# MACROSCOPIC QUANTUM PHENOMENA *in* HYBRID OPTOMECHANICAL SYSTEMS:

*A Theoretical Exploration*

*A Thesis submitted in Partial Fulfilment of the Requirements for the Degree of*
**DOCTOR *of* PHILOSOPHY**

*by*

**SAMPREET KALITA**

*Thesis Supervisor*
Prof. Amarendra Kumar Sarma


Department of Physics
Indian Institute of Technology Guwahati
Guwahati - 781039, Assam, India

January 2024

TH-3401_186121105

TH-3401_186121105

©2024 Sampreet Kalita






TH-3401_186121105

# Declaration

I, Sampreet Kalita, declare that the thesis entitled *"Macroscopic Quantum Phenomena in Hybrid Optomechanical Systems: A Theoretical Exploration"*, has been carried out by me at the Department of Physics, Indian Institute of Technology Guwahati, India, during the academic period starting from January 2019 and ending in December 2023 under the supervision of Prof. Amarendra Kumar Sarma. I have not submitted the contents of this thesis anywhere else for the award of a degree or diploma. For all the works that have been completed in collaboration with others, I have included only select parts in this thesis that have been worked out completely by me. Care has also been taken to reference the works and cite the resources which relate to the motivations, theories and experimental proposals presented in this thesis.

(Sampreet Kalita)
Department of Physics
Indian Institute of Technology Guwahati
Guwahati - 781039, Assam, India

Date:



TH-3401_186121105

# Certificate

This is to certify that the thesis entitled *"Macroscopic Quantum Phenomena in Hybrid Optomechanical Systems: A Theoretical Exploration"* submitted by **Sampreet Kalita** (186121105), a research scholar in the Department of Physics, Indian Institute of Technology Guwahati, is a record of original research work carried out under my supervision. The thesis has fulfilled all the requirements for the award of the degree of **Doctor of Philosophy** as per institute norms, and in my opinion, meet the standards for submission. The contents of this thesis have not been submitted to any other university or institute for the award of any degree or diploma.

Prof. Amarendra Kumar Sarma
Department of Physics
Indian Institute of Technology Guwahati
Guwahati - 781039, Assam, India

Date:

TH-3401_186121105

# Abstract

Optomechanical systems serve as a versatile platform for the study of classical and quantum phenomena both in the mesoscopic and macroscopic regime. They are also useful to analyze higher-order nonlinear effects or control the transmission, storage and retrieval of optical signals. Moreover, by integrating such systems into solid-state platforms and coupling other degrees of freedom to the optical and mechanical modes, one can study a multitude of phenomena arising in hybrid systems. In this thesis, we theoretically explore a handful of such macroscopic classical and quantum phenomena that emerge due to the radiation-pressure-induced optomechanical interaction in different configurations of hybrid open quantum systems. Specifically, we analyze (i) the behaviour of quantum synchronization in optically-coupled optomechanical systems, (ii) the transmission of a weak probe beam in an optomechanical analogue of annularly-trapped Bose-Einstein condensate placed inside a cavity, and (iii) the generation and the enhancement of robust entanglement and mechanical squeezing in modulated optomechanical setups. Our studies may find applications in optical sensing, quantum communication and quantum information processing with continuous variables.



TH-3401_186121105

# List of Publications

## Journal Publications as Thesis Chapters

1. **Sampreet Kalita**, Subhadeep Chakraborty and Amarendra K. Sarma, *Switching of Quantum Synchronization in Coupled Optomechanical Oscillators*, Journal of Physics Communications **5**, 115006 (2021, IOP Publishing)

2. **Sampreet Kalita**, Saumya Shah and Amarendra K. Sarma, *Significant Optoelectric Entanglement and Mechanical Squeezing in a Multimodulated Optoelectromechanical System*, Physical Review A **106**, 043501 (2022, American Physical Society)

3. **Sampreet Kalita**, Pardeep Kumar, Rina Kanamoto, M. Bhattacharya and Amarendra K. Sarma, *Pump-probe Cavity Optomechanics with a Rotating Atomic Superfluid in a Ring*, Physical Review A **107**, 013525 (2023, American Physical Society)

4. Priyankar Banerjee, **Sampreet Kalita** and Amarendra K. Sarma, *Robust Mechanical Squeezing beyond 3 dB in a Quadratically Coupled Optomechanical System*, Journal of the Optical Society of America B **40**, 1398 (2023, Optica Publishing Group)

## Other Journal Publications

1. Amarendra K. Sarma, Subhadeep Chakraborty and **Sampreet Kalita**, *Continuous Variable Quantum Entanglement in Optomechanical Systems: A Short Review*, AVS Quantum Science **3** , 015901 (2020, AIP Publishing)

2. Roson Nongthombam, **Sampreet Kalita** and Amarendra K. Sarma, *Synchronization of a Superconducting Qubit to an Optical Field Mediated by a Mechanical Resonator*, Physical Review A **107**, 013528 (2023, American Physical Society)



TH-3401_186121105

3. Amarendra K. Sarma and **Sampreet Kalita**, *Tutorial: Cavity Quantum Optomechanics*, Indian Journal of Pure & Applied Physics **61**, 622 (2023, Council of Scientific and Industrial Research - National Institute of Science Communication and Policy Research)

4. Pooja Kumari Gupta, **Sampreet Kalita** and Amarendra K. Sarma, *Quantum Interference induced Magnon Blockade and Antibunching in a Hybrid Quantum System*, Journal of the Optical Society of America B **41**, 447 (2024, Optica Publishing Group)

## Conference Proceedings

1. **Sampreet Kalita** and Amarendra K. Sarma, *The QOM Toolbox: An Object-oriented Python Framework for Cavity Optomechanical Systems*, Proceedings of Eighth International Congress on Information and Communication Technology **2**, 581 (2023, Springer Nature Singapore)



TH-3401_186121105

# Participations

## Conferences

1. Quantum 2.0 Conference (Optical Society of America), 14-17 September 2020 (virtual participation)

2. Student Conference on Optics & Photonics (PRL Ahmedabad), 24-26 November 2021 (virtual participation)

3. Conference on Optics Photonics and Quantum Optics (IIT Roorkee, India), 10-13 November 2022 (poster presentation)

4. $26^{th}$ Annual Conference on Quantum Information Processing (Ghent University, Belgium), 4-10 February 2023 (poster presentation)

5. $8^{th}$ International Congress on Information and Communication Technology (Brunel University London, UK), 20-23 February 2023 (oral presentation)

## Schools

1. Loop Quantum Gravity Online Summer School (CPT France), 7-25 June 2021 (virtual participation)

2. Qiskit Global Summer School on Quantum Machine Learning (IBM Quantum), 16-13 July 2021 (virtual participation)

3. New Trends in Quantum Simulation and Quantum Computation Summer School and Workshop (University of Nottingham, UK), 24-28 July 2023 (on-site participation)



TH-3401_186121105

## Workshops

1. Symposium on International Day of Light (IIT Guwahati, India), 16 May 2020 (on-site participation)
2. Hands on Invertible Neural Networks (ETS Montreal), 4 August 2021 (virtual participation)
3. Reservoir Computing Workshop (IIT Madras), 23-24 November 2022 (virtual participation)



TH-3401_186121105


*Dedicated to*
*the people I missed*
*during my doctoral tenure...*

TH-3401_186121105

# Acknowledgements

I begin by expressing my sincere gratitude towards my thesis supervisor Prof. Amarendra Kumar Sarma, for not only training me with the fundamentals, or guiding me through the hurdles, or motivating me to pursue pure Physics, but also for his constant emotional support and care throughout my journey. I also thank him for providing me with opportunities to interact with numerous people, which helped me enhance many soft skills along with my knowledge.

I thank my doctoral committee — Prof. Girish Sampath Setlur, Dr. Pankaj Kumar Mishra and Dr. Manabendra Sarma — for constantly inspiring me, and for their constructive feedback and insights on various intricacies. I also thank Prof. Mishkatul Bhattacharya and Dr. Pardeep Kumar for their time, their crucial inputs and their in-depth scrutiny of select works.

I acknowledge all the help, guidance and advice I obtained from the Heads of the department and all the faculty and staff members of the department during my doctoral period. I am also grateful to Prof. Anupam Saikia, Mr. Dhrubajyoti Sharma and Mr. Sanjib K. Saikia for their mentorship. I further thank Mr. Himanku Dutta and Mr. Riju Mahato for their prompt support.

I find myself lucky to have had effective interactions with several senior group members — Jyoti *da*, Subhadeep *bhaiya*, Abdelsalam *bhaiya*, Dipti *di* and Ambaresh *bhaiya* — whose enthusiastic responses and rejuvenating talks always pushed me towards good work. I thank my juniors Saumya and Priyankar for the dynamic brainstorming sessions. I am deeply thankful to my current group members — Roson, Pooja, Alolika, Urmimala and Gaurav — for their queries, criticism and energetic discussions, and all the *charcha* we had over *chai*! I also acknowledge from deep within, the invaluable parts played by Joy *da*, Rajnandan, Monu, Ravi, Shaona, Sumanth, Rohith, Hemanta *da*, Nayan *da*, Kamal, Pankaj *da*, Gyanendra *bhaiya*, Halim *da*, Gangesh *bhaiya* and Jennil, in the planning and designing of this thesis.

I thank my parents for their timeless support and care throughout my doctoral. I also thank my brother Mansmit and my cousin Arindam for their careful scrutiny of my works and that thoughtful suggestions which constitute a good part of my progress. Lastly, I am grateful to Pratyusha for not only reasoning out my ideas and reviving my presentations, but also introducing me to new domains of Physics!



TH-3401_186121105

# List of Figures





TH-3401_186121105

TH-3401_186121105

# Contents





TH-3401_186121105

Appendices





TH-3401_186121105

TH-3401_186121105

TH-3401_186121105

CHAPTER

1

# Introduction

It is the early 1600s. German philosopher Johannes Kepler is studying the trajectories of comets when he notices something unique in these moving objects — their dust tails always direct away from the sun [1]. A neoplatonic Kepler, who believes that light influences all inanimate matter [2], postulates that the rays of the sun "expell the effluvium" from the head of the comet. More than two centuries later, British mathematician William Thomson (Lord Kelvin) comes up with a theory on the "mechanical action of radiant heat", proposing that light can excite mechanical degrees of freedom [3]. In just a few years, Scottish physicist James Clerk Maxwell introduces his revolutionary theory on the electromagnetic nature of radiation, establishing that electromagnetic waves can carry momentum, and therefore, exert pressure [4]. And with that, what was once a hypothesis of metaphysical origin takes a credible mathematical form by the name of radiation pressure!

---

Select parts of this chapter are compiled from our article published in Indian J. Pure App. Phys. **61**, 822 (2023), titled *Tutorial: Cavity Quantum Optomechanics* and authored by Amarendra K. Sarma and Sampreet Kalita [5] (©2023 Indian Journal of Pure and Applied Physics under the Creative Commons Attribution 4.0 International license).



TH-3401_186121105

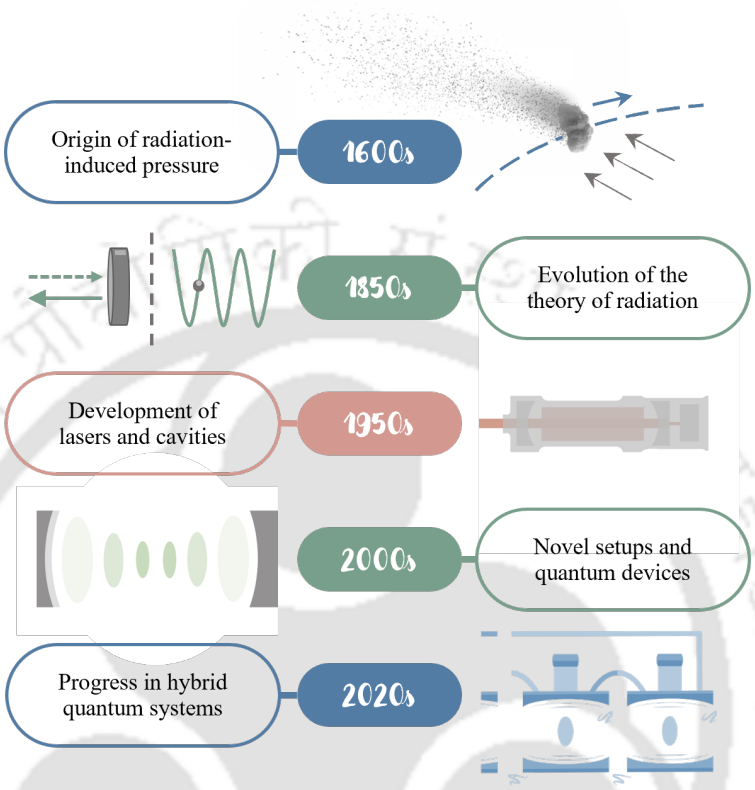


**Figure 1.1:** A brief history of optomechanics.

Another era of experimental breakthroughs begins with the discovery of the laser in the 1950s. Arthur Ashkin demonstrates its utility in trapping micro-particles inside an optical potential well [6]. Braginskii and Manukin study the ponderomotive effects of its radiation pressure, discussing optomechanical damping and bistability [7]. Caves demonstrates the quantum limits of sensitivity in interferometric optomechanical setups [8]. And by the beginning of the 21$^{st}$ century, a substantial number of theoretical proposals and experimental demonstrations of optomechanical effects surface in the scientific community [9, 10]. With further advancements in nano-fabrication and refrigeration techniques, optomechanical systems span a very wide spectrum of devices, ranging from nanometer-scale structures to macroscopic architectures maintained at cryogenic temperatures (refer to Figure 1.2).

TH-3401_186121105

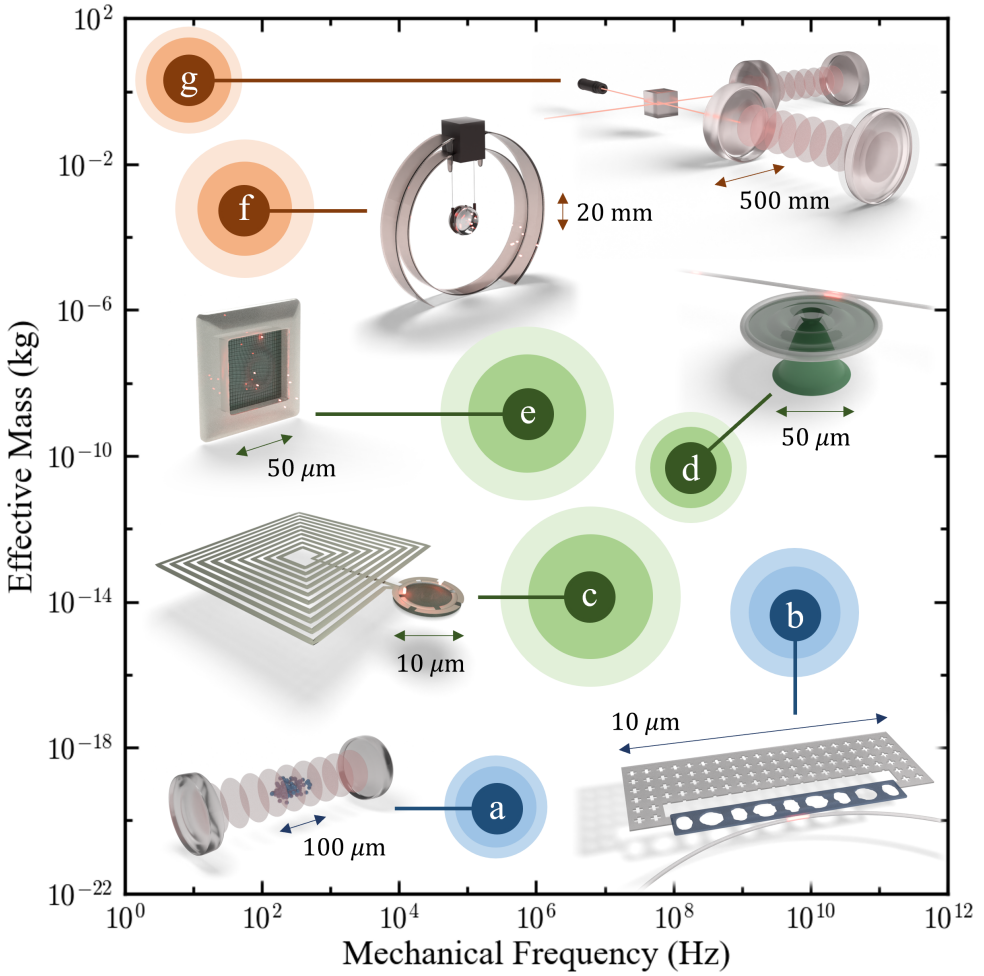


**Figure 1.2:** Operational regimes of different optomechanical devices [11, 12]: (a) Ultracold atoms, (b) optomechanical crystals, (c) electro-optomechanical systems, (d) mechanical resonators coupled to waveguides, (e) suspended mechanical membranes, (f) suspended mirrors and (g) interferometric setups. Due to this diversity, such devices can exhibit a multitude of phenomena, such as bistability [13], chaos [14], synchronization [15], cooling [16], induced transparency [17], anti-bunching [18], entanglement [19], squeezing [20], solitons [21], and so on.

---

For an extensive list of works on various classical and quantum phenomena in diverse open quantum systems, the reader may refer to our "quantum optomechanics resources" website. Theoretical proposals for various phenomena in optomechanics are available at this webpage. Experimental works with various setups are also available at this webpage.

TH-3401_186121105

Optomechanical models have been utilized to study various phenomena in diverse physical systems. Most of them diverge into seemingly different directions, but their underlying formalisms fall under the same umbrella of cavity optomechanics. Here, we explore a few such directions in detail. The first one is the ubiquitous phenomenon of *synchronization*, where two or more systems sympathetically adjust their rhythms to oscillate in unison. Initially observed in the oscillations of maritime clocks [22], classical synchronization has been reported across several domains of nature, from micro-biological beings to celestial objects [23]. This phenomena has also been studied for time-keeping applications in classical networks [24, 25] and has gathered recent interest as the quantum resource [26, 27], both as a measure of quantum correlations [28] and as an attribute in quantum communication protocols [29].

The next phenomenon we shall explore is a consequence of destructive interference between excitation pathways in $\Lambda$-type energy configurations and is known as *induced transparency*. Analogous to electromagnetically induced transparency, which is observed in $\Lambda$-type atomic systems [30], optomechanically induced transparency results in a window of transmission in the output spectrum of a weak probe beam when it perturbs a strongly driven optomechanical system [17, 31]. This provides a two-way benefit. On one hand, the output probe spectrum can be used to gather information about the system by minimally disturbing it, making this method useful for sensing applications [32]. On the other hand, the properties of the system can be used to manipulate the dispersion profile of the output probe beam, resulting in a controllable variation in its propagation speed [33].

Finally, we shall analyze in detail the phenomenon of *entanglement* in a close connection with *mechanical squeezing*. A characteristic feature of quantum mechanics, entanglement describes a form of spatial correlation that is shared between two components even when they are separated by large distances. It not only throws light on the fundamental nature of physical reality [34–37], but also serves as an important resource for quantum information processing [38, 39]. Numerous schemes have been proposed to enhance the entanglement between optical and mechanical degrees of freedom, notable among which are the introduction of modulations [40] and the application of feedback [41]. Although both optomechanical entanglement and mechanical squeezing have established their significance in metrology [42, 43], entangling microwave and optical signals in hybrid open quantum systems can open up new prospects to build electro-optomechanical converters [44, 45]. Such architectures may find applications in the development of quantum radars [46].

TH-3401_186121105

In this chapter, we present the theories and methodologies required to study the above-mentioned phenomena in optomechanical systems. We first introduce the underlying principles of a single optomechanical cavity, covering in detail the interesting physics and the mathematics of its formalism with suitable examples. The theoretical models discussed in the rest of the chapters utilize these physical descriptions and mathematical structures. Next, we provide an overview of different classical and quantum phenomena. Finally, we describe the numerical workflow and outline the structure of this thesis. Throughout the chapter, we highlight most useful terms, mention background facts, add relevant notes, point out approximations, specify parameter regimes and connect related theories through short digressions.

## 1.1 Cavity Optomechanical Systems

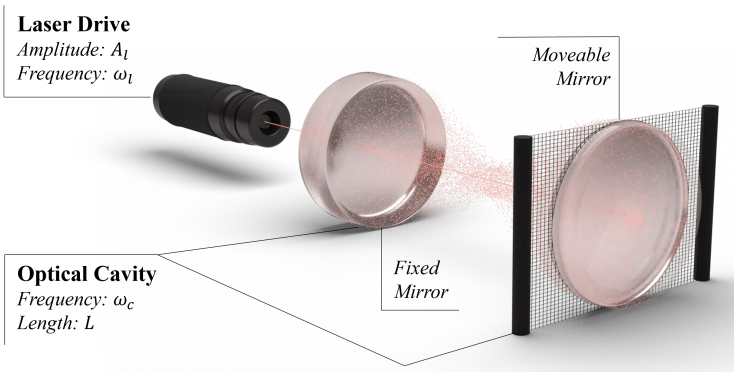


**Figure 1.3:** Illustration of a driven optomechanical cavity.

Optomechanical effects can be realized in a wide variety of platforms, ranging from nanomechanical cantilevers to kilogram-scale interferometric setups. Although, a surprisingly simple model can be used to describe most of the phenomena displayed by these seemingly different platforms. We depict this simplistic form in Figure 1.3, where we illustrate a driven cavity with two highly reflective mirrors — one fixed and the other moveable, separated by some distance $L$ — driven by a laser of amplitude $A_l$ and frequency $\omega_l$ [9].

TH-3401_186121105

At the heart of all cavity optomechanical systems is the radiation pressure interaction of optical photons with a mechanical element. The cavity plays an important role in boosting this optical force by circulating the light field for longer durations. The radiation pressure force exerted by this intracavity field then results in a continuous transfer of momentum to the mechanical element. The resultant displacement of the mechanical element caused by this intensity-dependent force changes the length of the cavity, thereby changing the cavity's resonant frequency. One can estimate the dependence of the cavity frequency $\omega_c$ on the mechanical displacement $\hat{q}$ by focusing on a single mode (say with a mode number $n$) at an optical frequency of $\omega_o$ which is close to the laser frequency. For a general cavity, we have

RECALL

*A Fabry-Pérot cavity with two fixed mirrors can accommodate modes that have frequencies in the integral multiples of $\pi c/L$, where $c$ is the speed of light.*

$$\omega_c(\hat{q}) \approx \omega_o + \frac{\partial \omega_c(\hat{q})}{\partial \hat{q}}\hat{q} + \frac{\partial^2 \omega_c(\hat{q})}{2\partial \hat{q}^2}\hat{q}^2 + \dots . \tag{1.1}$$

Equation (1.1) is core to all optomechanical systems and one can immediately work out three very important outcomes from this relation. First, the intensity-dependent mechanical displacement induces multistability in the intracavity optical field as it modifies the cavity frequency. Second, the cavity now behaves like a nonlinear optical medium because of the uneven phase shifts introduced in the output field of the cavity due to this displacement. Third, by detuning the laser frequency around the resonant frequency of the cavity, one can change the intracavity intensity, which in turn changes the mechanical displacement, thereby influencing the radiation pressure force acting on the mechanical element. This introduces a change in the mechanical spring constant and the mechanical damping. All these outcomes play a crucial role in the design, working and output of optomechanical systems. Before diving into their details, let us first systematically formulate the Hamiltonian.

The Hamiltonian of a driven optomechanical system $\hat{H}_s$ consists of the contributions from the optical photons, the mechanical element, the interaction between the optics and mechanics, and the laser drive Hamiltonian $\hat{H}_d$. The optical field is considered to be a harmonic oscillator with annihilation operator $\hat{a}$. The mechanical excitations can also be treated as a harmonic oscillator with mass $m$, frequency $\omega_m$ and mode annihilation operator $\hat{b}$. Both these optical and mechanical modes obey the Bosonic commutation relations

TH-3401_186121105

$[\hat{\mathcal{O}}, \hat{\mathcal{O}}^\dagger] = 1$ ($\hat{\mathcal{O}} \in \{\hat{a}, \hat{b}\}$) with number operators given by $\hat{n}_\mathcal{O} = \hat{\mathcal{O}}^\dagger\hat{\mathcal{O}}$.

NOTE

*The momentum imparted by the photons to the mechanical element gives rise to mechanical degrees of freedom, whose individual movements are given by the response of the elastic strain in their harmonic modes [12]. However, the macroscopic displacement of the mirror largely depends on the shorter-wavelength microscopic phononic modes and their collective excitations can be described by a harmonic oscillator with effective mass and fixed frequency. We conventionally refer to the single-mode treatment of effective excitations and the resultant pheonmena arising from such analysis as "macroscopic" [9].*

One can then express the full Hamiltonian of the driven cavity in terms of the energy and number $(\hat{n}_a, \hat{n}_b)$ of each quanta using Equation (1.1) as

$$\hat{H}_s = \hbar\omega_c(\hat{q})\hat{n}_a + \hbar\omega_m\hat{n}_b + \hat{H}_d = \hbar\omega_o\hat{a}^\dagger\hat{a} + \hbar\omega_m\hat{b}^\dagger\hat{b} + \hat{H}_i + \hat{H}_d, \tag{1.2}$$

where $\hat{H}_i$ denotes the energy of interaction between the optical and mechanical modes, and $\hat{H}_d$ is the Hamiltonian of the laser drive. For a simplified 1D scenario of the mechanical displacement ($\omega_c(\hat{q}) = n\pi c/(L+\hat{q}) \approx \omega_o - \omega_o\hat{q}/L$), we can approximate the Hamiltonian for the optomechanical interaction as

$$\hat{H}_i \approx -\hbar f\hat{q}\hat{a}^\dagger\hat{a} = -\hbar g_0\hat{a}^\dagger\hat{a}\left(\hat{b}^\dagger + \hat{b}\right). \tag{1.3}$$

Here we introduce two new parameters. The first is the frequency pull parameter [9] $f = -\partial\omega_c(\hat{q})/\partial\hat{q} = \omega_o/L$, which quantifies linear dispersive shifts in the resonance frequency of the optical field induced by the displacement, and is related to the radiation pressure force as $\hat{F}_{rad} = -\partial\hat{H}_i/\partial\hat{q} = \hbar f\hat{a}^\dagger\hat{a}$. The second parameter is a more fundamental one called the optomechanical coupling constant [9] $g_0 = f\sqrt{\hbar/(2m\omega_m)}$. This relates the radiation pressure force of a single photon on a single phonon and estimates the strength of their interaction.

RECALL

*The zero-point fluctuations in the position of a harmonic oscillator of mass $m$ and frequency $\omega_m$ is given by $\sqrt{\hbar/(2m\omega_m)}$.*

Finally, we write the contribution of the laser drive based on the quantized electromagnetic field description as $\hat{H}_d = i\hbar A_l\left(\hat{a}^\dagger e^{-i\omega_l t} - \hat{a}e^{i\omega_l t}\right)$ and obtain

$$\hat{H}_s = \hbar\omega_o\hat{a}^\dagger\hat{a} + \hbar\omega_m\hat{b}^\dagger\hat{b} - \hbar g_0\hat{a}^\dagger\hat{a}\left(\hat{b}^\dagger + \hat{b}\right) + i\hbar A_l\left(\hat{a}^\dagger e^{-i\omega_l t} - \hat{a}e^{i\omega_l t}\right). \tag{1.4}$$

TH-3401_186121105

The time-dependent terms can also be removed by switching to the frame of the laser frequency via a unitary transformation. Taking the laser detuning as $\Delta_0 = \omega_l - \omega_o$, the Hamiltonian in the rotating frame of the laser reads as

$$\hat{H}_l = -\hbar\Delta_0 \hat{a}^\dagger \hat{a} + \hbar\omega_m \hat{b}^\dagger \hat{b} - \hbar g_0 \hat{a}^\dagger \hat{a} \left(\hat{b}^\dagger + \hat{b}\right) + i\hbar A_l \left(\hat{a}^\dagger - \hat{a}\right). \tag{1.5}$$

DIGRESSION 1.1

**Rotating Frame Transformation**

Let us take a quick look at the Schrödinger equation $i\hbar\, d|\Psi\rangle/dt = \hat{H}_s|\Psi\rangle$, where we have defined $|\Psi\rangle$ as the wavefunction in the Schrödinger picture. If we choose a unitary operator $\hat{U} = e^{i\omega_l \hat{a}^\dagger \hat{a} t}$ such that $|\Psi_l\rangle = \hat{U}|\Psi\rangle$ is the new wavefunction in the rotating frame of the laser frequency, it can be shown by a simple substitution into the Schrödinger equation that

$$i\hbar \frac{d|\Psi_l\rangle}{dt} = \left(\hat{U}\hat{H}_s\hat{U}^\dagger - \hbar\omega_l \hat{a}^\dagger \hat{a}\right)|\Psi_l\rangle = \hat{H}_l|\Psi_l\rangle,$$

where $H_l$ is the Hamiltonian in the laser frame. Using the fact that $\hat{U}\hat{U}^\dagger = \mathbb{1}$, one can derive this Hamiltonian with the Baker-Campbell-Hausdroff relation,

$$e^{\hat{A}}\hat{B}e^{-\hat{A}} = \hat{B} + \left[\hat{A}, \hat{B}\right] + \cdots + \frac{1}{n!}\left[\hat{A}, \left[\hat{A}, \ldots \left[\hat{A}, \left[\hat{A}, \hat{B}\right]\right]\ldots\right]\right] + \ldots.$$

By switching to the laser frame, one can now analyze the slower dynamics of the mechanical motion. The laser frequency can also be adjusted in such a way that the detuning $\Delta_0$ is comparable to $\omega_m$ to facilitate the exchange of energy between the photons and the phonons. We discuss the scenarios pertaining to the different types of detuning later in this chapter. Also, for the sake of simplicity in subsequent expressions, we shall drop the circumflex (hat notation) in the operators henceforth.

PARAMETER

*Typically, the resonant optical frequency of the cavity is on the order of $10^{15}$ Hz, whereas the mechanical frequency usually lies in between KHz and GHz. The optomechanical coupling constant can range from a few hundred Hz (weak regime) to a few GHz (strong regime).*

In addition to the contributions mentioned above, open quantum systems such as optomechanical systems also dissipate quanta into the environment.

TH-3401_186121105

The photons experience absorption and scattering losses since they are coupled to the external environment through the mirrors. These losses collectively define the optical energy decay rate $\kappa$. This rate also determines the quality factor of the cavity $Q_o = \omega_o/\kappa$, which signifies the total number of times a single photon oscillates inside the cavity before decaying out. Similarly, the mechanical motion is affected by environmental factors such as viscous drag, clamping losses, phonon-phonon interactions and losses due to its composition. The mechanical energy decay rate $\gamma$ takes these effects into account. It also characterizes the strength of coupling between the mechanical mode and the environment. The mechanical quality factor $Q_m = \omega_m/\gamma$ is another equivalent parameter which is related to the phonon lifetime.

APPROXIMATION

*The thermal environment surrounding an open quantum system can be modelled as a collection of non-interacting harmonic oscillators. The noise entering the system can then be safely approximated as Markovian, with zero mean and $\delta$-correlated second moments [12].*

In addition, the environment introduces thermal fluctuations into the system. Thermal phonons play a very important role on the quantum dynamics of the mechanical mode. However, as the optical frequencies are very high, the effect of the thermal photons entering the cavity can be safely neglected and the cavity can be considered as being coupled to a reservoir at zero temperature. The main source of noise in the optical mode is the input from the laser drive. The laser power $P_l$ entering the cavity is related to its amplitude as $A_l = \sqrt{\kappa P_l/\hbar\omega_l}$ and the input power associated with its white noise $a_{in}$ is given by $P_{in} = \hbar\omega_l\langle a_{in}^\dagger a_{in}\rangle$ [47]. The white noise entering through the laser and the Langevin noise $b_{in}$ perturbing the mechanical oscillations obey [12, 47–49]

$$\langle a_{in}(t)a_{in}^\dagger(t')\rangle = \delta(t-t'), \tag{1.6a}$$

$$\langle b_{in}^\dagger(t)b_{in}(t')\rangle = n_{th}\delta(t-t'), \tag{1.6b}$$

$$\langle b_{in}(t)b_{in}^\dagger(t')\rangle = (n_{th}+1)\,\delta(t-t'), \tag{1.6c}$$

where $n_{th} = [e^{\{\hbar\omega_m/(k_BT)\}} - 1]^{-1}$ is the mean thermal occupancy at bath frequency $\omega_m$ and bath temperature $T$, $k_B$ being the Boltzmann constant. Using the mean-field approximation, it can be derived that the optical mode is modulated by an extra amount of $\sqrt{\kappa}a_{in}$ and the output field exiting the cavity is given by the input-output theory as $a_{out} = a_{in} - \sqrt{\kappa}a$ [47].

TH-3401_186121105

DIGRESSION 1.2

**Heisenberg Equations of Motion**

In the Heisenberg picture, the operators $\mathcal{O}_H$ evolve in time whereas the wavefunctions $|\Psi_H\rangle$ are constants of time. Using the unitary time-evolution operator $U = e^{-iH_l t/\hbar}$, a transformation from the Schrödinger picture to the Heisenberg picture can be carried out such that $\mathcal{O}_H = U^\dagger \mathcal{O} U$ and $|\Psi\rangle = U|\Psi_H\rangle$ is the wavefunction in the Schrödinger picture. Using these relations and the Schrödinger equation $i\hbar\, d|\Psi\rangle/dt = H_l|\Psi\rangle$, it can be shown that

$$\frac{d\mathcal{O}_H}{dt} = \frac{1}{i\hbar}\left(\mathcal{O}_H H_l - H_l \mathcal{O}_H\right) = \frac{1}{i\hbar}\left[\mathcal{O}_H, H_l\right].$$

Using Equation (1.5), we can derive the Heisenberg Langevin equations corresponding to the optical and mechanical modes, which read as

$$\begin{aligned}
\dot{a} &= \frac{1}{i\hbar}[a, H_l] - \frac{\kappa}{2}a + \sqrt{\kappa}a_{in} && \text{(1.7a)}\\
&= -\left(\frac{\kappa}{2} - i\Delta_0\right)a + ig_0\left(b^\dagger + b\right)a + A_l + \sqrt{\kappa}a_{in}, && \text{(1.7b)}\\
\dot{b} &= \frac{1}{i\hbar}[b, H_l] - \frac{\gamma}{2}b + \sqrt{\gamma}b_{in} && \text{(1.7c)}\\
&= -\left(\frac{\gamma}{2}b + i\omega_m\right)b + ig_0 a^\dagger a + \sqrt{\gamma}b_{in}. && \text{(1.7d)}
\end{aligned}$$

It can be clearly seen here that the frequency shift introduced in the optical mode by the mechanical position changes the optical mode amplitude, which in turn changes the mechanical mode amplitude. Both of these phenomena depend directly on the optomechanical coupling constant, and therfore, on the frequency pull. To have a better grasp on how these parameters affect the system dynamics, let us quickly analyze the classical scenario.

Assuming that the input fluctuations are zero-mean Gaussian in nature, we obtain the equations of motion of classical mean amplitudes $\alpha = \langle a\rangle$ and $\beta = \langle b\rangle$ by taking an ensemble average of Equations (1.7), which gives

$$\begin{aligned}
\dot{\alpha} &= -\left(\frac{\kappa}{2} - i\Delta\right)\alpha + A_l, && \text{(1.8a)}\\
\dot{\beta} &= -\left(\frac{\gamma}{2} + i\omega_m\right)\beta + ig_0\alpha^*\alpha, && \text{(1.8b)}
\end{aligned}$$

where we have introduced the effective detuning as $\Delta = \Delta_0 + g_0(\beta^* + \beta)$.

TH-3401_186121105

APPROX.

*In deriving Equations (1.8), we utilized the mean-field relation, $\langle \mathcal{O}_i \mathcal{O}_j \rangle \simeq \langle \mathcal{O}_i \rangle \langle \mathcal{O}_j \rangle$, giving us a decoupled effective detuning.*

Depending on the parameters of the systems, in the long-time limit, the dynamics of these complex-valued classical amplitudes may settle down either into a stationary steady-state, undergo self-sustained oscillations, or even display chaotic behaviour. For the first case, we can obtain the exact steady-state amplitudes by equating the right-hand sides of Equations (1.8) to zero. This gives us $\alpha_s = A_l/(\kappa/2 - i\Delta_s)$ and $\beta_s = ig_0|\alpha_s|^2/(\gamma/2 + i\omega_m)$. It can be seen here that the mechanical mode gets displaced by an amount proportional to the optical field intensity $|\alpha_s|^2$, and this displacement gives rise to a phase shift in the optical mode through the effective steady-state detuning $\Delta_s$. Substituting the expression of $\beta_s$ in the effective detuning, we obtain a cubic in the mean optical occupancy $N_o = |\alpha_s|^2$, which reads as

$$4C^2N_o^3 + 8C\Delta_0 N_o^2 + \left(4\Delta_0^2 + \kappa^2\right) N_o - 4\,|A_l|^2 = 0. \tag{1.9}$$

where $C = 2g_0^2\omega_m/(\gamma^2/4 + \omega_m^2)$.

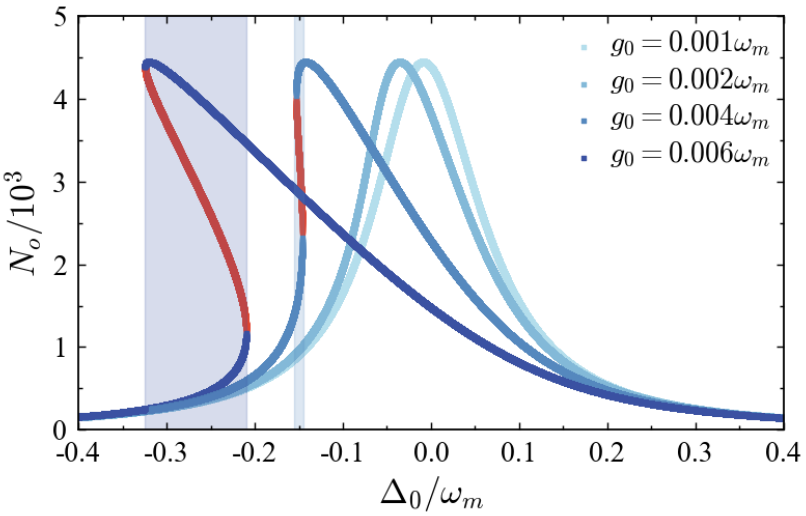


**Figure 1.4:** Number of intracavity optical photons ($N_o$) with variation in the laser detuning ($\Delta_0$) for different values of the coupling constant ($g_0$) obtained using Equation (1.9). The shaded areas in blue denote the regions of bistability. The parameters used (in units of $\omega_m$) are $A_l = 5.0$, $\gamma = 0.005$ and $\kappa = 0.15$.

TH-3401_186121105

The solutions to Equation (1.9) give us the two regimes of steady-state values. One of them contains one real root while the other one contains three real roots. The latter case is the multistable steady-state regime with three branches (shaded areas in Figure 1.4). However, when the detuning of the laser is gradually changed, the photons do not trace the central branch and the system makes discontinuous jumps between the upper and lower branches displaying a hysteretic behaviour [13], thereby displaying bistability [9, 12].

NOTE

*In most situations, it is preferable to retain the system away from bistability. One can also derive analytical conditions for the dynamical stability of the steady-state amplitudes obtained using the mean optical occupancies by utilizing the Routh-Hurwitz criteria for nonlinear dynamical systems [50].*

DIGRESSION 1.3

**Routh-Hurwitz Stability Criteria**

The determinant of any eigenvalue equation $\mathbf{A}-\lambda\mathbb{1}=0$ for a Jacobian matrix $\mathbf{A}$ of dimension $d$ can be expressed as a polynomial in the eigenvalues $\lambda$ as $\sum_{k=0}^{d} e_k\lambda^{d-k}=0$, where $e_k$ are the corresponding coefficients. One can then construct a square matrix $\mathbf{M}$ such that its elements (0-indexed) are given by

$$\mathbf{M}_{ij}=\begin{cases} e_{2i-j+2}, & \text{if } 0\leq 2i-j+2\leq d,\\ 0, & \text{otherwise.}\end{cases}$$

The Routh-Hurwitz criteria [50] simply states that the number of positive real eigenvalues of $\mathbf{A}$ is equal to the number of times the sequence $T_{k+1}/T_k$ is negative. Here, $T_k=\det[\mathbf{M}_k]$ are the determinants of the square submatrices $\mathbf{M}_k$, comprising of the first $k$ rows and columns of $\mathbf{M}$, with $T_0=a_0$.

When the cavity is strongly driven, the radiation pressure force enhances considerably due to the large number of intracavity photons. Even for small strengths of optomechanical coupling, the effective coupling between the optics and the mechanics enhances significantly. At this point, the system can be approximated by its linearized description. This means that the mode operators can be expressed as a sum of their large classical mean amplitudes and the quantum fluctuations around these values, i.e., $a=\alpha+\delta a$ and $b=\beta+\delta b$.

TH-3401_186121105

The dynamics of these fluctuations can be derived from Equations (1.7) as,

$$\delta\dot{a} = -\left(\frac{\kappa}{2} - i\Delta\right)\delta a + ig\left(\delta b^\dagger + \delta b\right) + \sqrt{\kappa}a_{in}, \tag{1.10a}$$

$$\delta\dot{b} = -\left(\frac{\gamma}{2} + i\omega_m\right)\delta b + i\left(g\delta a^\dagger + g^*\delta a\right) + \sqrt{\gamma}b_{in}, \tag{1.10b}$$

where $g = g_0\alpha$ is the effective coupling constant [12]. Thus, we see that the optomechanical coupling strength is enhanced by the optical mode amplitude.

APPROXIMATION

*In the presence of a strong laser drive, the classical mean amplitudes assume much larger values than the quantum fluctuations. Assuming that the optomechanical coupling is comparatively weaker than its effective value, we can ignore the second-order terms in $\delta a$ and $\delta b$ as a part of this linearization.*

At this point, it is interesting to consider a simple scenario where the classical values settle down to a steady state and the phase of the laser light is adjusted in such a way that $\alpha_s$ assumes only real values, with $g_s = g_0|\alpha_s| = g_0\alpha_s$. One can then obtain a set of linear equations where the dynamics of the optical and mechanical fluctuations is governed by a position-position interaction. An equivalent simplified linearized Hamiltonian that describes this scenario is given by [12]

$$H_l = -\hbar\Delta_s\delta a^\dagger\delta a + \hbar\omega_m\delta b^\dagger\delta b - \hbar g_s\left(\delta a^\dagger + \delta a\right)\left(\delta b^\dagger + \delta b\right). \tag{1.11}$$

DIGRESSION 1.4

**Optomechanical Cooling and Parametric Amplification**

When the cavity is driven by a laser source, the light scattered by the mechanical excitations gives rise to Stokes and anti-Stokes sidebands, where a quanta of mechanical energy is either absorbed or excited by the light field respectively. Depending on the detuning of the laser, this results in either cooling or heating of the mechanical element. In the red-detuned regime, when $\Delta_s = -\omega_m$, the interaction Hamiltonian takes the form of a beam-splitter interaction under the rotating wave approximation [12], given by the energy-conserving interaction Hamiltonian

$$\tilde{H}_i = -\hbar g_s\left(\delta a^\dagger\delta b + \delta a\delta b^\dagger\right).$$

TH-3401_186121105

Since the mechanical mode is at a higher temperature than the optical mode, such a Hamiltonian preserves the phonon de-excitation process and this leads to a cooling effect in the mechanical motion. Cooling of the mechanical mode is a requirement for most quantum optomechanical applications and various schemes have been proposed to cool the mechanical oscillator to its quantum ground state. Similarly, in the blue-detuned regime, when $\Delta_s = \omega_m$, the Hamiltonian takes a form known as the squeezed interaction, such that

$$\tilde{H}_i = -\hbar g_s \left(\delta a^\dagger \delta b^\dagger + \delta a \delta b\right).$$

Under suitable conditions, the resonant interaction of the modes supresses the photon de-excitation process and this leads to heating or amplification of the mechanical mode through simultaneous excitations of optical and mechanical quanta. This form can also be used to squeeze the variance of the position fluctuations of the mechanical mode at the expense of increased variance in the momentum fluctuations [20,40]. Such parametric processes are routinely used in interferometric setups to enhance the mechanical sensitivity.

In order to estimate the degree of various quantum phenomena, it is, in general, useful to extract the correlations between the components of the system. To achieve this, we first express the Equations (1.10) in terms of the fluctuation quadratures, defined as $X = (\delta a^\dagger + \delta a)/\sqrt{2}$, $Y = i(\delta a^\dagger - \delta a)/\sqrt{2}$, $Q = (\delta b^\dagger + \delta b)/\sqrt{2}$ and $P = i(\delta b^\dagger - \delta b)/\sqrt{2}$, which results in

$$\delta\dot{X} = -\frac{\kappa}{2}X - \Delta Y - 2g_I Q + \sqrt{\kappa}X_{in}, \tag{1.12a}$$

$$\delta\dot{Y} = \Delta X - \frac{\kappa}{2}Y + 2g_R Q + \sqrt{\kappa}Y_{in}, \tag{1.12b}$$

$$\delta\dot{Q} = -\frac{\gamma}{2}Q + \omega_m P + \sqrt{\gamma}Q_{in}, \tag{1.12c}$$

$$\delta\dot{P} = 2g_R X + 2g_I Y - \omega_m Q - \frac{\gamma}{2}P + \sqrt{\gamma}P_{in}, \tag{1.12d}$$

where $g_R$ and $g_I$ are the real and imaginary components of $g$ respectively, while $X_{in} = (a_{in}^\dagger + a_{in})/\sqrt{2}$, $Y_{in} = i(a_{in}^\dagger - a_{in})/\sqrt{2}$, $Q_{in} = (b_{in}^\dagger + b_{in})/\sqrt{2}$ and $P_{in} = i(b_{in}^\dagger - b_{in})/\sqrt{2}$ are the noise quadratures governed by Equations (1.6). Using $\mathbf{u} = (X, Y, Q, P)^T$ as the vector of quadratures, we can rewrite Equations (1.12) compactly as the fluctuation quadrature rate equation

$$\dot{\mathbf{u}}(t) = \mathbf{A}(t)\mathbf{u}(t) + \mathbf{n}(t) \tag{1.13}$$

TH-3401_186121105

where $\mathbf{n} = (\sqrt{\kappa}X_{in}, \sqrt{\kappa}Y_{in}, \sqrt{\gamma}Q_{in}, \sqrt{\gamma}P_{in})$ and the drift matrix $\mathbf{A}$ equals

$$\begin{pmatrix} -\frac{\kappa}{2} & -\Delta & -2g_I & 0 \\ \Delta & -\frac{\kappa}{2} & 2g_R & 0 \\ 0 & 0 & -\frac{\gamma}{2} & \omega_m \\ 2g_R & 2g_I & -\omega_m & -\frac{\gamma}{2} \end{pmatrix}. \tag{1.14}$$

Finally, we define the correlation matrix of the quadratures as [19]

$$\mathbf{V}_{ij} = \frac{1}{2}\langle \mathbf{u}_i\mathbf{u}_j + \mathbf{u}_j\mathbf{u}_i \rangle \tag{1.15}$$

It can be shown that the dynamical form of this matrix satisfies the equation

$$\dot{\mathbf{V}}(t) = \mathbf{A}\mathbf{V}(t) + \mathbf{V}(t)\mathbf{A}^T + \mathbf{D}, \tag{1.16}$$

where $\mathbf{D} = \text{Diag}[\kappa/2, \kappa/2, \gamma(n_{th} + 1/2), \gamma(n_{th} + 1/2)]$ is the noise matrix. This correlation matrix also preserves the compact uncertainty relation

$$\mathbf{V} + \frac{i}{2}\mathbf{\Omega} \geq 0, \tag{1.17}$$

where $\mathbf{\Omega} = \bigoplus_{k=1}^{N} \begin{pmatrix} 0 & 1 \\ -1 & 0 \end{pmatrix}$; $N$ being the number of modes in the system. To estimate bipartite phenomena in optomechanical systems, this matrix is usually written in terms of correlation submatrices in the $4 \times 4$ block form

$$\mathcal{V} = \begin{pmatrix} \mathcal{A} & \mathcal{C} \\ \mathcal{C}^T & \mathcal{B} \end{pmatrix}, \tag{1.18}$$

where $\mathcal{A}$ and $\mathcal{B}$ represent the individual submatrices of the two participating components and $\mathcal{C}$ represents the submatrix of their cross-correlations.

**NOTE**

*The stability of the formal solution is a necessary condition for the derivation of this dynamical form. In order to satisfy this dynamical stability condition, the eigenvalues of the drift matrix cannot assume positive real values.*

TH-3401_186121105

DIGRESSION 1.5

**Dynamical Form of the Correlation Matrix**

The compact rate equation for the quadrature vectors is analogous to

$$\dot{\mathbf{u}}_i(t) = \sum_k \mathbf{A}_{ik}(t)\mathbf{u}_k(t) + \mathbf{n}_i(t),$$

whose formal solution can be obtained using the Langevin approach as

$$\mathbf{u}_i(t) = \sum_k \mathbf{M}_{ik}(t,t_0)\mathbf{u}_k(t_0) + \sum_k \int_{t_0}^{t} ds \mathbf{M}_{ik}(t,s)\mathbf{n}_k(s),$$

where $\dot{\mathbf{M}}(t,t_0) = \mathbf{A}(t)\mathbf{M}(t,t_0)$ with $\mathbf{M}(t,t) = \mathbb{1}$. Due to the presence of the stochastic noises inside the integral, we cannot write an exact analytical solution for the dynamics of the quantum fluctuations. However, by utilizing the properties of Gaussian noises, we can focus on the second-order moments of the fluctuation quadratures through the correlation matrix. Differentiating Equation (1.15), one obtains the dynamics of each correlation element as

$$\begin{aligned}\dot{\mathbf{V}}_{ij}(t) &= \sum_k \mathbf{A}_{ik}(t)\mathbf{V}_{kj}(t) + \sum_l \mathbf{A}_{jl}(t)\mathbf{V}_{il}(t) \\ &\quad + \frac{1}{2}\langle \mathbf{n}_i(t)\mathbf{u}_j(t) + \mathbf{u}_j(t)\mathbf{n}_i(t)\rangle \\ &\quad + \frac{1}{2}\langle \mathbf{u}_i(t)\mathbf{n}_j(t) + \mathbf{n}_j(t)\mathbf{u}_i(t)\rangle\end{aligned}$$

The final term in this expression can be further simplified by substituting the formal solution and using the fact that the noises have zero mean, giving us

$$\begin{aligned}&\sum_k \frac{1}{2}\int_{t_0}^{t} ds \mathbf{M}_{ik}(t,s)\langle \mathbf{n}_k(s)\mathbf{n}_j(t) + \mathbf{n}_j(t)\mathbf{n}_k(s)\rangle \\ &= \sum_k \int_{t_0}^{t} ds \mathbf{M}_{ik}(t,s)\mathbf{D}_{kj}\delta(s-t) \\ &= \frac{1}{2}\sum_k \mathbf{M}_{ik}(t,t)\mathbf{D}_{kj} = \frac{1}{2}\mathbf{D}_{ij}\end{aligned}$$

where we have defined the noise matrix $\mathbf{D}$ in such a way that $\langle \mathbf{n}_i(t)\mathbf{n}_j(t') + \mathbf{n}_j(t')\mathbf{n}_i(t)\rangle/2 = \mathbf{D}_{ij}\delta(t-t')$. Similarly, it can be shown that $\langle \mathbf{n}_i(t)\mathbf{u}_j(t) + \mathbf{u}_j(t)\mathbf{n}_i(t)\rangle/2 = \mathbf{D}_{ij}/2$. Thus, we can simplify the correlation dynamics to

$$\dot{\mathbf{V}}_{ij}(t) = [\mathbf{A}(t)\mathbf{V}(t)]_{ij} + \left[\mathbf{V}(t)\mathbf{A}^T(t)\right]_{ij} + \mathbf{D}_{ij}.$$

TH-3401_186121105

## 1.2 Classical and Quantum Phenomena

The inherently nonlinear interactions between the optical and the mechanical elements of cavity optomechanical systems give rise to a rich variety of observable effects, both in the classical and the quantum domain. Through this section, we attempt to introduce the physical origins of those phenomena which are relevant to this thesis, namely, synchronization, induced transparency, entanglement and squeezing. We also present a brief mathematical background of some established quantifiers pertaining to these phenomena. These figure of merits are utilized in later chapters where we discuss their applications in detail. Here we demonstrate how these phenomena can be observed in optomechanical systems with small changes in their parameters.

### 1.2.1 Nonlinear Dynamics and Synchronization

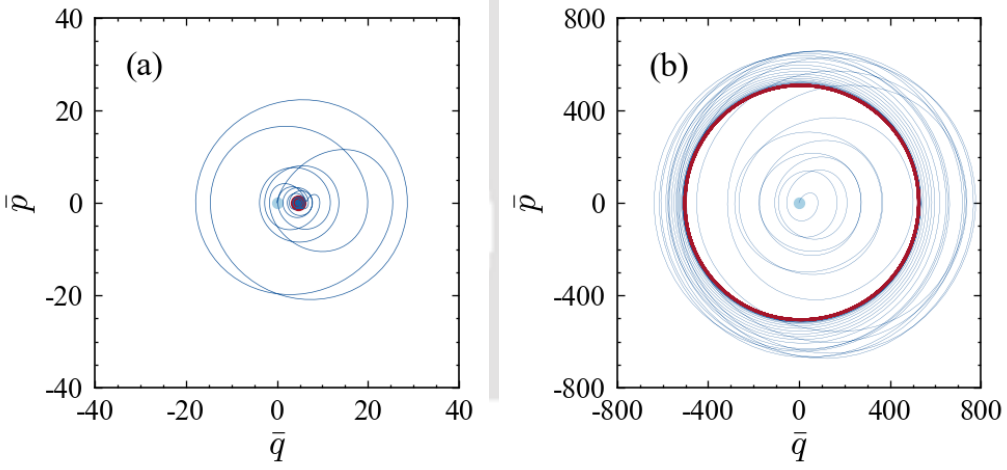


**Figure 1.5:** Phase-space trajectories for the time evolution of normalized classical position ($\bar{q} = \sqrt{m\omega_m}(\beta^* + \beta)/\sqrt{\hbar}$) and normalized classical momentum ($\bar{p} = i(\beta^* - \beta)/\sqrt{\hbar m\omega_m}$) obtained using (a) a red-detuned laser ($\Delta_0 = -\omega_m$) of amplitude $A_l = 10$ and (b) a blue-detuned laser ($\Delta_0 = \omega_m$) of amplitude $A_l = 50$. The light blue dots denote the initial conditions for the simulation ($\bar{q} = 0, \bar{p} = 0$). The red dot in (a) highlights the fixed point into which the mechanical mode settles down. The red loop in (b) illustrates the limit cycle dynamics of the mechanical mode. In both figures, we have plotted the dynamics of the system upto $t = 10^3/\omega_m$. Other parameters (in units of $\omega_m$) are $g_0 = 0.005$, $\gamma = 0.005$ and $\kappa = 0.15$.

TH-3401_186121105

Cavity optomechanical systems are typical nonlinear dynamical systems in the classical regime. The time evolution of their classical mean amplitudes can trace different types of attractors. Two such attractor diagrams for the mechanical mode of the cavity optomechanical system described in Section 1.1 are depicted in Figure 1.5. It can be seen here that the phase-space trajectory of the classical dynamics in Figure 1.5 (a) settles down into a fixed point, which is analogous to the steady state behaviour discussed earlier. Whereas, from Figure 1.5 (b), it is evident that optomechanical systems also exhibit limit-cycle oscillations. When systems with such self-sustained dynamics are coupled to other oscillating components whose frequencies are close to that of the self-oscillations, their motions tend to synchronize with each other. For coupled systems, synchronization may initially appear between their classical mode amplitudes and the classical synchronized dynamics may in turn result in the synchronization of their quantum fluctuations [51, 52]. Although different proposals attempt to quantify the degree of this quantum synchronization via different measures [28], we shall restrict ourselves to the widely accepted measure proposed by Mari *et. al.* [15]. This measure employs the effective phase mismatch between the quantum fluctuations in the rotating frame of the classical phases. Using this approach, one can estimate the degree the quantum phase synchronization between two components as,

> RECALL
>
> *Due to the uncertainty principle in quantum mechanics, there is no clear identification of phase-space trajectories for the quantum fluctuations of a system.*

$$S_p = \frac{1}{\sqrt{2}}\langle P_-^2\rangle^{-1}, \tag{1.19}$$

where $P_- = \tilde{P}_j - \tilde{P}_{j'}$ represents the mismatch between the rotated phase quadratures $\tilde{P}_k$ ($k \in \{j, j'\}$) such that $\tilde{P}_k e^{i\phi_k} = P_k$ are the momentum quadratures of the respective modes; $\phi_k = \arg[\langle \mathcal{O}_k \rangle]$ being the corresponding classical phases. In terms of the block form in Equation (1.18) containing the correlation elements for the constituent modes, we can rewrite this as

$$S_p = \left(\tilde{\mathcal{V}}_{11} + \tilde{\mathcal{V}}_{33} - 2 \times \tilde{\mathcal{V}}_{13}\right)^{-1}, \tag{1.20}$$

where $\tilde{\mathcal{V}} = \mathbf{R}\mathcal{V}\mathbf{R}^T$ is the phase-rotated correlation matrix (0-indexed), with $\mathbf{R} = \bigoplus_{k\in\{j,j'\}} \begin{pmatrix} \cos\phi_k & \sin\phi_k \\ -\sin\phi_k & \cos\phi_k \end{pmatrix}$ containing the classical rotation matrices.

TH-3401_186121105

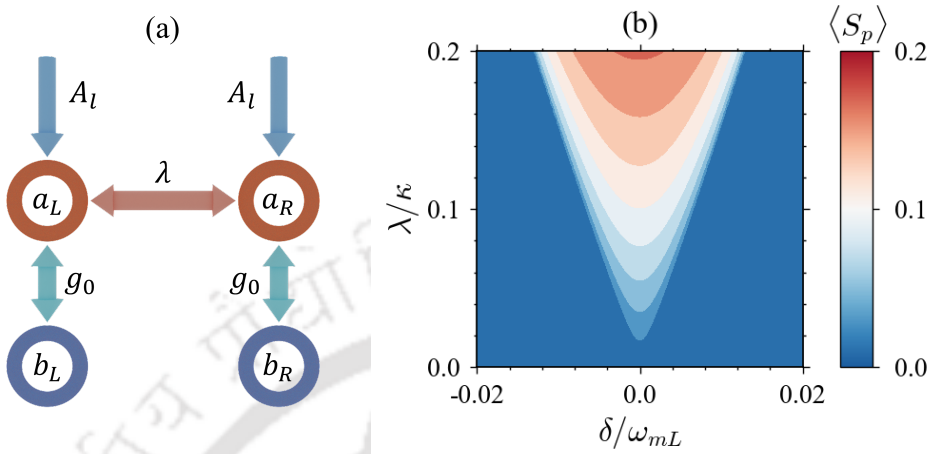


**Figure 1.6:** (a) A figurative model of two cavity optomechanical systems coupled using an optical channel of strength $\lambda$, and driven by lasers of amplitude $A_l$ and detuning $\Delta_{0j}$ ($j \in \{L, R\}$). $a_j$ and $b_j$ denote their optical and mechanical annihilation operators interacting with strengths $g_j$. The optical energies decay at a rate of $\kappa$ whereas the damping rate of the mechanical energies, (frequencies $\omega_{mj}$ and mean thermal occupancies $n_{th_j}$) is $\gamma$. (b) Behaviour of time-averaged quantum phase synchronization ($\langle S_p \rangle = \tau^{-1} \int_{t_0}^{t_0+\tau} S_p(t)dt$) with variation in the normalized detuning ($\delta/\omega_{mL} = \omega_{mR}/\omega_{mL} - 1$) and the normalized coupling strength of the optical channel ($\lambda/\kappa$). Here, $\tau = 10 \times 2\pi/\omega_m$ and $t_0$ is chosen in such a way that $t_{\max} = t_0 + \tau = 10^3/\omega_{mL}$. The parameters used (in units of $\omega_{mL}$) are $A_l = 52$, $g_0 = 0.005$, $\gamma = 0.01$ and $\kappa = 0.3$, with $\Delta_{0j} = \omega_{mj}$ and $n_{th_L} = n_{th_R} = 0$.

To demonstrate this measure, let us consider two nearly identical blue-detuned optomechanical cavities ($j \in \{L, R\}$) coupled using an optical channel of strength $\lambda$ as depicted in Figure 1.6 (a). We assume that the coupling Hamiltonian $H_c = -\hbar\lambda(a_L^\dagger a_R + a_L a_R^\dagger)$ characterizes a photon-hopping interaction between the two cavities. Due to the optical channel, the mechanical modes of the individual systems now get coupled to one another indirectly, and thereby, display quantum phase synchronization after a transient period. Figure 1.6 (b) shows the variation of time-averaged values of this synchronization with change in the detuning between the two mechanical frequencies and the optical channel's coupling strength. This variation is a classic example of the Arnold tongue — a characteristic feature in classical synchronization. We shall discuss such classical signatures in more detail and analyze quantum phase synchronization in coupled optomechanical systems in Chapter 2.

TH-3401_186121105

### 1.2.2 Optomechanically Induced Transparency

An interesting outcome of interference is observed when a weak probe laser is introduced alongside the laser drive pumping an optomechanical cavity in the resolved sideband regime. When the detuning of the probe beam from the pump is close to the mechanical frequency, the anti-Stokes sideband of the pump field (originating due to scattering via the mechanical mode) interferes destructively with the probe field. This suppresses the build-up of the intracavity field at the probe frequency and renders the probe transparent.

NOTE

*An analogous effect in Λ-type atomic systems is EIT [30], where destructive interference between the excitation pathways of the system result in the transmission of a weak probe beam in the presence of a strong control field.*

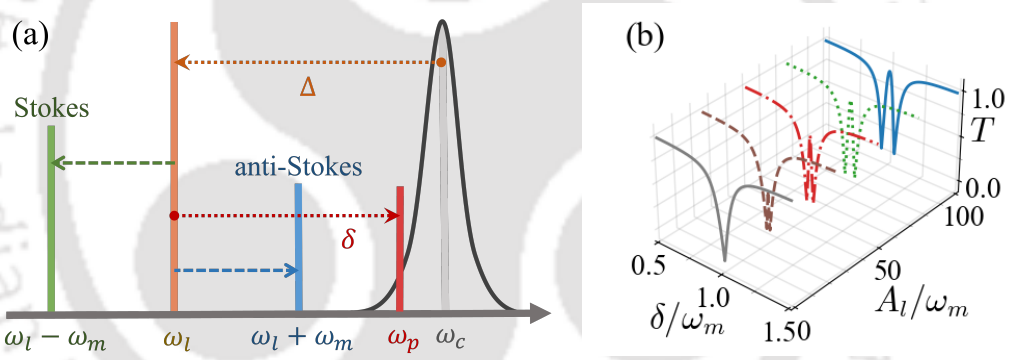


**Figure 1.7:** (a) Positions of the pump and probe frequencies with reference to the cavity frequency and the mechanically-scattered Stokes and anti-Stokes sidebands. (b) Variation of transmission at the probe frequency ($T$) with change in the normalized probe detuning ($\delta/\omega_m = (\omega_p - \omega_l)/\omega_m$) and the normalized pump amplitude ($A_l/\omega_m$) at the resonance condition $\Delta_s = -\omega_m$. Other parameters (in units of $\omega_m$) are $g_0 = 0.0005$, $\gamma = 0.005$ and $\kappa = 0.15$, with $\mu = 0.5$.

To derive an analytical expression for the output field of the cavity at the probe frequency, we first rewrite the Hamiltonian in Equation (1.5) by adding the probe laser term $H_p = i\hbar A_p(a^\dagger e^{-i\delta t} - a e^{i\delta t})$. Here, $A_p$ ($\ll A_l$) is the amplitude of the probe beam and $\delta = \omega_p - \omega_l$ is its detuning from the pump, $\omega_p$ denoting the frequency of the probe. Figure 1.7 (a) illustrates this configuration of the probe laser, the pump laser and its first-order sidebands.

TH-3401_186121105

The classical dynamics described by Equation (1.8) can then be rewritten as

$$\dot{\alpha} = -\left(\frac{\kappa}{2} - i\Delta\right)\alpha + A_l + A_p e^{-i\delta t}, \tag{1.21a}$$

$$\dot{\beta} = -\left(\frac{\gamma}{2} + i\omega_m\right)\beta + ig_0\alpha^*\alpha. \tag{1.21b}$$

Since the amplitude of the probe beam is much smaller than that of the pump, it is safe to assume that, along with the steady-state intracavity field, the primary contributions in the output transmission are from the first-order mechanically-scattered sidebands of the strong pump field. Using an ansatz of the form $\alpha = \alpha_s + A_- e^{-i\delta t} + A_+ e^{i\delta t}$ and $\beta = \beta_s + B_- e^{-i\delta t} + B_+ e^{i\delta t}$, we then obtain a set of linear equations at the Stokes and anti-Stokes frequencies as

$$A_-\left(\frac{\kappa}{2} - i\Delta_s - i\delta\right) - ig_0\left(B_- + B_+^*\right)\alpha_s = A_p, \tag{1.22a}$$

$$A_+^*\left(\frac{\kappa}{2} + i\Delta_s - i\delta\right) + ig_0\left(B_- + B_+^*\right)\alpha_s^* = 0, \tag{1.22b}$$

$$B_-\left(\frac{\gamma}{2} + i\omega_m - i\delta\right) - ig_0\left(\alpha_s^* A_- + \alpha_s A_+^*\right) = 0, \tag{1.22c}$$

$$B_+^*\left(\frac{\gamma}{2} - i\omega_m - i\delta\right) + ig_0\left(\alpha_s^* A_- + \alpha_s A_+^*\right) = 0, \tag{1.22d}$$

where we have used $\Delta_s = \Delta_0 + g_0(\beta_s^* + \beta_s)$ as the effective steady-state detuning. Solving the above equations gives us the sideband amplitude as

$$A_- = \left(\frac{\mathcal{K}_+\mathcal{G}_+\mathcal{G}_- + 2ig_0^2\omega_m\left|\alpha_s\right|^2}{\mathcal{K}_+\mathcal{K}_-\mathcal{G}_+\mathcal{G}_- + 4g_0^2\Delta_s\omega_m\left|\alpha_s\right|^2}\right)A_p, \tag{1.23}$$

with $\mathcal{K}_\pm = \kappa/2 \pm i\Delta_s - i\delta$ and $\mathcal{G}_\pm = \gamma/2 \pm i\omega_m - i\delta$. This amplitude represents the intracavity field at the probe frequency. The transmission intensity at the probe frequency can then be obtained using the input-output relation as

$$T = \left|\frac{\sqrt{\mu\kappa}A_- - A_p/\sqrt{\mu\kappa}}{A_p/\sqrt{\mu\kappa}}\right|^2 = \left|1 - \frac{\mu\kappa A_-}{A_p}\right|^2, \tag{1.24}$$

where $\mu$ is the laser-cavity coupling parameter.

We plot the transmission of light through the cavity at the probe frequency when $\Delta = -\omega_m$ and the probe beam is close to the resonance condition $\delta = \omega_m$ in Figure 1.7 (b). As the power of the pumping laser drive increases, one can see that a window of optomechanically induced transparency emerges at resonance. In Chapter 3, we shall investigate this phenomena in a more complex system and probe deeper into its consequent effects.

TH-3401_186121105

### 1.2.3 Quantum Entanglement

The dispersive coupling between the optical and mechanical elements of an optomechanical cavity may also give rise to a finite amount of entanglement. By expressing the correlations between them in the form of Equation (1.18), we can quantify the degree of Gaussian quantum entanglement as [19, 53],

$$E_{\mathcal{N}} = \max[0, -\ln[2\eta_-]], \tag{1.25}$$

where $\eta_- = 2^{-1/2}\{\tilde{\Sigma}[\mathcal{V}] - (\tilde{\Sigma}[\mathcal{V}]^2 - 4\det[\mathcal{V}])^{1/2}\}^{1/2}$, with $\tilde{\Sigma}[\mathcal{V}] = \det[\mathcal{A}] + \det[\mathcal{B}] - 2\det[\mathcal{C}]$. This figure of merit is known as logarithmic negativity.

DIGRESSION 1.6

**Partial Positive Transpose and the Simon's Criteria**

Using a local symplectic operation $\mathbf{S}_l$ that preserves the compact uncertainty relation, the block correlation matrix $\mathcal{V}$ can be diagonalized as [54]

$$\mathcal{V} = \mathbf{S}_l \mathcal{V}_s \mathbf{S}_l^T; \quad \mathcal{V}_s = \begin{pmatrix} a & 0 & c_1 & 0 \\ 0 & a & 0 & c_2 \\ c_1 & 0 & b & 0 \\ 0 & c_2 & 0 & b \end{pmatrix},$$

such that $\det[\mathcal{A}] = a^2$, $\det[\mathcal{B}] = b^2$, $\det[\mathcal{C}] = c_1 c_2$ and $\det[\mathcal{V}]$ are invariants of the transformation. Under partial positive transposition [55], this becomes

$$\tilde{\mathcal{V}}_s = \Lambda \mathcal{V}_s \Lambda = \begin{pmatrix} a & 0 & c_1 & 0 \\ 0 & a & 0 & -c_2 \\ c_1 & 0 & b & 0 \\ 0 & -c_2 & 0 & b \end{pmatrix},$$

where $\Lambda = \mathrm{Diag}[1, 1, 1, -1]$ performs a phase-space mirror reflection on the second state [56]. It is important to note that under this transpose operation, only the cross-correlation matrix of $\tilde{\mathcal{V}}_s$ changes sign, i.e., $\det[\tilde{\mathcal{C}}] = -\det[\mathcal{C}]$. One can then obtain the positive symplectic eigenvalues of $\tilde{\mathcal{V}}_s$ as

$$\eta_\pm = \frac{1}{\sqrt{2}} \sqrt{\Sigma[\tilde{\mathcal{V}}_s] \pm \sqrt{\Sigma[\tilde{\mathcal{V}}_s]^2 - 4\det[\tilde{\mathcal{V}}_s]}},$$

with $\Sigma[\tilde{\mathcal{V}}_s] = \det[\tilde{\mathcal{A}}] + \det[\tilde{\mathcal{B}}] + 2\det[\tilde{\mathcal{C}}] = \det[\mathcal{A}] + \det[\mathcal{B}] - 2\det[\mathcal{C}] = \tilde{\Sigma}[\mathcal{V}]$ such that $\det[\tilde{\mathcal{V}}_s] = \eta_\pm^2 \Sigma[\tilde{\mathcal{V}}_s] - \eta_\pm^4$. Thus, Simon's necessary and sufficient

TH-3401_186121105

condition for separability under partial transposition criterion results in [57]

$$\begin{aligned} 4\left(ab-c_1^2\right)\left(ab-c_2^2\right) &\geq \left(a^2+b^2+2\left|c_1c_2\right|\right)-\frac{1}{4} \\ \Rightarrow 4\det[\tilde{\mathcal{V}}_s] &\geq \Sigma[\tilde{\mathcal{V}}_s]-\frac{1}{4} \end{aligned}$$

Therefore, a necessary and sufficient condition for entanglement between the two states can be imposed on the smallest symplectic eigenvalue as [58]

$$\eta_- < \frac{1}{2},$$

which is equivalent to the logarithmic negativity quantifier.

Figure 1.8 (a) shows the optomechanical entanglement in the steady-state of the system discussed in Section 1.1. Entanglement may also be observed across the components of coupled subsystems. We shall elaborate on the behaviour of entanglement and propose methods to enhance it in Chapter 4.

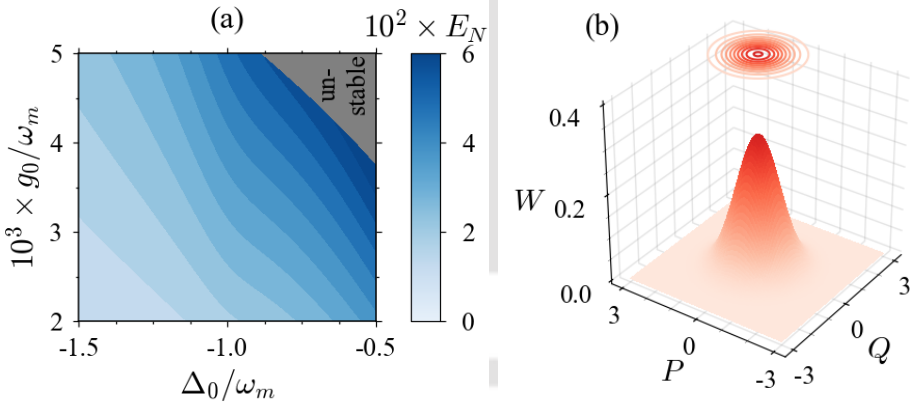


**Figure 1.8:** (a) Stationary entanglement ($E_N$) between the optical and mechanical modes obtained at different values of the normalized laser detuning ($\Delta_0/\omega_m$) and the optomechanical coupling constant ($g_0/\omega_m$). The gray region marks dynamical instability and multistability. (b) Single-mode Wigner distribution ($W$) for the mechanical mode at $t = 10^3/\omega_m$ obtained using a blue-detuned laser ($\Delta_0 = \omega_m$) with a coupling constant of $g_0 = 0.0001$. Other parameters used (in units of $\omega_m$) are $A_l = 10$, $\gamma = 0.005$ and $\kappa = 0.15$, with $n_{th} = 0$.

TH-3401_186121105

### 1.2.4 Mechanical Squeezing

The mechanical mode of a quantum harmonic oscillator is ideally lower-bound by a quadrature variance of $\mathbf{V}_{jj} = 0.5$ (or equivalently 3 dB). But one can increase the precision in the measurement of one of these quadratures at the expense of increasing the variance of the other, leading to a "squeezing" of the mode. The degree of this squeezing (expressed in decibels as $-10\log_{10}[\mathbf{V}_{jj}]$) can be visualized in the phase-space by the Wigner probability distribution function of the mechanical mode [12]

> **RECALL** *A coherent Gaussian state of a quantum harmonic oscillator contains minimum uncertainty.*

$$W = \frac{1}{2\pi\sqrt{\det[\mathbf{V}_m]}} \exp\left[\frac{-\mathbf{u}_m^T \mathbf{V}_m^{-1} \mathbf{u}_m}{2}\right], \tag{1.26}$$

where $\mathbf{u}_m$ is the vector of the mechanical mode's fluctuation quadratures and $\mathbf{V}_m$ is the $2\times2$ correlation matrix of the mechanical mode. This measure can also be used to visualize multi-mode squeezing in coupled quantum systems by appropriately scaling the quadrature vector and the correlation matrix.

> **NOTE**
>
> *Mechanical squeezing can also be generated from the creation or annihilation of correlated photon-phonon pairs. The corresponding Hamiltonian of their interaction gets amplified in the presence of parametric processes in the blue-detuned regime. Such a two-mode squeezing effect typically results in higher degrees of entanglement between the optical and mechanical modes [59].*

Figure 1.8 (b) demonstrates a $\sim 2.83$ dB variance of the mechanical position for the system described in Section 1.1 driven by a blue-detuned laser into a steady state. One can also calculate the corresponding value from the analytical expressions of the steady-state variances of the quadratures obtained by solving Equation (1.16). In Chapter 4, we shall discuss multiple scenarios where we enhance the precision in the measurement of the mechanical position by increasing the variance of the corresponding momentum quadrature and study the effect of two-mode squeezing in the enhancement of bipartite entanglement.

TH-3401_186121105

## 1.3 Numerical Methods and The Toolbox

With the linearization approximation, our numerical simulations mostly reduce to solving coupled ordinary differential equations for the classical mode amplitudes and the correlation matrix elements introduced in Section 1.1 using standard numerical techniques. Once these values are obtained, we estimate the degree of the classical and quantum phenomena based on their established measures as discussed in Section 1.2. The routine that we use to obtain most of the results presented in this thesis is illustrated in Figure 1.9.

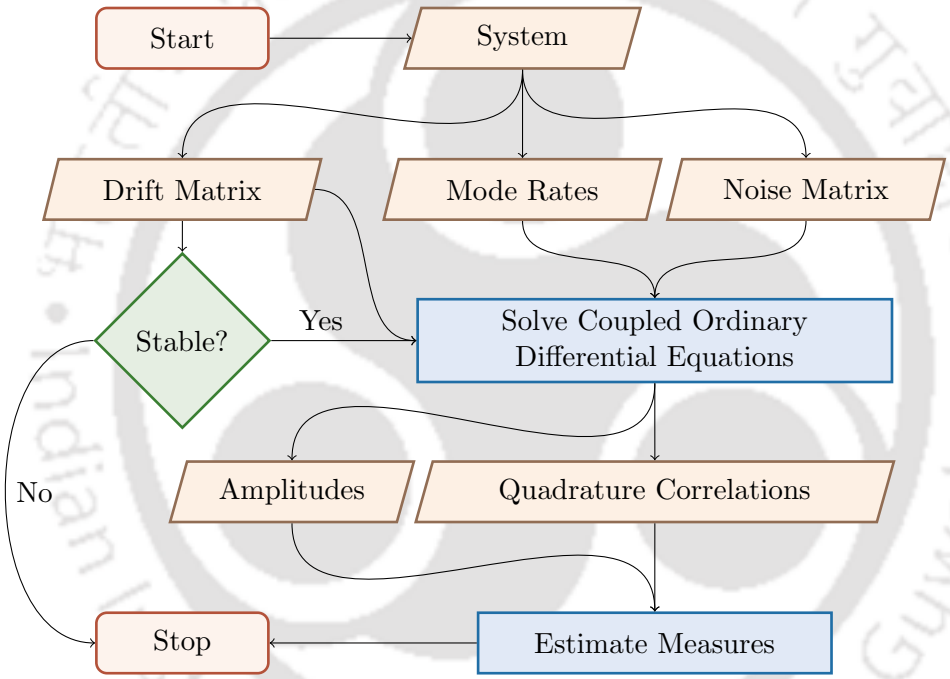


**Figure 1.9:** Workflow to simulate a linearized system with fixed parameters.

To implement the above workflow in a parallel manner, we developed an object-oriented Python library — the quantum optomechanics toolbox [60]. This toolbox (packaged as `qom`) is a wrapper-styled, scalable framework featuring multiple modules to calculate stationary and dynamical properties of many-body optomechanical systems. Its solvers also contain several options to fine-tune the simulations. The key advantages of this toolbox can be summarized as (i) automatically-managed loopers with parallelization utilities, (ii) configurable solvers to obtain dynamics, stability and measures, and (iii) customizable plotters to work across libraries with a common syntax.

TH-3401_186121105

Apart from supporting linearized many-body quantum optomechanical systems, the toolbox also contains modules for classical nonlinear dynamical systems and open quantum systems in general. In addition to this, it features a graphical user-interface that reduces the process of simulating different sets of parameters for each user-defined system to just a few clicks! It, therefore, serves as an easy-to-use alternative towards writing explicit code and avoiding repetitive exercises to present the results. All the figures presented in this thesis are plotted using this `qom` toolbox.

## 1.4 Structure of the Thesis

The thesis contains five chapters that cover some of the works completed during the doctoral tenure. This introductory chapter familiarizes the reader to the field of optomechanics and provides a flavour of the various phenomena that can be studied in such systems. The subsequent chapters are divided on the basis of these phenomena, where we detail our corresponding works. In what follows, we briefly outline the contents of these individual chapters.

**Chapter 2:** In this chapter, we discuss quantum synchronization in much more detail, comparing different approaches to measure it and relating the significance of these measures to physical observables. We then report our work where we analyze the dynamical behaviour of quantum phase synchronization in two optomechanical systems coupled via an unidirectional optical channel. The idea behind the study of such phenomena in hybrid optomechanical systems is to develop stable networks of synchronizable quantum systems that can relay information with a very less amounts of phase noises.

**Chapter 3:** Here, we introduce an annularly-trapped Bose-Einstein condensate placed inside a cavity and driven by strong pump beams carrying orbital angular momentum. We briefly discuss the formulation of an analogous optomechanical Hamiltonian that can describe such a system and present our work involving a weak probe beam passing through this system. We systematically analyze the transmission profile of the probe beam and the modifications in its propagation caused by the atomic condensate. Our approach connects semi-classical interference to atomic rotation sensing and highlights how methods pertaining to optomechanics can be utilized to extract information about the condensate in a minimally destructive manner.

TH-3401_186121105

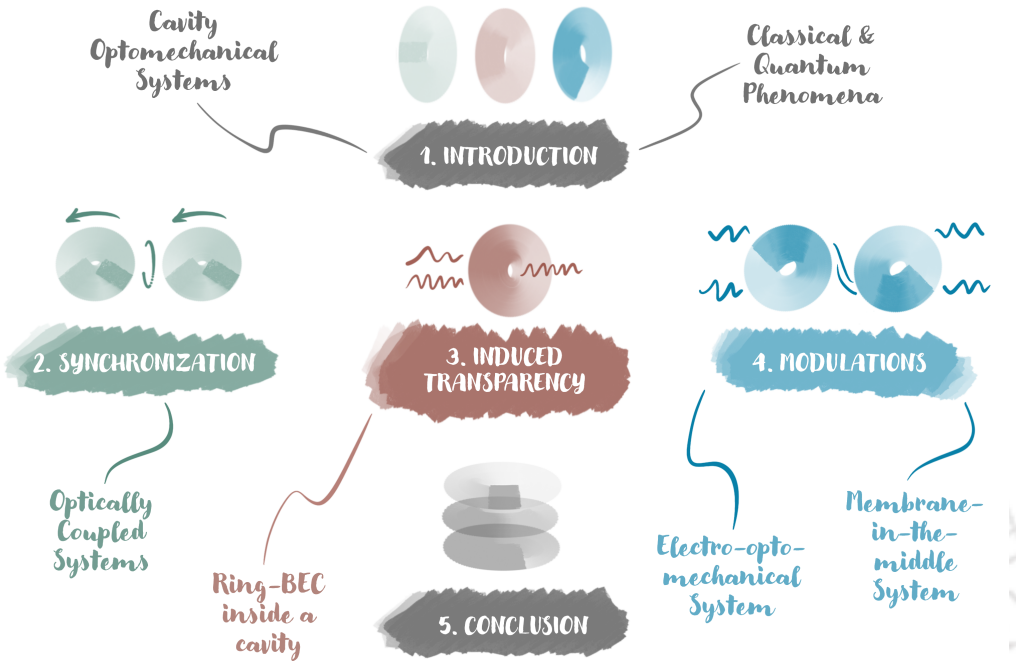


**Figure 1.10:** Structure of the thesis.

**Chapter 4:** This chapter deals with the area of modulated optomechanics. We begin by introducing different ways by which one can modulate the dynamics of optomechanical systems. We then report our works where we analyzed two modulated systems — a membrane-in-the-middle optomechanical cavity and an electro-optomechanical system. The motivation behind such studies is to generate higher degrees of entanglement between optical, mechanical and electrical components and to enhance mechanical squeezing.

**Chapter 5:** We summarize all our works in this chapter, highlighting their novelties, caveats and scalability. We also revisit the key findings of the discussed works, connect them to potential near-future applications and discuss the scope of further research in these areas.

TH-3401_186121105

TH-3401_186121105

CHAPTER

2

# Synchronizing Coupled Quantum Systems

Synchronization is an ubiquitious phenomena observed in an extremely wide spectrum of systems — from nanoscale masses to astronomical objects [23]. It's first account dates back to the $17^{\text{th}}$ century where the motion of two maritime pendulum clocks was formally analyzed by Christian Huygens [22]. And over the years, the phenomena of synchronization has been extensively studied in numerous physical, biological, chemical as well as social systems [61]. Although one can simply describe synchronized behaviour as a sympathetic adjustment of intrinsic rhythms between coupled bodies, the analysis of the coupled nonlinear dynamics which lead such complex systems to eventually oscillate in unison is an engaging (and equally surprising) field of research!

---

This chapter is based on our work published in J. Phys. Commun. **5**, 115006 (2021), titled *Switching of Quantum Synchronization in Coupled Optomechanical Oscillators* and authored by Sampreet Kalita, Subhadeep Chakraborty and Amarendra K. Sarma [62, 63] (©2021 The Author(s) under the Creative Commons Attribution 4.0 license).



TH-3401_186121105

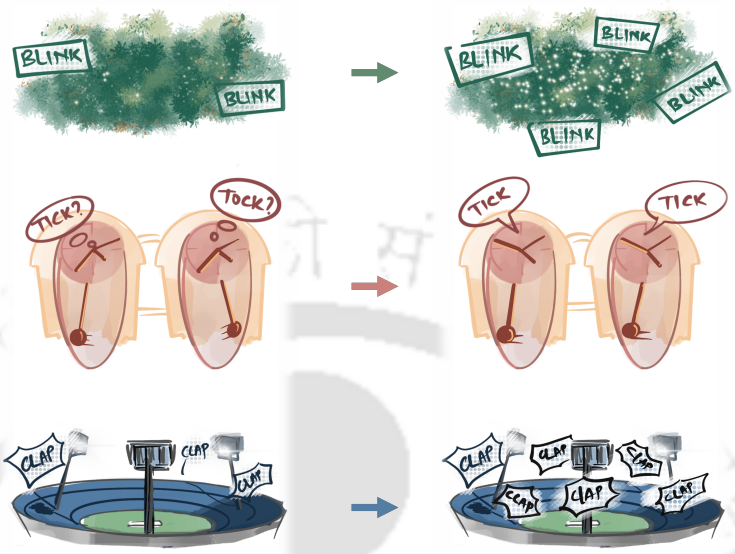


**Figure 2.1:** Examples of synchronization in different types of systems (*top to bottom*): flashing of fireflies, oscillation of pendulum clocks and slow applause in stadiums. The illustrations on the left denote the initial transients of each system whereas the ones on the right denote the synchronized phases.

Spontaneous synchronization plays a significant role in time-keeping and design of communication protocols for classical information processing [24, 25]. Quantum analogues of this nonlinear dynamical phenomenon have also been explored in diverse models for similar applications in the quantum domain. These include the analysis of van der Pol oscillators [64], Kerr-anharmonic oscillators [65], atomic ensembles [66], ions [67], spin systems [68] and hybrid architectures [69, 70]. As demonstrated in Section 1.2.1, synchronization can even emerge in optomechanical systems between coupled mechanical elements that undergo limit-cycle dynamics. In fact, this has been experimentally validated using optically coupled micro-disk resonators [51] and optical racetrack cavities with integrated mechanical oscillators [71]. This has enthused the investigation of synchronization in many-body quantum networks [72–74]. Several proposals to enhance the degree of quantum synchronization have also been reported, notable among them being the addition of secondary laser drives and squeezed driving [75, 76]. Thermal noise driven steering of synchronous behaviour and the study of chaotic synchronization are other areas of active research in the field [77–79].

TH-3401_186121105

In this chapter, we present our theoretical exploration of quantum phase synchronization in optically coupled optomechanical oscillators. The specific choice of exploiting the optical coupling as opposed to the mechanical one is motivated by recent theoretical investigations [29, 77, 80], and experimental demonstrations [51, 81] using optical channels. We first begin by discussing the measure used to quantify quantum phase synchronization in Section 2.1. We then describe the unidirectionally-coupled configuration of near-identical optomechanical systems and discuss the novelty of our results in Section 2.2. We also systematically compare this system with the bidirectionally-coupled system introduced in Section 1.2.1. Finally, we summarize our findings and mention the applications of our work in Section 2.3.

## 2.1 Quantum Phase Synchronization

As discussed in Section 1.2.1, we employ the criteria in Equation (1.19) for the estimation of quantum synchronization in our works, which reads as

$$S_p = \frac{1}{\sqrt{2}} \frac{1}{\langle \left( \tilde{P}_j - \tilde{P}_{j'} \right)^2 \rangle}, \tag{2.1}$$

where $\tilde{P}_k$ ($k \in \{j, j'\}$) are the rotated phase quadratures with $\tilde{P}_k e^{i\phi_k} = P_k$ as the momentum quadratures of the respective modes and $\phi_k = \arg[\langle \mathcal{O}_k \rangle]$ as their corresponding classical phases. This figure of merit can be thought of as an inverse quantifier of the effective mismatch between the phase quadratures of the oscillators. Hence, higher values of $S_p$ imply a lower degree of phase noise between the two oscillators. This can be visualized from Figure 2.2.

It can be immediately seen here that, (i) since $S_p$ incorporates the classical phase $\phi_k$, the mechanical mode amplitudes ($\beta_k = \bar{\beta}_k + r_k e^{i\phi_k}$) must attain limit-cycles ($r_k > 0$) in the classical dynamics for a physically plausible value of quantum phase synchronization, and (ii) since $S_p$ is defined in the frame of the limit-cycle dynamics, it must contain signatures of the classical nonlinear dynamics alongside the quantum signatures. Whereas these are analogous to the necessary conditions for synchronization [23], the dynamical stability of the system needs to be ascertained separately using the drift matrix. Moreover, because of the relative difference between the phase quadratures in Equation (2.1), this measure only reflects the strength of synchronization and cannot determine its type (in-phase, anti-phase or other values).

TH-3401_186121105

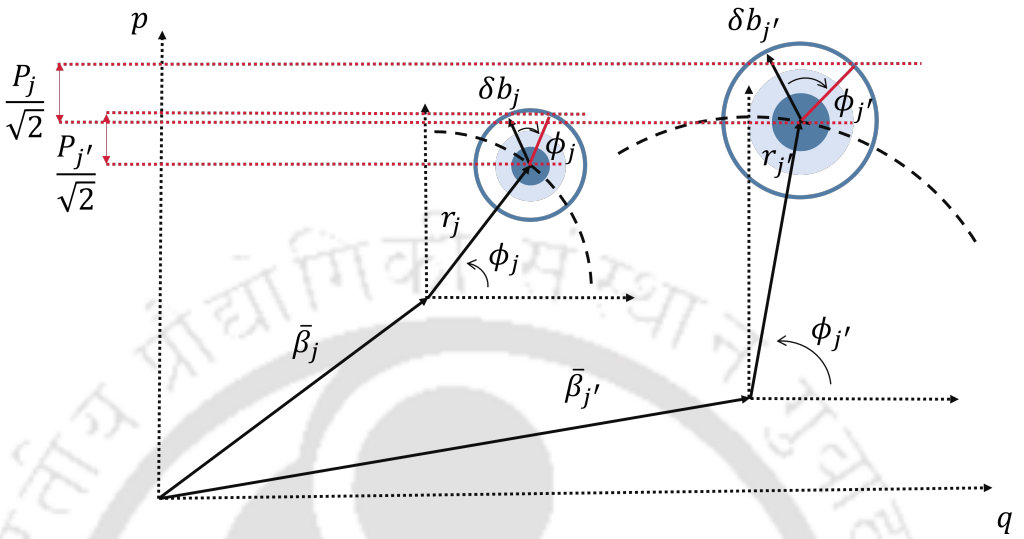


**Figure 2.2:** Interpretation of rotated phase-fluctuations in phase-space.

To comment on the type of synchronization, we take into account another widely-accepted measure for classical and quantum correlations known as the Pearson correlation factor [28]. In terms of the fluctuation quadratures relevant to the measure of quantum phase synchronization in Equation (2.1), this measure reads as [28]

$$C = \frac{\int_{t_0}^{t_0+\tau} \langle P_j P_{j'} \rangle dt}{\sqrt{\int_{t_0}^{t_0+\tau} \langle P_j^2 \rangle dt \int_{t_0}^{t_0+\tau} \langle P_{j'}^2 \rangle dt}}, \tag{2.2}$$

where $t_0$ and $\tau$ respectively denote the initial time and the duration for which the measure is being calculated. While $C \sim 1$ $(-1)$ characterizes an in-phase (anti-phase) evolution, $C \sim 0$ refers to the absence of any correlation.

**NOTE**

*Numerous efforts have also been made to connect the onset of quantum synchronization to the generation of quantum correlations [67, 82–87]. However, determining a concrete relation between the two and formalizing an universal measure of quantum synchronization is still a challenging task [15, 27, 88].*

TH-3401_186121105

## 2.2 Switching of Quantum Synchronization

Before defining the unidirectional configuration, let us rewrite the Heisenberg Langevin equations for the bidirectional configuration in Figure 1.6(a) as

$$\dot{a}_j = -\left(\frac{\kappa}{2} - i\Delta_{0j}\right) a_j + ig_0\left(b_j^\dagger + b_j\right) a_j + i\lambda a_{j'} + A_l + \sqrt{\kappa}a_{in_j}, \quad (2.3a)$$

$$\dot{b}_j = -\left(i\omega_{mj} + \frac{\gamma}{2}\right) b_j + ig_0 a_j^\dagger a_j + \sqrt{\gamma}b_{in_j}, \quad (2.3b)$$

where $j \in \{L, R\}$ ($j' \in \{L, R\} - \{j\}$ unless specified otherwise). Here, the $L$ and $R$ denote the left and right systems respectively while the rest of the symbols have their usual meaning. The reversible exchange of photons between the two systems is denoted by the Hermitian Hamiltonian $H_c = -\hbar\lambda(a_L^\dagger a_R + a_L a_R^\dagger)$, where $\lambda$ is the coupling strength of the optical channel. Using a linearized description of the quantum dynamics and proceeding in the same way as detailed in Section 1.1, we obtain Figure 1.6 (b). It may be noted here that each individual point in the figure represent a time-averaged value of $S_p$, obtained using the last 10 cycles of oscillation.

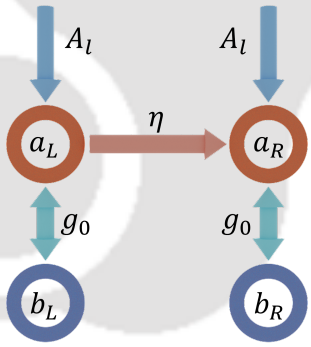


**Figure 2.3:** A pictorial depiction of the unidirectionally coupled systems.

We now proceed to the unidirectional configuration, illustrated in Figure 2.3, where the two optomechanical oscillators are arranged in a forward-fed manner. Such a cascaded geometry can be modelled using [89–91]

$$a_{in_R}(t) \to \sqrt{\eta}a_L^{out}(t - \tau') + \sqrt{1-\eta}a_{in_R}(t), \quad (2.4)$$

where $\eta \leq 1$ is the transmission loss between the optical cavities and $\tau'$ is the time required for light to travel from the left to the right cavity. However, for theoretical simplicity, we will consider $\tau' = 0$ in the rest of our discussion.

TH-3401_186121105

NOTE

*This configuration is different from the bidirectional one in the sense that photons are only allowed to leave the left cavity and enter the right one. Such a behaviour can be described by a non-Hermitian dissipative Hamiltonian.*

The full dissipative dynamics can then be described by

$$\dot{a}_L = -\left(\frac{\kappa}{2} - i\Delta_{0L}\right) a_L + ig_0\left(b_L^\dagger + b_L\right) a_L + A_l + \sqrt{\kappa_L} a_{in_L}, \tag{2.5a}$$

$$\dot{a}_R = -\left(\frac{\kappa}{2} - i\Delta_{0R}\right) a_R + ig_0\left(b_R^\dagger + b_R\right) a_R - \sqrt{\eta}\kappa a_L + \left(\sqrt{\eta} + \sqrt{1-\eta}\right) A_l + \sqrt{\kappa_R}\sqrt{\eta} a_{in_L} + \sqrt{\kappa_R}\sqrt{1-\eta} a_{in_R}, \tag{2.5b}$$

$$\dot{b}_j = -\left(\frac{\gamma}{2} + i\omega_{mj}\right) b_j + ig_0 a_j^\dagger a_j + \sqrt{\gamma_j} b_{in_j}, \tag{2.5c}$$

which gives us the drift matrix as (refer to Section 1.1 for its derivation)

$$\begin{pmatrix} -\frac{\kappa}{2} & -\Delta_L & -2G_{L_{\mathrm{Im}}} & 0 & 0 & 0 & 0 & 0 \\ \Delta_L & -\frac{\kappa}{2} & 2G_{L_{\mathrm{Re}}} & 0 & 0 & 0 & 0 & 0 \\ 0 & 0 & -\frac{\gamma}{2} & \omega_{mL} & 0 & 0 & 0 & 0 \\ 2G_{L_{\mathrm{Re}}} & 2G_{L_{\mathrm{Im}}} & -\omega_{mL} & -\frac{\gamma}{2} & 0 & 0 & 0 & 0 \\ -\mu & 0 & 0 & 0 & -\frac{\kappa}{2} & -\Delta_R & -2G_{R_{\mathrm{Im}}} & 0 \\ 0 & -\mu & 0 & 0 & \Delta_R & -\frac{\kappa}{2} & 2G_{R_{\mathrm{Re}}} & 0 \\ 0 & 0 & 0 & 0 & 0 & 0 & -\frac{\gamma}{2} & \omega_{mR} \\ 0 & 0 & 0 & 0 & 2G_{R_{\mathrm{Re}}} & 2G_{R_{\mathrm{Im}}} & -\omega_{mR} & -\frac{\gamma}{2} \end{pmatrix}. \tag{2.6}$$

In deriving Equation (2.6), we have used $\Delta_j = \Delta_{0j} + g_0(\beta_j^* + \beta_j)$ as the effective detuning, $G_j = g_0\alpha_j = G_{j_{Re}} + iG_{j_{Im}}$ as the effective optomechanical coupling rate and $\mu = \sqrt{\eta}\kappa$. The corresponding noise correlation matrix is

$$\begin{pmatrix} \frac{\kappa}{2} & 0 & 0 & 0 & \mu & 0 & 0 & 0 \\ 0 & \frac{\kappa}{2} & 0 & 0 & 0 & \mu & 0 & 0 \\ 0 & 0 & \frac{\gamma}{2}\left(n_{th_L} + \frac{1}{2}\right) & 0 & 0 & 0 & 0 & 0 \\ 0 & 0 & 0 & \frac{\gamma}{2}\left(n_{th_L} + \frac{1}{2}\right) & 0 & 0 & 0 & 0 \\ \mu & 0 & 0 & 0 & \frac{\kappa}{2} & 0 & 0 & 0 \\ 0 & \mu & 0 & 0 & 0 & \frac{\kappa}{2} & 0 & 0 \\ 0 & 0 & 0 & 0 & 0 & 0 & \frac{\gamma}{2}\left(n_{th_R} + \frac{1}{2}\right) & 0 \\ 0 & 0 & 0 & 0 & 0 & 0 & 0 & \frac{\gamma}{2}\left(n_{th_R} + \frac{1}{2}\right) \end{pmatrix} \tag{2.7}$$

TH-3401_186121105

We numerically simulate the dynamics of the classical mode amplitudes and the correlation matrix elements and estimate the degree of quantum phase synchronization between the mechanical modes of the two systems. We find that, in contrast to the bidirectional configuration, the unidirectional configuration takes a longer time to reach synchronous behaviour. This can be attributed to the fact that the weighted classical nonlinearity entering the quantum dynamics, together with the intrinsic asymmetry associated with the unidirectionality of the configuration, hinder the sympathetic adjustment of rhythms in its mechanical oscillators, delaying their synchronization.

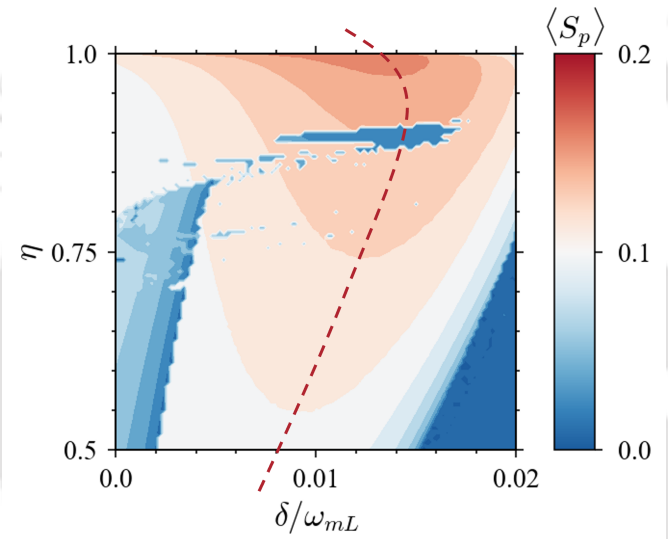


**Figure 2.4:** Time-averaged values of quantum phase synchronization ($\langle S_p \rangle$) with variation in the normalized detuning ($\delta/\omega_{mL}$) and the transmission loss ($\eta$). The red (dashed) line denotes the values of the detuning at which synchronization is maximum. Here, $\omega_{mL} t_{\max} = 10^4$. The parameters used (in units of $\omega_{mL}$) are $A_l = 52$, $g_0 = 0.005$, $\gamma = 0.01$ and $\kappa = 0.3$, with $\Delta_{0j} = \omega_{mj}$ and $n_{th_L} = n_{th_R} = 0$.

Another interesting effect of the unidirectionality can be observed when the detuning between the mechanical oscillators $\delta = \omega_{mR} - \omega_{mL}$ is varied. This is depicted in Figure 2.4, where we plot the time-averaged values of the synchronization, $\langle S_p \rangle = \tau^{-1} \int_{t_0}^{t_0+\tau} S_p(t) dt$. Here, $\tau = 10 \times 2\pi/\omega_m$ represents the time taken to complete the last 10 cycles of the numerical simulation. Unlike the case with the bidirectional configuration depicted in Figure 1.6, we find that synchronization gets suppressed in identical oscillators ($\delta = 0$)

TH-3401_186121105

and $\langle S_p \rangle$ is maximum at finite positive values of $\delta$. To reason this out, let us consider a simple scenario with asymptotic mechanical mode amplitudes $\beta_j = g_0|\alpha_j|^2/(\omega_{mj} - i\gamma/2)$. It is apparent that these amplitudes increase with increasing intracavity mode intensities ($|\alpha_j|^2$) and decrease for higher values of mechanical frequencies ($\omega_{mj}$). Thus, in the bidirectional configuration, when the mechanical oscillators are identical, i.e., $\omega_{mL} = \omega_{mR}$, the two oscillators are likely to acquire equal mode amplitudes, leading to a significant degree of synchronization between them. Whereas, for the unidirectional scenario, the amplitude of the right optical mode surpasses that of the left one for identical oscillators, resulting in higher $\beta_R$ values. Therefore, in this case, detuned oscillators with $\omega_{mR} > \omega_{mL}$ are the ones that acquire similar mechanical mode amplitudes with a constant phase difference and are more likely to synchronize than identical ones. To verify this analytically, we calculate the difference between the phonon numbers for either configurations in the linearized quantum regime (refer to the analytical expressions in Appendix A). We observe that the phonon numbers acquire equal magnitudes for identical oscillators in the bidirectional configuration, whereas, for the unidirectional configuration, the phonon number difference is non-zero at the zero detuning. Rather, we find that the corresponding non-zero detunings that result in equivalent number of phonons largely depend on $\eta$.

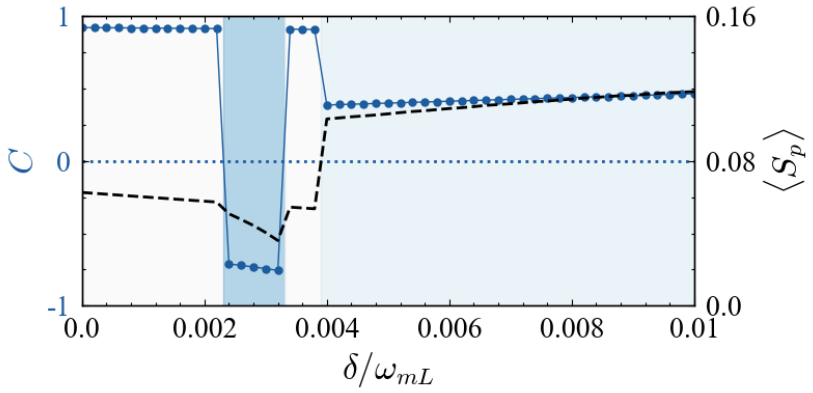


**Figure 2.5:** Time-averaged values of quantum phase synchronization, $\langle S_p \rangle$ (dashed black lines), and Pearson correlation factor, $C$ (solid blue circles), obtained for the unidirectional setup at different values of normalized detuning $\delta/\omega_{mL}$. The dotted blue line represents $C = 0$. The shaded areas in the figure denote that the quanta of phonons in the right mechanical mode is higher than that in the left one. Here, $\eta = 0.75$. Other parameters used are the same as those in Figure 2.4.

TH-3401_186121105

To gain further insights into the behaviour of synchronization in the unidirectional configuration, we take the Pearson correlation factor into account. Figure 2.5 depicts the variation of this measure with respect to the frequency detuning $\delta$ for a fixed value of the transmission loss parameter ($\eta = 0.75$). It can be seen here that the two oscillators undergo successive transitions, from in-phase to anti-phase, and back from anti-phase to in-phase states. Finally, the oscillators switch from a highly in-phase state ($C \approx 1$) to a moderately in-phase oscillatory state. Therefore, by choosing appropriate mechanical frequencies, one can selectively synchronize the two oscillators. And with higher degrees of synchronization, the phase noise between the two oscillators can also be reduced, making them useful in designing time-keeping and communication protocols.

NOTE

*Similar signatures of transitions can also be observed for higher number of thermal phonons.*

## 2.3 Summary of the Chapter

In this chapter, we systematically investigated the phenomenon of quantum phase synchronization in two unidirectionally coupled optomechanical systems and compared our results with the bidirectional case. We observed that irrespective of the coupling topologies, synchronization builds up after an initial transient. However, the time required for the mechanical modes to synchronize is longer in the unidirectional one. Moreover, while analyzing the dependence of this synchronization on the frequencies of the mechanical oscillators, we observed that synchronization does not attain maximum values for identical oscillators. It rather peaks around a finite detuning between their frequencies. We also found that the two oscillators undergo synchronization transitions between in-phase and anti-phase values at different detunings. Our work throws light on the behaviour of quantum phase synchronization for variation in coupling paradigms and mechanical detunings, and highlights the ability to perform controlled switching between quantum phase-locked conditions of coupled oscillators. Also, the reduction of phase-noise with high degrees of synchronization can act as a great resource for time-keeping applications and can be utilized in quantum communication and for devising multi-oscillator quantum networks.

TH-3401_186121105

TH-3401_186121105

CHAPTER

3

# Optomechanically Induced Transparency

Cavity optomechanical systems and their hybrid analogues have long been used to probe the quantum-classical boundary. Much like their utility in the study of classical nonlinear phenomena in the micrometer scale, these systems also serve as a highly demanded platform to understand quantum phenomena in the macroscopic domain. Specifically, coherent interactions between the mechanical elements and the intracavity optical fields inside these systems have been extensively utilized to control and measure several classical and quantum properties in the past decade. Whereas majority of such systems rely on the transfer of linear momentum from the optical field to the mechanics via radiation-pressure interaction, atypical setups that involve more composite forms of interaction have also been designed to achieve remarkable results both in the classical and the quantum regime!

---

This chapter is based on our work published in Phys. Rev. A **107**, 013525 (2023), titled *Pump-probe Cavity Optomechanics with a Rotating Atomic Superfluid in a Ring* and authored by Sampreet Kalita, Pardeep Kumar, Rina Kanamoto, Mishkatul Bhattacharya and Amarendra K. Sarma [92, 93] (©2023 The Author(s) under the Creative Commons Attribution 4.0 International license).



TH-3401_186121105

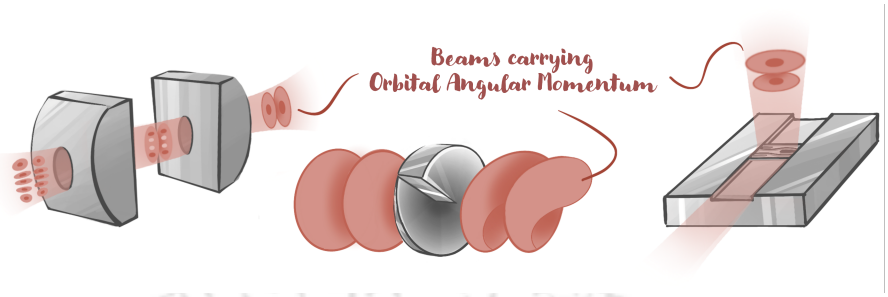


**Figure 3.1:** Common setups to generate beams with orbital angular momentum (*left to right*): cylindrical lenses, spiral phase plates and holographic gratings.

RECALL

*Photons can also carry orbital and spin angular momentum, analogous to the classical phase and circular polarization.*

One way to interlace photons and phonons without using conventional vibrational optomechanics is via the exchange of orbital angular momentum (OAM) [94]. Coherent optical beams carrying OAM can be generated using special setups that encode a spatially varying phase into an otherwise linear beam (refer to Figure 3.1). These OAM-carrying beams can then exert torque on mechanical elements, altering their rotational state and thereby affecting their mass distribution. Such effects have been experimentally demonstrated in nanoparticles [95,96], and even in in macroscopic states of matter such as liquid crystals [97] and Bose-Einstein condensates (BECs) [98–100]!

In addition to the transfer of angular momentum, OAM-carrying beams also carry vortices (singularities) in their axial profile. In fact, superposed OAM-carrying beams such as Laguerre-Gaussian modes are routinely used to confine BECs inside circular vortices [101] (refer to Figure 3.2). Such annularly-trapped BECs have emerged as a remarkable system for studying a plethora of phenomena associated with quantized circulation [102–108]. Along with supporting quantized vortices for macroscopically long times [99, 109, 110], these systems topologically stabilize states of higher circulation [111], thus providing a versatile platform for investigations of superfluid hydrodynamics [112, 113], matter-wave interferometry [114], atomtronic circuits [115,116], and fermionic superfluidity [117–119]. However, for the studies mentioned above, it is very important to characterize the circulation of the ring condensate. The determination of the rotation of atomic superfluid typically requires the measurement of the winding number of a rotational state.

TH-3401_186121105

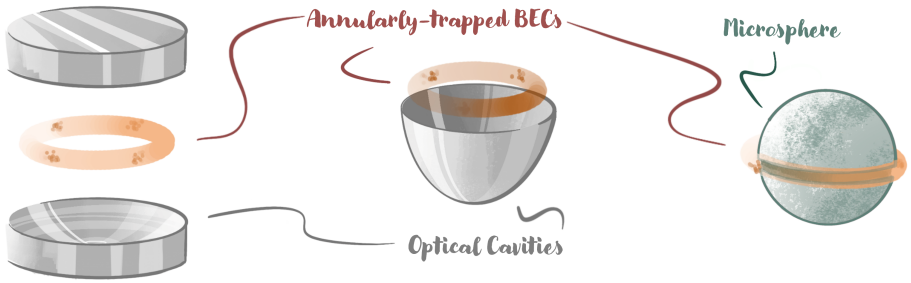


**Figure 3.2:** Geometries of annularly-trapped Bose-Einstein condensates (*left to right*): Fabry-Perot cavities, hemispherical cavities and microsphere waveguides.

The existing techniques for detecting the winding number involve atomic absorption of the photons used for imaging, and are thus fully destructive, thus precluding real-time observation and placing requirements on the replication of initial conditions [102]. Also the radius of the vortex (in this case, the ring trap) is typically smaller than the optical wavelength, thereby making it difficult to perform *in situ* detection of vortices in the trapped dilute gases, and requiring time-of-flight expansion techniques [104].

To circumvent the above issues, very recently, a versatile system [120] was proposed to sense and manipulate the rotation of annular BEC with minimal destruction, *in situ* and in real-time. The method improves the rotation sensitivity of ring BECs by three orders of magnitude compared to demonstrated methods and also provides a unique way to manipulate atomic currrents by generating optomechanical entanglement between atomic matter waves. In this chapter, we investigate another way to gauge the atomic rotation and study its quantum coherent effects using a similar optomechanical approach. Specifically, within the paradigm of rotational optomechanics [94], we examine the modification, by a rotating atomic superfluid, of the destructive interference between a strong pump field and a weak probe field driving the cavity containing the superfluid. In Section 3.1, we discuss the formalism of the system from an optomechanical perspective and derive a general expression for the transmission amplitudes of the optical field in-phase and out-of-phase with the probe frequency. We then analyze the optomechanically induced transparency (OMIT) and the group delay of the probe field. Finally, we conclude by summarizing our findings and mentioning the advantages of our method in Section 3.2.

TH-3401_186121105

## 3.1 Pump-probe Cavity Optomechanics with an Annularly Trapped Bose-Einstein Condensate

We consider an atomic BEC (sodium, Na) of $N$ atoms confined in a ring trap of radius $R$ placed inside an optical cavity as shown in Figure 3.3, and rotating with a winding number $L_p$. For such a configuration, the potential experienced by each atom in the condensate is such that the motion decouples along radial ($\rho$), axial ($z$), and azimuthal ($\phi$) directions. We employ a one-dimensional description of the problem, i.e., we consider the dynamics only along the azimuthal direction by assuming that the quantum state along radial and axial directions remains unchanged throughout the dynamic evolution of the system. Such a one-dimensional description can be applied if [121], $N < 4\sqrt{\pi}R\sqrt{\omega_\rho}/(3d_{\rm Na}\sqrt{\omega_z})$. Here, $d_{\rm Na}$ and $\omega_\rho$ ($\omega_z$) are the ground state scattering length of the Na atoms, and the radial (axial) harmonic trapping frequency respectively.

A superposition of two control lasers carrying OAM $\pm l\hbar$ interacts with the condensate. The generation of such a coaxial OAM superposition has already been achieved experimentally [122–124]. The corresponding optical beams generate an angular lattice inside the cavity and causes Bragg-scattering of some atoms in the condensate. For a weak dipole potential [120], only the first-order diffraction needs to be considered (see inset of Figure 3.3), namely, scattering from the rotational state with winding number $L_p$ to states with winding number $L_p \pm 2l$. We now introduce a weak laser drive of frequency $\omega_p$ and power $P_p$ to probe the ring BEC-cavity system.

Using the above arguments and the fact that the dynamics of the macroscopically occupied state with winding number $L_p$ is essentially classical, we write the Hamiltonian as [120] (refer to Appendix B for a brief derivation)

$$\frac{H}{\hbar} = -\tilde{\Delta}a^\dagger a + \sum_{j=c,d}\frac{\omega_j}{2}\left(X_j^2+Y_j^2\right) + G\left(X_c+X_d\right)a^\dagger a + \sum_{j=c,d}2\tilde{g}N\left(X_j^2+Y_j^2\right) + 2\tilde{g}N\left(X_cX_d - Y_cY_d\right) + iA_l\left(a^\dagger - a\right) + iA_p\left(a^\dagger e^{-i\delta t} - ae^{i\delta t}\right). \tag{3.1}$$

Here, the first term denotes the energy of the optical mode with $\tilde{\Delta} = \omega_l - \omega_o - g_a^2N/(2\Delta_a)$, where $\omega_o$, $g_a$, and $\Delta_a$ are the cavity frequency, the single atom-photon interaction strength and the detuning of the laser frequency from the atomic transition respectively. The second term denotes

TH-3401_186121105

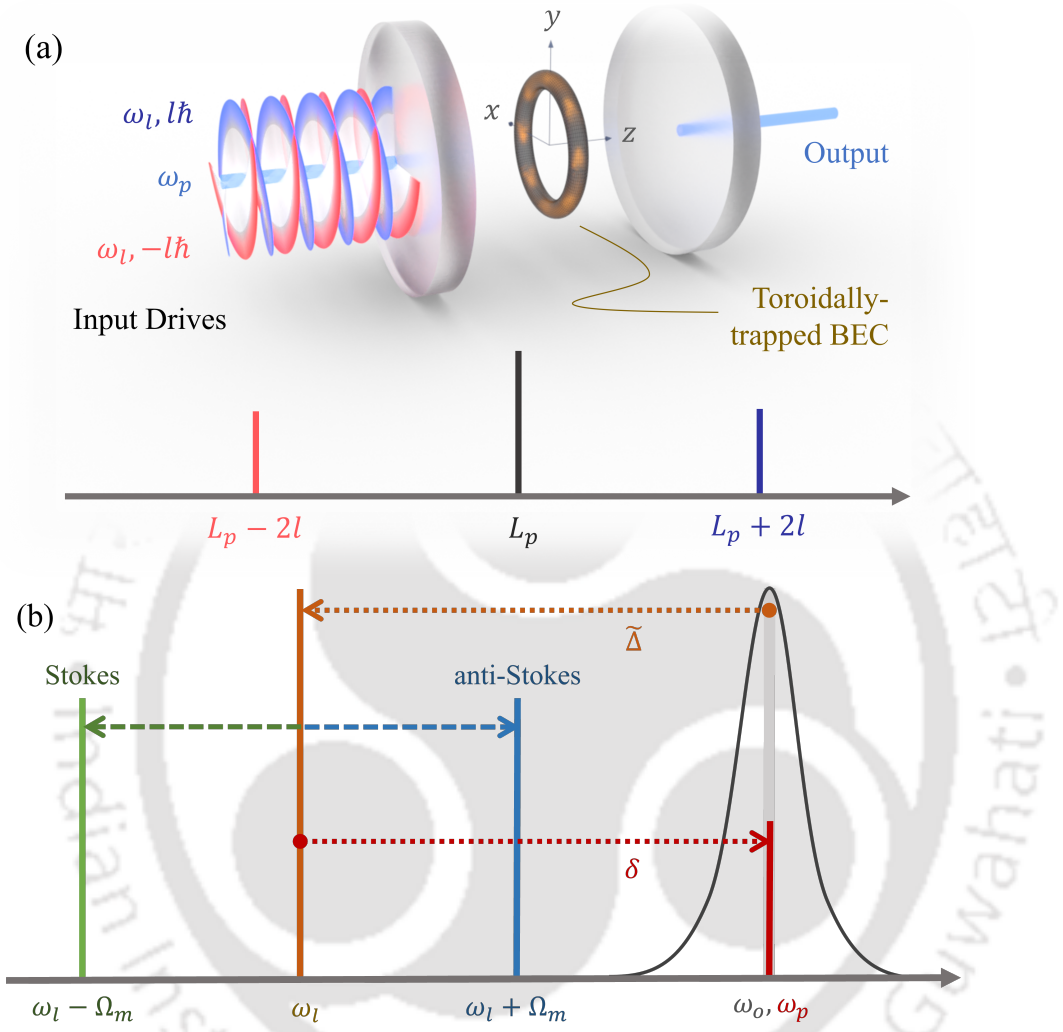


**Figure 3.3:** (a) A Fabry-Perot cavity with partially reflecting mirrors is driven by coherent control beams (red and blue helices on the left) carrying OAM, which interact with a toroidally-trapped BEC. A second weak laser (light blue beam) probes the cavity and its transmission is measured at the output. *Inset:* Position of the Bragg-scattered sidemodes on either sides of the initial winding number. (b) Position of the frequencies and the first mechanical sidebands of the control laser.

the energies of the sidemodes in terms of their dimensionless position and momentum operators. (Unless specified otherwise, we shall use $j \in \{c, d\}$ for the bosonic atomic operators obeying $[j, j'^{\dagger}] = \delta_{jj'}$ for the rest of the text.)

TH-3401_186121105

Here, the sidemode frequencies which are quadratic in angular momenta can be expressed as [120] $\omega_c = \hbar(L_p+2l)^2/(2I)$ and $\omega_d = \hbar(L_p-2l)^2/(2I)$, where $I = mR^2$ is the atomic moment of inertia about the center of the ring trap, $m$ being the mass of each Sodium atom. It may be noted here that the actual sidemode frequencies obtained from the Bogoliubov mode analysis are given by $\omega'_{c,d} = (\omega^2_{c,d} + 4\omega_{c,d}\tilde{g}N)^{1/2}$. However, here we use $\omega'_{c,d} \sim \omega_{c,d}$ by imposing $\omega_{c,d} \gg 4\tilde{g}N$, where $\tilde{g} = g/(4\pi\hbar)$ corresponds to the scaled two-body atomic interactions, with $g = 2\hbar\omega_\rho a_{Na}/R$ [120]. Further, the third term on the right hand side of Equation (3.1) denotes the optomechanical coupling between the sidemodes and the optical field where the effective sidemode coupling strength is given by $G = g_a^2\sqrt{N}/(2\sqrt{2}\Delta_a)$. The next two terms describe the inter-mode coupling owing to atom-atom interactions of strength $\tilde{g}$. The final two terms denote the control laser field and the probe laser field entering the cavity respectively, having amplitude $A_k = \sqrt{\mu\kappa P_k/\hbar\omega_k}$, with $k = l$ $(p)$ for the control (probe) laser and $\mu$ as the laser-cavity coupling parameter. The detuning of the probe laser from the control laser is $\delta = \omega_p - \omega_c$.

In the presence of the probe field, the corresponding Heisenberg Langevin equations for the system become

$$\begin{aligned}
\dot{a} &= -\left[\frac{\kappa}{2} - i\left\{\tilde{\Delta} - G\left(X_c + X_d\right)\right\}\right] a \\
&\quad + A_l + A_p e^{-i\delta t} + \sqrt{\mu\kappa}a_{in}, && \text{(3.2a)} \\
\ddot{X}_c &= -\gamma\dot{X}_c - \Omega_c^2 X_c - G\tilde{\omega}_c a^\dagger a - \mathcal{A}X_d + \omega_c\epsilon_c, && \text{(3.2b)} \\
\ddot{X}_d &= -\gamma\dot{X}_d - \Omega_d^2 X_d - G\tilde{\omega}_d a^\dagger a + \mathcal{A}X_c + \omega_d\epsilon_d. && \text{(3.2c)}
\end{aligned}$$

Here, $\gamma$ corresponds to the decay of supercurrents [125] and $\epsilon_j$ denote the Brownian noises in the mechanical sidemodes [9]. Also, for the sake of simplicity, we have introduced the quantities $\Omega_j^2 = (\omega_j + 4\tilde{g}N)^2 - 4\tilde{g}^2N^2$ and $\tilde{\omega}_j = \omega_j + 2\tilde{g}N$, $\mathcal{A} = 2\tilde{g}N(\omega_c - \omega_d)$.

With the above formalism, we study the output spectra of the Stokes field, which is *in phase* with the probe frequency to determine its transparency and amplification windows. We begin by assuming that the probe field is *sufficiently weak* in comparison to the control field ($A_l \gg A_p$) so that its effect can be treated as a perturbation to the otherwise classical steady-state. This, together with a sufficiently strong control field, allows us to present a linearized description of the system [12,126]. Proceeding in a similar way as Section 1.2.2, the classical expectation values are approximated as $\langle a\rangle = \alpha_s + A_- e^{-i\delta t} + A_+ e^{i\delta t}$, $\langle X_c\rangle = q_{cs} + C_- e^{-i\delta t} + C_+ e^{i\delta t}$ and $\langle X_d\rangle =$

TH-3401_186121105

$q_{ds} + D_- e^{-i\delta t} + D_+ e^{i\delta t}$, where $\alpha_s$, $q_{cs}$ and $q_{ds}$ are the steady-state classical mode amplitudes in the *adiabatic limit* ($\kappa \gg \gamma, g_a^2/\Delta_a$) given by

$$\alpha_s = A_l/\left(\kappa/2 - i\Delta\right), \tag{3.3a}$$

$$q_{cs} = -G\tilde{\omega}_d|\alpha_s|^2/\sqrt{\mathcal{A}^2 + \Omega_c^2\Omega_d^2}, \tag{3.3b}$$

$$q_{ds} = -G\tilde{\omega}_c|\alpha_s|^2/\sqrt{\mathcal{A}^2 + \Omega_c^2\Omega_d^2}, \tag{3.3c}$$

with effective detuning $\Delta = \tilde{\Delta} - G(q_{cs} + q_{ds})$. Solving this gives us

$$A_- = \frac{A_p\left(\Gamma_+ + iG^2\Lambda\left|\alpha_s\right|^2\right)}{\Gamma_+\Gamma_- + 2\Delta G^2\Lambda\left|\alpha_s\right|^2}, \tag{3.4a}$$

$$A_+^* = \frac{-iG^2A_p\Lambda\left(\alpha_s\right)^2}{\Gamma_+\Gamma_- + 2\Delta G^2\Lambda\left|\alpha_s\right|^2}, \tag{3.4b}$$

where $\Gamma_\pm = (\kappa/2 \pm i\Delta - i\delta)$, $\chi_j = 1/(\Omega_j^2 - i\delta\gamma - \delta^2)$ and $\Lambda = \{\mathcal{A}\chi_c\chi_d(\tilde{\omega}_c - \tilde{\omega}_d) + \chi_c\tilde{\omega}_c + \chi_d\tilde{\omega}_d\}/(\mathcal{A}^2\chi_c\chi_d + 1)$. Now, using the input-output convention for the system in Figure 3.3 as $a_{out} = -a_{in} + \sqrt{\mu\kappa}a$, the expectation value of the cavity output field can be expressed as

$$\langle a_{out}\rangle = s_l e^{-i\omega_l t} + s_S e^{-i(\delta+\omega_l)t} + s_{aS}e^{-i(\delta-\omega_l)t} \tag{3.5}$$

Here, $s_l = \sqrt{\mu\kappa}\alpha_s - A_l/\sqrt{\mu\kappa}$ is the signal at the control laser frequency $\omega_l$, and $s_S = \sqrt{\mu\kappa}A_- - A_p/\sqrt{\mu\kappa}$ is the Stokes sideband signal oscillating at the frequency of the probe field $\delta + \omega_l = \omega_p$. On the other hand, the anti-Stokes signal $s_{aS} = \sqrt{\mu\kappa}A_+$, which oscillates at $\omega_l - \delta = 2\omega_l - \omega_p$, results in the four-wave mixing effect, due to the interaction of the upconverted control field and the reflected probe field. Above Stokes and anti-Stokes sidebands can also be visualized as the mechanical sidebands which arise due to the scattering of the strong control field. This can be viewed from Figure 3.3(b), when the resonance condition $\delta = \Omega_m$ is achieved. Thus, the transmission intensity at the probe frequency is obtained as [17, 127]

$$T = |t_S|^2 = \left|1 - \frac{\mu\kappa A_-}{A_p}\right|^2 = \left|1 - \frac{\mu\kappa\left(\Gamma_+ + iG^2\Lambda\left|\alpha_s\right|^2\right)}{\Gamma_+\Gamma_- + 2\Delta G^2\Lambda\left|\alpha_s\right|^2}\right|. \tag{3.6}$$

Here the real and imaginary parts of the amplitude $t_S$ reflect the absorption and dispersion properties of the system in response to the probe field.

TH-3401_186121105

To investigate the effect of control field-mediated interference on the output probe field, we choose experimentally feasible parameters [102, 120–122, 128–130]: $m = 23$ amu, $R = 10$ $\mu$m , $N = 10^4$, $\lambda_l = 589$ nm, $L_p = 1$ (unless stated otherwise), $l = 20$ (unless indicated otherwise), $g_a/(2\pi) = 0.36$ MHz, $\Delta_a/(2\pi) = 4.7$ GHz, depth of the optical potential $U_0/(2\pi) = 28.3$ Hz, $G/(2\pi) = 1$ kHz, $\gamma/(2\pi) = 0.8$ Hz, $\kappa/(2\pi) = 1$ kHz, $\mu = 0.5$, $d_{\mathrm{Na}} = 0.1$ nm, the atomic interaction in the mean-field regime $\tilde{g}_m = \frac{\hbar}{4IN}\ \tilde{g}_m/(2\pi) \sim 0.11$ mHz, $\tilde{g} \sim 12\tilde{g}_m$, and $\omega_z/(2\pi) = \omega_\rho/(2\pi) = 840$ Hz. For the above parameters, our system is minimally destructive, namely, very few atoms get diffracted from the ring trap to first-order Bragg-diffraction sidemodes. Also, as stated earlier, we have verified that these set of parameters satisfy (i) a one-dimensional description of our model, (ii) $\omega_{c,d} \gg 4\tilde{g}N$, and (iii) the inequality required for weak potential [120]. In what follows, we numerically simulate the probe transmission spectrum.

APPROX.

*The strength of the atom-atom coupling has a negligible effect on the probe transmission and we therefore set $\tilde{g} = 0$ for the rest of our analysis [120].*

DIGRESSION 3.1

**Stability and Choice of Control Power**

To proceed further, we first choose the parameters for which the system remains monostable [120, 130] and also satisfies the Routh-Hurwitz criteria. Also, we set the control field detuning equal to the mean of the sidemode frequencies, i.e., $\tilde{\Delta} = -\Omega_m = -(\Omega_c + \Omega_d)/2$. This choice of the cavity detuning allows us to elicit the signatures of both single (non-rotating BEC) as well as double-OMIT (rotating BEC) resonances from our system, as explained below. We observe that the system displays bistability for a few femtoWatts of input power for a red-detuned control field. Also, for control powers $P_l \ll 6$ fW, and $0 \leq L_p \leq 10$, the system is dynamically stable. The characteristic analytical expression for the critical control power at $\tilde{\Delta} = -\Omega_m$ is given by

$$P_{l_{cr}} = \frac{\hbar\omega_l\Omega_m}{54\mu\kappa C}\left(4\Omega_m^2 + 9\kappa^2\right)$$

where $C = G^2(\tilde{\omega}_c + \tilde{\omega}_d)/(\mathcal{A}^2 + \Omega_c^2\Omega_d^2)^{1/2}$. For the remainder of our analysis, we choose parameters (for instance $P_l \ll P_{l_{cr}}$ and $P_l \ll 6$ fW) to keep our system away from bistability and also in the dynamically stable regime.

TH-3401_186121105

### 3.1.1 Induced Transparency

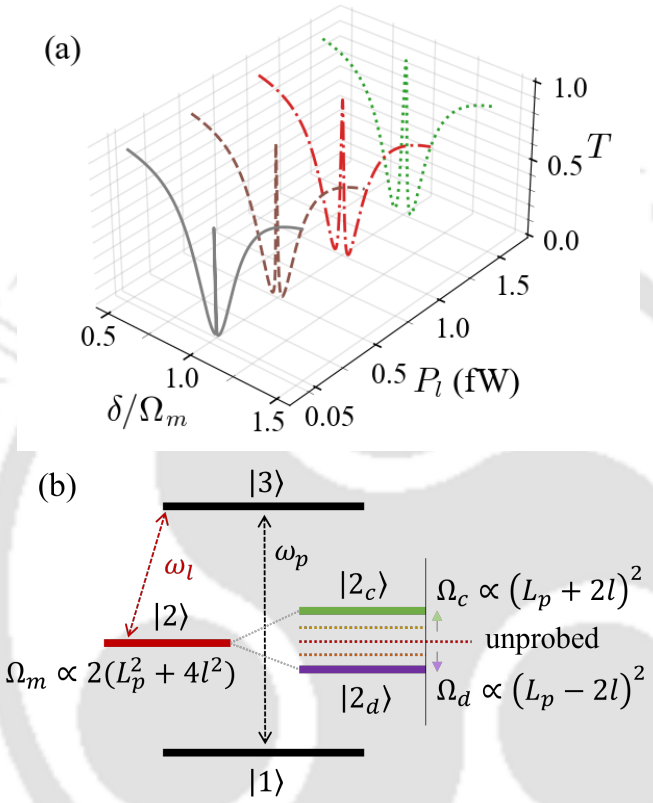


**Figure 3.4:** (a) Transmission spectrum of the probe field ($T$) for $L_p = 0$ obtained at $\tilde{\Delta} = -\Omega_m$ at different values of control power ($P_l$). Here, $P_{l_{cr}} = 28$ fW. (b) Energy levels and transition pathways for the system at $\tilde{\Delta} = -\Omega_m$.

In the absence of atomic rotation ($L_p = 0$), the two mechanical sidemodes are degenerate. In the presence of the control beam, the probe transmission spectrum obtained from Equation (3.6) shows signatures of OMIT [127,131], as shown in Figure 3.4(a). This is because the simultaneous presence of the control and probe fields causes the radiation pressure force to oscillate at a beat frequency $\delta = \omega_p - \omega_l$. If these oscillations are in resonance with $\Omega_m$, then the mechanical sidemode also starts vibrating coherently. This further gives rise to the Stokes ($\omega_l - \Omega_m$) and anti-Stokes ($\omega_l + \Omega_m$) scattered light from the strong control field (refer to Figure 3.4(b)). At $\tilde{\Delta} = -\Omega_m$, the Stokes scattering becomes highly off-resonant and thereby gets suppressed.

TH-3401_186121105

As a result, only anti-Stokes light ($|1\rangle \rightarrow |3\rangle \rightarrow |2\rangle \rightarrow |3\rangle$) builds up in the cavity which is degenerate with the probe field ($|1\rangle \rightarrow |3\rangle$). The destructive interference between the probe and the anti-Stokes scattering hinders the formation of the intracavity probe field and produces transparency [31, 132].

The physical origin of the OMIT can also be understood from the $\Lambda$-type energy level structure for $L_p = 0$ shown in the left half of Figure 3.4(b). In this configuration, the probe field excites a direct transition $|1\rangle \leftrightarrow |3\rangle$ in which the occupation of the mechanical oscillator remains unchanged. However, the control laser is scanned close to the red sideband on an indirect transition ($|2\rangle \leftrightarrow |3\rangle$). In this transition, a mechanical excitation quantum is annihilated and a photon is created inside the cavity. Since the control laser is much stronger than the probe, the magnitude of excitation amplitude of the indirect transition is of the same order as the direct transition. Under resonant conditions ($\delta = \Omega_m$, and $\tilde{\Delta} = -\Omega_m$), the excitation amplitude of the indirect pathway is $\pi$ out of phase ($|2\rangle \rightarrow |3\rangle$ and $|\,|3\rangle \rightarrow |2\rangle$ each contribute $\pi/2$ phase shift) with respect to the direct excitation pathway. In other words, the two excitation pathways, $|1\rangle \rightarrow |3\rangle$ and $|1\rangle \rightarrow |3\rangle \rightarrow |2\rangle \rightarrow |3\rangle$, interfere destructively to create transparency for the probe field [133].

DIGRESSION 3.2

**Approximate Expressions for Peak Value and Peak Width**

The interference effects discussed above are classical in nature and are studied in the linearized regime where quantum nonlinear effects are neglected [134–136]. In this regime, the OMIT response is determined by a combined parameter $G|\alpha_s|$ and is typically observed for $\gamma \ll \Gamma_{\rm om}$ (with $\Gamma_{\rm om} = 4G^2|\alpha_s|^2/\kappa$), and $G|\alpha_s| \ll \kappa \ll \Omega_m$. The expressions for the peak value and width of the OMIT window can therefore be approximated as [17]

$$\begin{aligned} T(\delta = \Omega_m) &\approx \left(\frac{\mathcal{C}}{1+\mathcal{C}}\right)^2 \\ \Gamma_m &\approx \gamma\,(1+\mathcal{C}) \end{aligned}$$

where $\mathcal{C} = \Gamma_{om}/\gamma$ is the cooperativity of the system. Both these analytical expressions fit well with the exact numerical values at different powers. Moreover, since the degree of interference can be controlled by the power of the control laser, the features of the OMIT, such as the height and width of its window, can also be manipulated by varying the control laser's power.

TH-3401_186121105

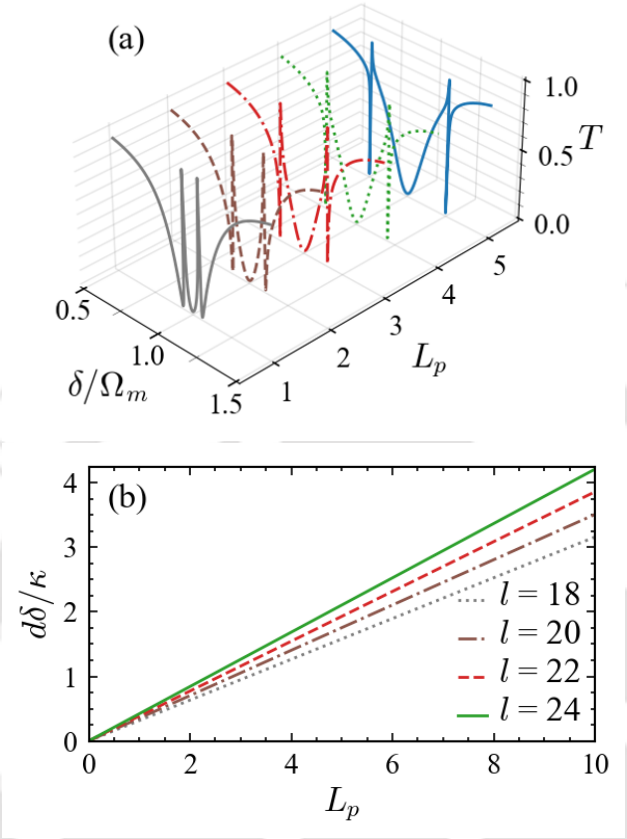


**Figure 3.5:** (a) Transmission of the probe field ($T$) as a function of the winding number ($L_p$) for $P_l = 1$ fW. For this case, the critical power is $P_{l_{cr}} = 33$ fW. (b) Separation between the transparency peaks ($d\delta$, normalized by $\kappa$) as a function of the winding numbers ($L_p$) at control laser detuning $\tilde{\Delta} = -\Omega_m$ and for different values of OAM. Other parameters used are same as those in Figure 3.4.

For an initially non-rotating BEC ($L_p = 0$), the Bragg-scattered mechanical modes become degenerate and the probe transmission spectrum exhibits OMIT in the presence of a control laser. However, in the presence of a persistent flow in ring BEC ($L_p \neq 0$), the mechanical sidemodes no longer remain degenerate and acquire distinguishable frequencies. This in turn modifies the output probe transmission spectrum, as shown in Figure 3.5(a). Specifically, the spectrum shows double-OMIT, i.e., two transparency windows emerge along with the absorption window of width $\sim |\Omega_c - \Omega_d|$ situated at $\delta = \Omega_m$ [132, 137, 138]. Further, it can be seen that the two transmission peaks are situated at $\delta_+ = \Omega_d$ and $\delta_- = -\Omega_c$, respectively.

TH-3401_186121105

The underlying mechanism for the double-OMIT structure can be explained from the interference between three transition pathways formed for $L_p \neq 0$ (refer to the right half of Figure 3.4(b)). Similar to the case of $L_p = 0$, here, the destructive interference due to $\pi$ phase shift between the excitation pathways — (i) $|1\rangle \rightarrow |3\rangle$ and $|1\rangle \rightarrow |3\rangle \rightarrow |2_c\rangle \rightarrow |3\rangle$, or (ii) $|1\rangle \rightarrow |3\rangle$ and $|1\rangle \rightarrow |3\rangle \rightarrow |2_d\rangle \rightarrow |3\rangle$ — suppresses the buildup of the intracavity field at the respective beat frequencies. Thus, whenever the two sidemodes frequencies (at energy levels $|2_c\rangle$ and $|2_d\rangle$) are resonant with the beat frequency $\delta$, a transparency window is observed, resulting in a double-OMIT structure [137]. However, a complete absorption at $\delta = \Omega_m$ results from the constructive interference between one direct pathway ($|1\rangle \rightarrow |3\rangle$) and two indirect excitation pathways ($|1\rangle \rightarrow |3\rangle \rightarrow |2_c\rangle \rightarrow |3\rangle$ and $|1\rangle \rightarrow |3\rangle \rightarrow |2_d\rangle \rightarrow |3\rangle$). This is because the indirect pathways give rise to a total of $2\pi$ phase shift with respect to the direct transition pathway.

Interestingly, an increase in the magnitude of the winding number of the persistent flow results in a higher frequency separation between the Bragg scattered mechanical side-modes. This characteristic feature of the probe transmission may serve as a tool to sense the state of rotation of the BEC. For instance, the separation of the transmission peaks from resonance increases with the BEC winding number. This dependence can be used to detect the magnitude of the winding number of the persistent flow present in the atomic superfluid. To obtain more insight, we study the separation between the transmission peaks such that $d\delta = \delta_+ - \delta_-$ as shown in Figure 3.5(b). Salient features of this plot are: (i) the peak-separation varies linearly with the winding number, $L_p$. This is due to the fact that the transmission dips appear at frequencies, $\omega_p = \omega_l + \Omega_c$ and $\omega_p = \omega_l + \Omega_d$, respectively. Thus, the difference between the transmission dips varies as the beat frequency of the two mechanical sidemodes which is linearly proportional to the winding number. (ii) The difference in the peak separation remains immune to the sign of the winding number. A change of sign of $L_p$ is analogous to the swapping of the sidemode frequencies about their mean, resulting in equal and opposite values of frequencies, thereby producing equal transmissions.

NOTE

*When the laser detuning and the pump-probe detuning are not resonant with the mechanical frequency, asymmetric Fano profiles are observed [139, 140].*

TH-3401_186121105

### 3.1.2 Group Delay

In the preceding section, we exploited the control beam-generated destructive interference to obtain narrow transmission windows in the probe output spectrum. Another remarkable effect in this system is the dispersion, which allows the use of a transparency window for the exploration of slow- or fast-light. Specifically, it is the rapid variation of the transmission phase of the probe field within the transparency window which governs the dispersion. Using Equation (3.6), one can obtain such a dispersion profile from the argument of the transmission amplitude and calculate the transmission group delay from its slope, such that [141]

$$\phi(\omega_p) = \arg[t_S(\omega_p)], \tag{3.7a}$$

$$\tau_g = \frac{d\phi(\omega_p)}{d\omega_p}. \tag{3.7b}$$

Figure 3.6 displays the transmission phase and group delay as a function of pump-probe detuning in the absence and presence of quantized circulation. Around resonance, $\delta = \Omega_m$, the transmission phase of the probe field shows a rapid positive (negative) variation for $L_p = 0$ ($L_p = 1$), as shown in Figure 3.6(a). It suggests that within the transparency window, switching from positive group delay (slow light) to negative group delay (fast light) takes place once the BEC starts rotating, as exhibited in Figure 3.6(b).

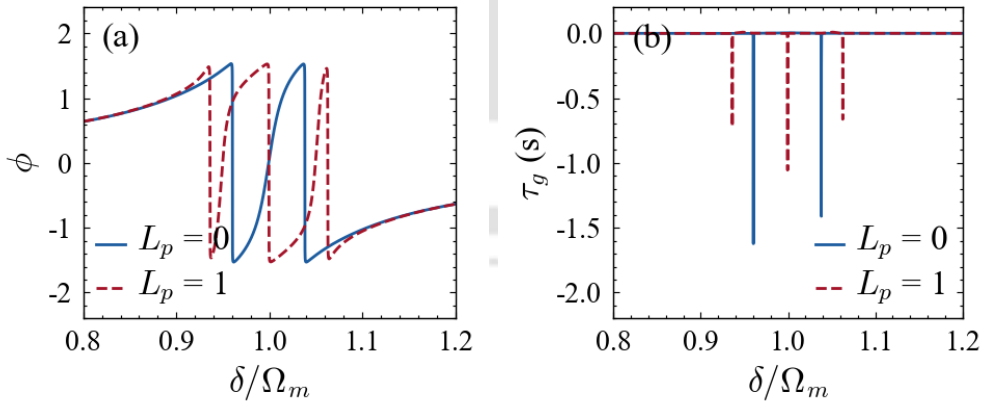


**Figure 3.6:** (a) Transmission phase ($\phi$) and (b) group delay ($\tau$) as a function of normalized pump-probe detuning ($\delta/\Omega_m$) for $L_p = 0$ (dashed blue) and $L_p = 1$ (solid red). Other parameters used are same as those in Figure 3.4.

TH-3401_186121105

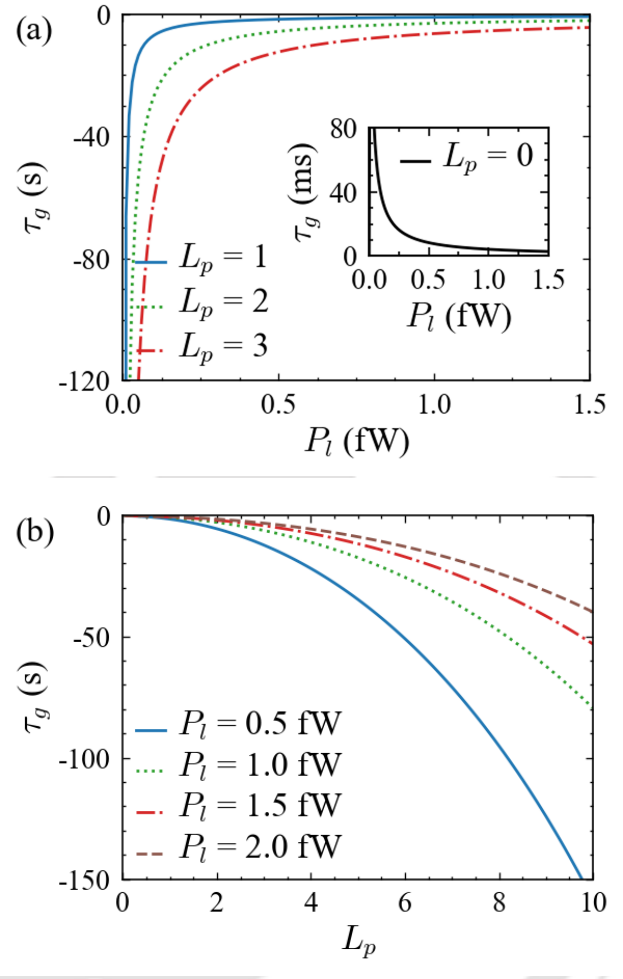


**Figure 3.7:** Group delay ($\tau$) as a function of (a) control power ($P_l$) for different winding numbers ($L_p$) and (b) winding number ($L_p$) for different control powers ($P_l$). Here, $\delta = \Omega_m$. Other parameters used are same as those in Figure 3.4.

As per Equation (3.7b), the variation of the transmission phase at resonance plays an important role in determining the group delay. In Figure 3.7(a), we exhibit the group delay at $\delta = \Omega_m$, as a function of the power of the control beam for different winding numbers. For $L_p = 0$, the group delay decreases with control power, as shown in the inset of Figure 3.7(a). This is because, for lower power the transmission window is very narrow and therefore, the corresponding dispersion profile has a very sharp slope around

TH-3401_186121105

resonance which corresponds to high group index and slow light. However, with an increase in power, the transmission window broadens and eventually the slope of the dispersion decreases. In the presence of atomic circulation, the group delay becomes negative corresponding to fast light. And with the increase in control power the negativeness of the group delay diminishes for the same reason as explained above. Since the absorption window around resonance broadens for an increase in the winding number, the negativity of the slope of the dispersion profile decreases, the group delay takes larger negative values as shown in Figure 3.7(b).

## 3.2 Summary of the Chapter

Here, we introduced an annularly trapped Bose-Einstein condensate inside a cavity and systematically investigated how coherent interference effects can be manipulated by atomic persistent currents in the presence of strong control fields and a weak probe beam. First of all, we analyzed the transmission spectrum of the probe field. Under resonant conditions, we observed that destructive interference results in the emergence of symmetric narrow transmission windows in the probe spectrum, exhibiting optomechanically induced transparency. However, in the presence of atomic superflow, the probe transmission spectrum is modified and a double-peaked structure appears with an absorption window at the resonance. Moreover, we found that the characteristic features of the output probe spectrum can be manipulated by tuning the quantized circulation. For instance, the separation between the peaks in the probe transmission provides as a useful tool for establishing the magnitude of the quantized circulation. In addition to studying the probe transmission, we also presented our findings on the group delay of the probe field. Remarkably, the system shows switching from slow to fast light as the atomic circulation is turned on. The observed phenomena can be employed to realize quantum state transfer protocols [142, 143], measurement of OAM of light [144], optical switching [145, 146] and wavelength conversion [147].

TH-3401_186121105

TH-3401_186121105

CHAPTER

4

# Modulated Optomechanics

Quantum phenomena such as entanglement and squeezing have been studied extensively in a wide range of theoretical models and realized experimentally in a multitude of platforms. Several applications, ranging from sensing minuscule forces and displacements to preparation of highly nonclassical states in quantum devices, have their roots in the generation of robust squeezing and significant entanglement between the constituent components. Here, we introduce the technique of modulations for the generation, enhancement and retention of these quantum properties in atypical optomechanical setups.

---

This chapter is based on two of our published works: (1) J. Opt. Soc. Am. B **40**, 1398 (2023), titled *Robust Mechanical Squeezing beyond 3 dB in a Quadratically Coupled Optomechanical System* and authored by Priyankar Banerjee, Sampreet Kalita and Amarendra K. Sarma [148, 149] (©2023 Optica Publishing Group) and (2) Phys. Rev. A **106**, 043501 (2022), titled *Significant Optoelectrical Entanglement and Mechanical Squeezing in a Multimodulated Optoelectromechanical System* and authored by Sampreet Kalita, Saumya Shah and Amarendra K. Sarma [150, 151] (©2022 American Physical Society). All reproduced content are added with permission.



TH-3401_186121105

For most sensing applications, the precision of measurements in micromechanical systems is bounded by their zero-point quantum fluctuations [12]. Moreover, these position measurements also introduce noises that mostly exceed the standard quantum limit (SQL) of 3 dB [152]. To circumvent this, the motional quadratures are typically squeezed beyond this SQL using suitable approaches [153–156]. In the past decades, mechanical squeezing has been proposed using squeezed photons [157, 158], two-tone driving [152,156,159,160], reservoir engineering [40,161–163] and frequency modulation [164]. Also, squeezed vacuum light is routinely used in gravitational wave detectors [165,166]. Such interferometric setups are also useful for information processing, where quantum entanglement serves as a crucial resource [167]. This phenomena has been theoretically studied in several optomechanical models [19, 53, 168–171], and experimentally realized in simple as well as hybrid setups [172–175]. Transduction of information through quantum phenomena has also been reported in hybrid "opto-electro-mechanical" systems [176–178]. Such devices rely on the fact that optomechanical systems are highly integrable into solid-state electronics through their mechanical components. The radiation-pressure-induced mechanical displacement in the optomechanical half [9,10] of such systems induces voltages and currents in the quantum electrical elements [179], thus enabling transfer of information between the optical and electrical components. These hybrid systems offer sufficient scalability together with the ability to leverage entanglement for efficient communication and storage schemes [44, 46, 180–183]. However, entanglement usually gets decohered with time due to the constant interactions of the system with the environment. Therefore, there is a continuous lookout for systems that can accommodate this properties not only for longer durations but also in substantial amounts.

One way to enhance quantum properties like squeezing and entanglement is by introducing higher-order nonlinearities, typically a squeezed-mode interaction Hamiltonian [12]. For example, in Section 1.1, we formalized the Hamiltonian of a simple optomechanical system considering only the linear term in the expansion of the cavity frequency (refer to Equation (1.1)). One can also consider the terms which are quadratic or higher in $q$ and study the effect of higher-order interactions in optomechanical systems. Of popular interest is the inclusion of the quadratic term, which results in the optomechanical interaction Hamiltonian $H_i \approx -\hbar g_0 a^\dagger a(b^\dagger + b) + \hbar g_1 a^\dagger a(b^\dagger + b)^2$, where the quadratic coupling is governed by the constant $g_1 = \hbar\omega_o/(4m\omega_m L^2)$. Compared to the linear term, the contribution of the quadratic term is usually

TH-3401_186121105

very small in typical moveable-end-mirror setups, and can often be ignored. But in certain systems such as those with a thin membrane at the node or antinode of a fixed-miror cavity, the second term can play a significant role [9]. Such "membrane-in-the-middle" setups have been used to analyze the effect of second-order interactions, in the generation of quantum phenomena [184] and also in sensing applications [185].

Another widely followed protocol to enhance the generated entanglement and squeezing is the introduction of modulations [20, 40, 186–189]. We shall discuss this method in this chapter. In Section 4.1, we briefly introduce the effects of laser modulations in the dynamical state of a simple optomechanical system and analyze the its contributions towards the enhancement of the mechanical squeezing and optomechanical entanglement. We then extend this analysis to a quadratically-coupled membrane-in-the-middle optomechanical system in Section 4.2. Here, we present the dissipative generation of mechanical squeezing by periodically modulating the driving amplitude and show that along with a robust squeezing, a high degree of optomechanical entanglement can be produced. We then introduce a hybrid opto-electromechanical system in Section 4.3. Here, we study the bipartite entanglement between the optical and the electrical components in the presence of multiple modulations — the laser drive amplitude, the voltage drive amplitude and the mechanical spring constant. Additionally, we analyze the squeezing in the mechanical position and comment on the windows of maximum mechanical squeezing and optoelectrical entanglement. Finally, we summarize the chapter and mention the applications of our works in Section 4.4.

## 4.1 Effect of Amplitude Modulations

In the presence of a laser drive whose amplitude is modulated as $A_l = \Sigma_{n=-\infty}^{\infty} A_{ln} e^{-in\Omega_l t}$ (where $A_{ln}$ are the strengths of the sideband modulations and $\Omega_l$ denotes the frequency of the modulation), the laser Hamiltonian introduced in Equation (1.4) can be re-written as

$$H_d = i\hbar \left( A_l a^\dagger e^{-i\omega_l t} - A_l^* a e^{i\omega_l t} \right) = i\hbar \sum_{n=-\infty}^{\infty} A_{ln} \left( a^\dagger e^{-i(\omega_l + n\Omega_l)t} - a e^{i(\omega_l + n\Omega_l)t} \right).$$

This results in a time-dependent laser amplitude term in the Heisenberg Langevin equation corresponding to the optical mode. A semi-classical treatment then incorporates this term in the classical mean amplitude of the

TH-3401_186121105

optical mode. Utilizing a power series ansatz for the asymptotic classical dynamics to obtain the mean amplitudes oscillating at the frequencies $n\Omega_l$, one finds that a suitable approximation of the dynamical behaviour can be given by just considering the first-order sidebands (refer to Reference [40]).

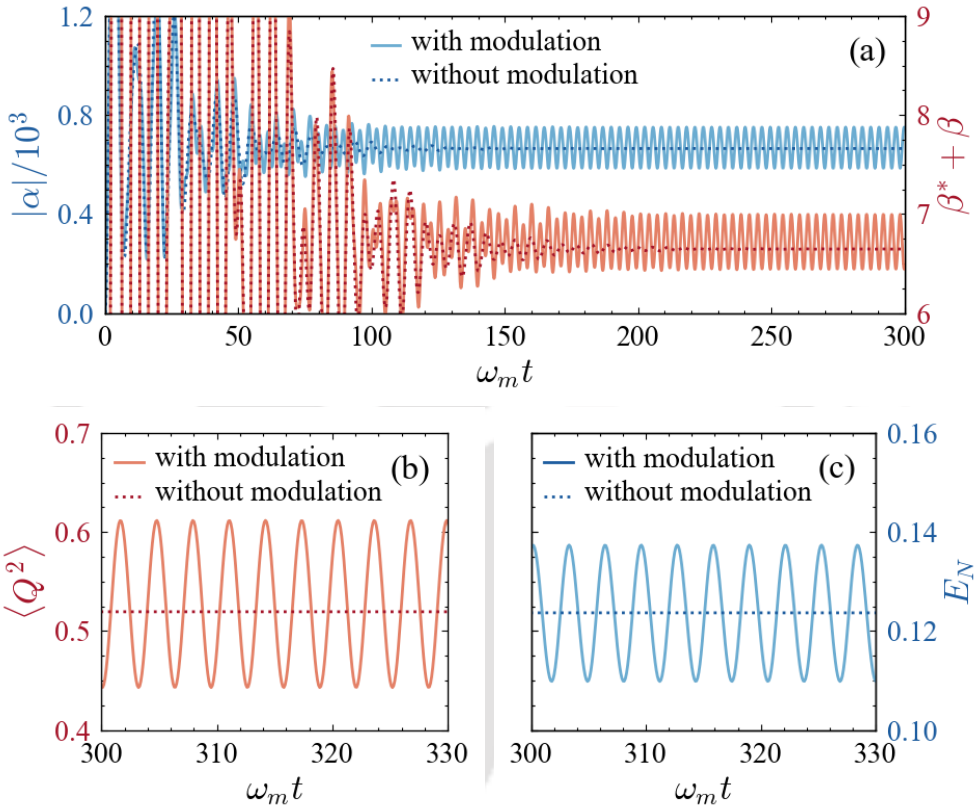


**Figure 4.1:** (a) Dynamics of the classical mode amplitudes $|\alpha|/10^3$ (blue) and $2\mathrm{Re}[\beta]$ (red) in the presence (solid) and absence (dotted) of modulations in the laser amplitude. (b) Corresponding dynamics of the correlations $\langle Q^2 \rangle$ (red) and optomechanical entanglement $E_N$ (blue). Here, we have used $A_{l0} = 25.0$ with $A_{l\pm} = 0.1A_{l0}$ and $\Omega_l = 2.0$. Other parameters are the same as Figure 1.5(a).

As can be seen in Figure 4.1(a), the modulations in the laser drive introduce oscillations in the classical mode amplitudes even in the red-detuned regime. Since these modes are integral parts of the effective detuning and the effective coupling, the drift matrix becomes time-dependent, and as a result, the quantum properties follow similar behaviour as shown in Figure 4.1(b-c). We now proceed to analyze these properties in two different systems.

TH-3401_186121105

## 4.2 Optomechanical Entanglement and Mechanical Squeezing in a Quadratically Coupled System

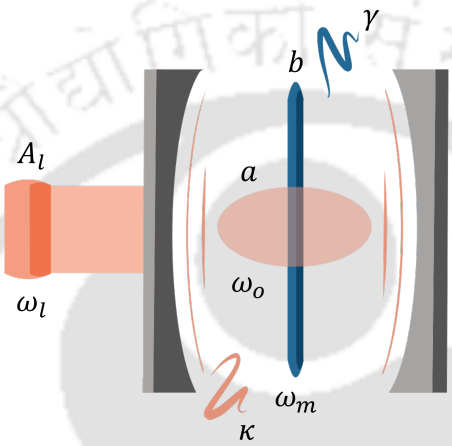


**Figure 4.2:** A laser-driven membrane-in-the-middle optomechanical system.

Figure 4.2 illustrates our membrane-in-the-middle setup inside an optical cavity driven by an amplitude-modulated laser drive. In the rotating frame of the laser frequency $\omega_l$, we write the Hamiltonian of this system as [9]

$$\begin{aligned} H &= -\hbar\Delta_0 a^\dagger a + \hbar\omega_m b^\dagger b + \hbar g_1 a^\dagger a \left(b^\dagger + b\right)^2 \\ &\quad + i\hbar\left(A_l a^\dagger - A_l^* a\right) + \hbar\eta\left(b^\dagger + b\right). \end{aligned} \tag{4.1}$$

Here, the third term denotes the optomechanical interaction energy with quadratic coupling coefficient $g_1$. The fourth term represents the amplitude-modulated laser drive and the final term represents a constant impulsive force of strength $\eta$ acting on the mechanical membrane, which prevents the mechanical motion of the oscillator from dying out in the long time limit.

For a sufficiently strong laser drive, the Heisenberg Langevin equations obtained from the Hamiltonian in Equation (4.1) can be approximated by a semi-classical description such that the classical dynamics are governed by

$$\dot{\alpha} = i\Delta_0\alpha - \frac{\kappa}{2}\alpha - ig_1\alpha\left(\beta^* + \beta\right)^2 + A_l, \tag{4.2a}$$

$$\dot{\beta} = -i\omega_m\beta - \frac{\gamma}{2}\beta - 2ig_1\left|\alpha\right|^2\left(\beta^* + \beta\right) - i\eta, \tag{4.2b}$$

TH-3401_186121105

and the dynamics of the quantum fluctuations are given by

$$\delta\dot{a} = i\Delta_1\delta a - \frac{\kappa}{2}\delta a - 2ig_1\alpha\left(\beta^* + \beta\right)\left(\delta b^\dagger + \delta b\right) + \sqrt{\kappa}a_{in}, \tag{4.3a}$$

$$\delta\dot{b} = -i\omega_m\delta b - \frac{\gamma}{2}\delta b - 2ig_1\left(\alpha^*\delta a + \alpha\delta a^\dagger\right)\left(\beta^* + \beta\right) - 2ig_1\left|\alpha\right|^2\left(\delta b^\dagger + \delta b\right) + \sqrt{\gamma}b_{in}, \tag{4.3b}$$

with $\Delta_1 = \Delta_0 - g_1(\beta^* + \beta)^2$ as the new effective detuning. The drift matrix for the quantum fluctuation quadratures can then be obtained as

$$\mathbf{A} = \begin{pmatrix} -\frac{\kappa}{2} & -\Delta_1 & 8g_1\alpha_I\beta_R & 0 \\ \Delta_1 & -\frac{\kappa}{2} & -8g_1\alpha_R\beta_R & 0 \\ 0 & 0 & -\frac{\gamma}{2} & \omega_m \\ -8g_1\alpha_R\beta_R & -8g_1\alpha_I\beta_R & -\omega_m - 4g_1\left|\alpha\right|^2 & -\frac{\gamma}{2} \end{pmatrix}, \tag{4.4}$$

where $\alpha_R$ ($\beta_R$) and $\alpha_I$ ($\beta_I$) are the real and imaginary components of $\alpha$ ($\beta$) respectively. The corresponding noise correlations terms are given by the matrix $\mathbf{D} = \text{Diag}[\kappa(n_a + 1/2), \kappa(n_a + 1/2), \gamma(n_b + 1/2), \gamma(n_b + 1/2)]$.

As discussed in Section 4.1, we now assume that the primary contribution of the modulated drive comes from the offset strength and the first-order modulations, and that the optical mode and the mechanical mode amplitudes display a periodic profile which is similar to that of the modulated external field [20, 188]. We, therefore, assume a classical ansatz for the amplitudes as

$$\alpha = \alpha_{-1}e^{i\Omega_l t} + \alpha_0 + \alpha_1 e^{-i\Omega_l t}, \tag{4.5a}$$

$$\beta = \beta_{-1}e^{i\Omega_l t} + \beta_0 + \beta_1 e^{-i\Omega_l t}. \tag{4.5b}$$

At this point, it is interesting to analyze the dynamics of the slowly varying fluctuations by moving into the rotating frame of their oscillations. To do this, we rewrite the fluctuation operators (input noises) for the optical and mechanical modes as $\delta a = \tilde{a}e^{i\Delta_1 t}$ ($a_{in} = \tilde{a}_{in}e^{i\Delta_1 t}$) and $\delta b = \tilde{b}e^{-i\omega_m t}$ ($b_{in} = \tilde{b}_{in}e^{-i\omega_m t}$) respectively. By tuning the classical dynamics of our system in such a way that $\Delta_1 \approx -\omega_m$ and $\Omega_l = 2\omega_m$, one can obtain

$$\dot{\tilde{a}} = -iG_0\tilde{b} - iG_1\tilde{b}^\dagger - \frac{\kappa}{2}\tilde{a} + \sqrt{\kappa}\tilde{a}_{in}, \tag{4.6a}$$

$$\dot{\tilde{b}} = -iG_0\tilde{a} - iG_1\tilde{a}^\dagger - i\tilde{G}_0\tilde{b} - i\tilde{G}_1\tilde{b}^\dagger - \frac{\gamma}{2}\tilde{b} + \sqrt{\gamma}\tilde{b}_{in}, \tag{4.6b}$$

TH-3401_186121105

where we have used the ansatz in Equations (4.5) to obtain

$$
\begin{aligned}
G_0 &= 2g_1\left\{2\alpha_0\beta_0 + (\alpha_{-1}+\alpha_1)(\beta_{-1}+\beta_1)\right\}, && \text{(4.7a)}\\
G_1 &= 2g_1\left\{\alpha_0(\beta_{-1}+\beta_1) + 2\alpha_1\beta_0\right\}, && \text{(4.7b)}\\
\tilde{G}_0 &= 2g_1\left(\alpha_0^2+\alpha_{-1}^2+\alpha_1^2\right), && \text{(4.7c)}\\
\tilde{G}_1 &= 2g_1\alpha_0(\alpha_{-1}+\alpha_1). && \text{(4.7d)}
\end{aligned}
$$

APPROX.

*In deriving Equations (4.6), we used the rotating wave approximation (RWA) to ignore the highly oscillating terms in $\omega_{mL}$.*

To verify the above approximation, let us numerically simulate Equations (4.6) and compare these results with those obtained using Equations (4.3). To do this, we first write the drift matrix under RWA as

$$
\tilde{\mathbf{A}} = \begin{pmatrix} -\frac{\kappa}{2} & 0 & 0 & G_- \\ 0 & -\frac{\kappa}{2} & -G_+ & 0 \\ 0 & G_- & -\frac{\gamma}{2} & \tilde{G}_- \\ -G_+ & 0 & -\tilde{G}_+ & -\frac{\gamma}{2} \end{pmatrix}, \qquad (4.8)
$$

with $G_\pm = G_0 \pm G_1$ and $\tilde{G}_\pm = \tilde{G}_0 \pm \tilde{G}_1$.

DIGRESSION 4.1

**Dynamical Stability under RWA**

To ascertain the dynamical stability of our system under RWA, we apply the Routh-Hurwitz criteria discussed in Digression 1.3 for the drift matrix in Equation (4.8). This gives us the following conditions:

$$
\begin{aligned}
\gamma+\kappa &> 0,\\
\frac{1}{4}\left(\gamma^2+4\gamma\kappa+\kappa^2\right)+2G_-G_+ + \tilde{G}_-\tilde{G}_+ &> 0,\\
\tilde{G}_-\tilde{G}_+\kappa + \left(\frac{1}{4}\gamma\kappa + G_-G_+\right)(\gamma+\kappa) &> 0,\\
\frac{\kappa^2}{16}\left(4\tilde{G}_-\tilde{G}_+ + \gamma^2\right) + G_-^2G_+^2 + \frac{\gamma\kappa}{2}G_-G_+ &> 0.
\end{aligned}
$$

In the rest of our analysis, we verify that the above conditions are met at all times during the evolution of our system.

TH-3401_186121105

Figure 4.3 presents the time-evolution of the variances of the position and momentum quadratures in the presence of amplitude-modulated laser drive. Without RWA, the quadrature variances display oscillatory dynamics in the long-time limit. Under RWA, the variance in the quadratures follow the extremas of the otherwise oscillatory dynamics. It can be seen here that the maximum amount of squeezing achieved in the position quadrature for both the un-approximated and approximated scenarios is the same. We therefore utilize the dynamical values obtained under RWA for the rest of our analysis.

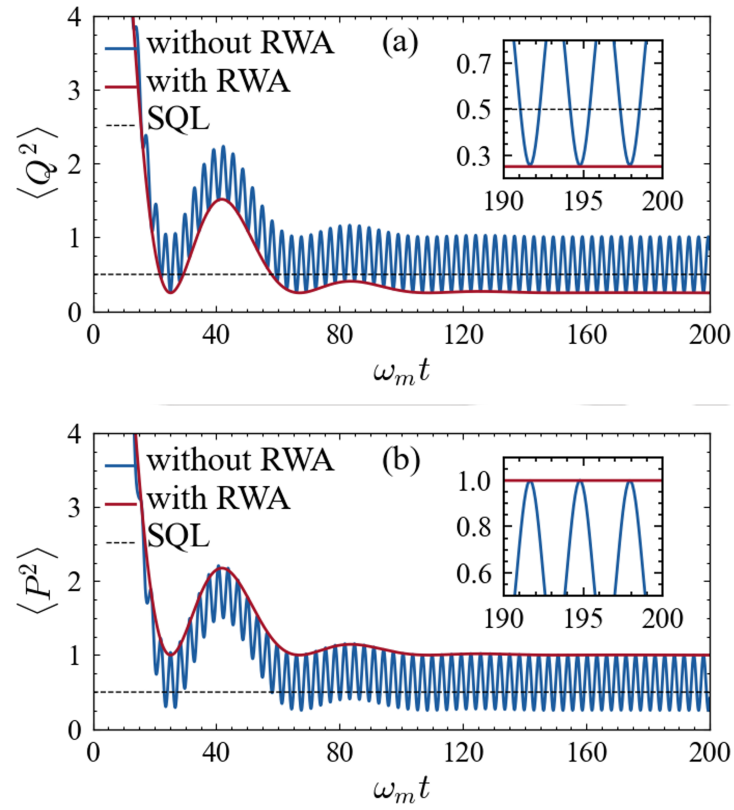


**Figure 4.3:** Time-evolution of the variance in (a) position fluctuation ($Q$) and (b) momentum fluctuation ($P$) with RWA (solid red) and without RWA (solid blue). The thin dashed line denotes the standard quantum limit. The insets illustrate the closeness of the minimum (maximum) values of the variance in position (momentum) with and without RWA once the system reaches periodic dynamics. The parameters used are $\Delta_1 = -\omega_m$, $g_1 = 10^{-4}\omega_m$, $\Omega_a = \Omega_b = 2\omega_m$, $\kappa = 0.1\omega_m$, $\gamma = 10^{-6}\omega_m$, $a_0 = 2.0$, $a_{\pm 1} = 0.2$, $b_0 = 100$, $b_{\pm 1} = 25$, $n_a = 0$ and $n_b = 10$.

TH-3401_186121105

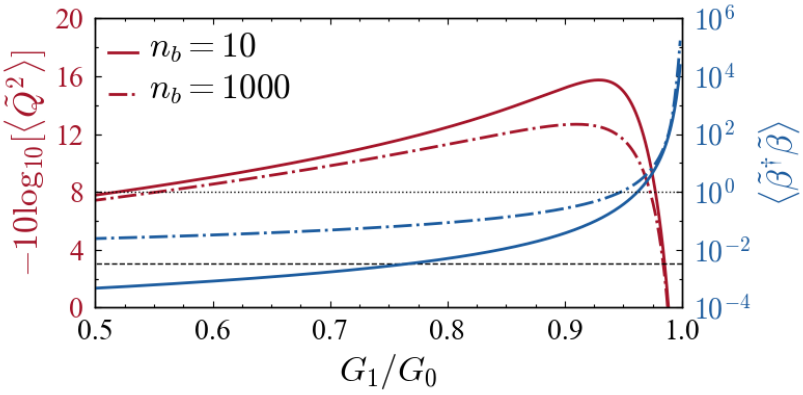


**Figure 4.4:** Behaviour of the steady-state variance in the position quadrature $\langle\tilde{Q}^2\rangle$ under RWA (red) and occupancy of the Bogoliubov mode $\langle\tilde{\beta}^\dagger\tilde{\beta}\rangle$ (blue) with variation in the ratio of the sideband coupling strengths $G_1/G_0$ for $n_b = 10$ (solid) and $n_b = 1000$ (dot dashed). Here, we have used $(b_{-1} + b_1) \in (0, 225.0]$ to obtain the given range of $G_1/G_0$ with $\omega_m t_{\max} = 10^3$. The thin dashed line denotes the SQL and the region under the thin dotted one corresponds to the cooling of the Bogoliubov mode ($\langle\tilde{\beta}^\dagger\tilde{\beta}\rangle < 1$). Other parameters are the same as in Figure 4.3.

In Figure 4.4, we show the maximum squeezing in the mechanical position for a wide range of the ratio $G_1/G_0$ in the long-time limit. We observe that the squeezing initially increases with the increase in the sideband ratio. However, as its value approaches unity, it suddenly drops and the corresponding variances exceed the SQL. To understand this behaviour of steady-state squeezing under RWA more intuitively, we perform the Bogoliubov mode transformation on the mechanical mode such that $\tilde{\beta} = \cosh[r]\tilde{b} + \sinh[r]\tilde{b}^\dagger$, where $r = \arctan[G_1/G_0]$ [159] (refer to Appendix C for detailed derivation). This transforms Equations (4.6) to

$$\dot{\tilde{a}} = -i\mathcal{G}\tilde{\beta} - \frac{\kappa}{2}\tilde{a} + \sqrt{\kappa}\tilde{a}_{in}, \tag{4.10a}$$

$$\dot{\tilde{\beta}} = -i\mathcal{G}\tilde{a} - \frac{\gamma}{2}\tilde{\beta} + \sqrt{\gamma}\tilde{\beta}_{in} - i\left\{\left(\frac{G_0^2 + G_1^2}{\mathcal{G}^2}\right)\tilde{G}_0 - \frac{2G_1G_0}{\mathcal{G}^2}\tilde{G}_1\right\}\tilde{\beta} - i\left\{\left(\frac{G_0^2 + G_1^2}{\mathcal{G}^2}\right)\tilde{G}_1 - \frac{2G_1G_0}{\mathcal{G}^2}\tilde{G}_0\right\}\tilde{\beta}^\dagger, \tag{4.10b}$$

where $\mathcal{G} = \sqrt{G_0^2 - G_1^2}$ is the effective coupling between the optical mode and the mechanical Bogoliubov mode, with $\tilde{\beta}_{in} = \cosh[r]\tilde{b}_{in} + \sinh[r]\tilde{b}_{in}^\dagger$. It can be

TH-3401_186121105

easily shown that the optomechanical interaction that describes Equations (4.10) takes the form $H_i = \mathcal{G}(\tilde{a}^\dagger\tilde{\beta}+\tilde{a}\tilde{\beta}^\dagger)$. This Hamiltonian is analogous to the beam-splitter interaction which describes the energy exchange between the optical and mechanical mode and is widely applied for mechanical sideband cooling [16, 190]. In our case, the Bogoliubov mode $\tilde{\beta}$ undergoes ground-state cooling by interacting with the optical mode $\tilde{a}$. Further, the squeezing parameter $r = \tanh^{-1}[G_1/G_0]$ increases with an increase in $G_1$ for a given $G_0$. This enhances the squeezing of the mechanical mode initially. However, as $G_1$ approaches $G_0$, the effective coupling parameter $\mathcal{G} = \sqrt{G_0^2 - G_1^2}$ goes to zero, decoupling the optical mode from the mechanical Bogoliubov mode. At this point, the cooling of the Bogoliubov mode no longer takes place and there is a sharp increase in its steady-state occupancy, $\langle\tilde{\beta}^\dagger\tilde{\beta}\rangle$ (refer to Figure 4.4). After this stage, the effects of thermal noises dominate, making it impossible to achieve high degrees of squeezing. This is shown by the abrupt fall of $-10\log_{10}[\langle\tilde{Q}^2\rangle]$ around $G_1/G_0$ values corresponding to $\langle\tilde{\beta}^\dagger\tilde{\beta}\rangle > 1$. Thus, there exists an optimal value of the sideband ratio for maximum squeezing.

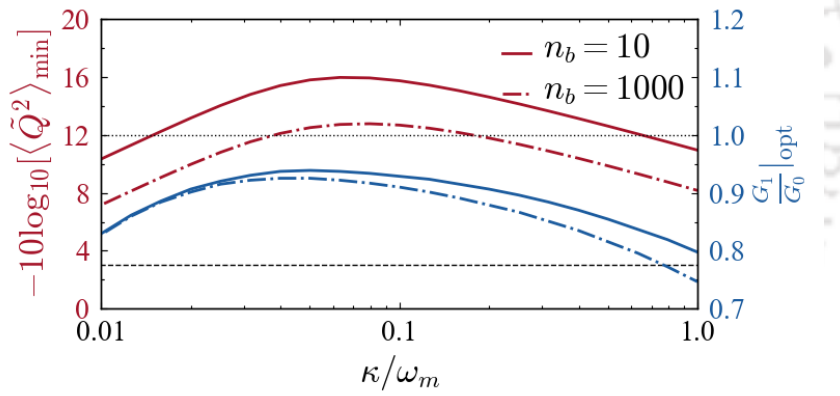


**Figure 4.5:** Maximum squeezing in the position quadrature, $-10\log_{10}[\langle\tilde{Q}^2\rangle_{\min}]$ (red), and the corresponding optimal sideband ratios, $G_1/G_0$ (blue), plotted against the variation in the decay rate $\kappa$ for $n_b = 10$ (solid) and $n_b = 1000$ (dot dashed) with $\omega_m t_{\max} = 10^4$. The thin dashed line denotes the SQL while the dotted one represents $G_1 = G_0$. Other parameters are same as in Figure 4.4.

We now numerically analyze the effect of optical dissipation on the optimal value of the sideband ratio. In Figure 4.5, we show that the minimum quadrature variance $\langle\tilde{Q}^2\rangle_{\min}$ for a specific value of the sideband ratio increases with an increase in $\kappa$ only up to a certain threshold. As $\kappa$ is increased further, the magnitude of squeezing decreases [159]. We also plot the optimal values

TH-3401_186121105

of $G_1/G_0$ from the position of maximum squeezing (for example, from Figure 4.4) by varying $\kappa$. We find that this typical choice of $G_1/G_0$ is close to 1. Similar to the maximum value of squeezing, the value of the optimal ratio also decreases for higher values of dissipation. It may be noted here that with an increase in the phonon number, the minimum value of $\langle\tilde{Q}^2\rangle$ increases due to the effect of thermal noise. For our system, even for a hundred-fold increase in thermal occupancy, the amount of squeezing obtained remains significantly above the SQL. This is shown in Figure 4.6. Alongside this, we also plot the behaviour of entanglement between the optical and mechanical modes of our system at the points where the maximum squeezing is observed. Here, we have used the logarithmic negativity quantifier introduced in Section 1.2.3. Similar to the behaviour of squeezing, we observe that the entanglement between the modes is robust up to a few tens of thermal photons. However, the value of observed entanglement is very small for smaller values of $G_1/G_0$ and greatly enhances when the ratio is close to unity. In the next section, we present a multi-modulated system to generate significant entanglement.

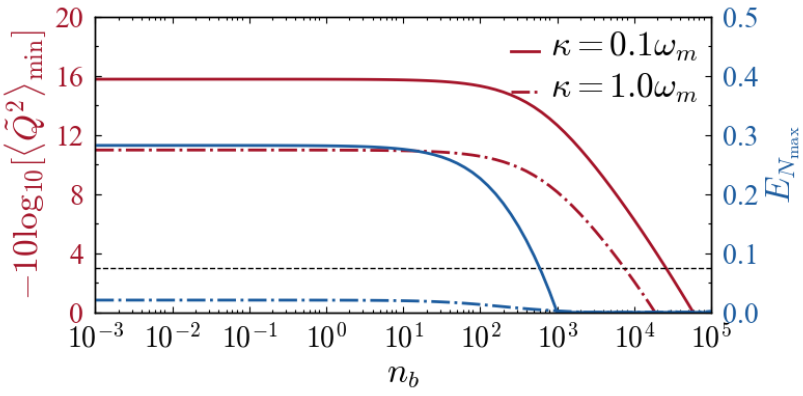


**Figure 4.6:** Maximum squeezing in the position quadrature, $-10\log_{10}[\langle\tilde{Q}^2\rangle_{\min}]$ (red), and corresponding optomechanical entanglement, $E_N$ (blue) with varying occupancies of the mechanical mode, $n_b$ for $\kappa \in \{0.1, 1.0\}\omega_m$ at optimal values of $G_1/G_0$. Here, $\omega_m t_{\max} = 10^3$. The thin dashed line in the figure denotes the SQL. Other parameters are the same as in Figure 4.3.

NOTE

*Most modulation proposals for mechanical squeezing in dissipative systems apply two-tone driving [152, 159, 164, 191], which may induce instability [20].*

TH-3401_186121105

## 4.3 Optoelectrical Entanglement and Mechanical Squeezing in a Multi-modulated System

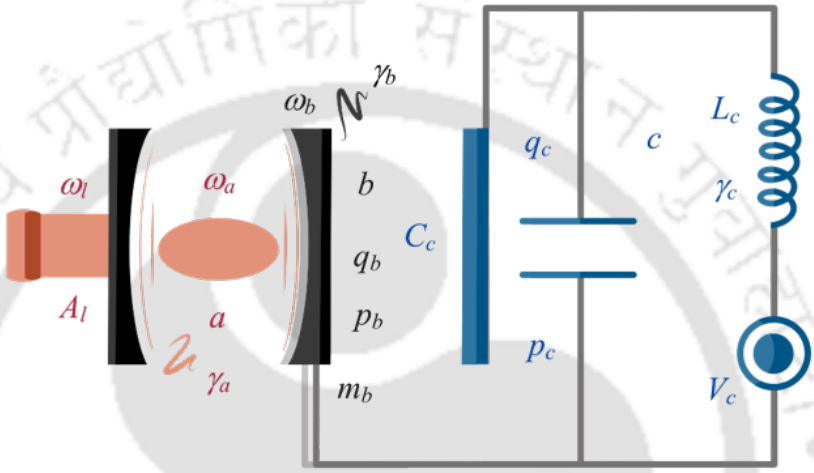


**Figure 4.7:** Illustration of the complete opto-electro-mechanical system. The moveable end-mirror of a laser-driven optomechanical cavity (left half) is capacitively coupled to an LC circuit (right half) connected to a voltage source.

The schematics of our hybrid system is depicted in Figure 4.7, where a driven cavity optomechanical system is coupled to an LC circuit via its mechanical end-mirror. A metallic coating on the end-mirror serves as one plate of a parallel-plate capacitor. The radiation pressure of the laser imparts momentum to the moveable end-mirror. This couples the cavity mode to the mechanical mode. The displacement of the mirror also alters the capacitance, thereby coupling it to the LC circuit mode. An external voltage drives the LC circuit. The complete Hamiltonian of the system can be expressed as [179]

$$\begin{aligned} H &= \hbar\omega_a a^\dagger a + \frac{1}{2}m_b\omega_b^2 q_b^2 + \frac{p_b^2}{2m_b} + \frac{q_c^2}{2C_c} + \frac{p_c^2}{2L_c} \\ &\quad + i\hbar\left(A_l a^\dagger e^{-i\omega_l t} - A_l^* a e^{i\omega_l t}\right) - q_c V_c. \end{aligned} \tag{4.11}$$

Here, the second (fourth) and third (fifth) terms together represent the mechanical (LC circuit) energy satisfying $[q_j, p_j] = i\hbar$, $q_j$ and $p_j$ being the position (charge) and momentum (flux) operators ($j \in \{b, c\}$ unless specified

TH-3401_186121105

otherwise). Unlike the symbols used in Section 1.1, here we use the subscripts $a$, $b$ and $c$ to denote the optical mode, the mechanical mode and the LC circuit mode respectively. Thus, $m_b$ and $\omega_b$ denote the effective mass and frequency of the mechanical end-mirror whereas the LC circuit's total capacitance and inductance are denoted by $C_c$ and $L_c$. The electromechanical coupling is *capacitive* in nature, with a total capacitance of $C_c = C_{cp} + C_{c0}d/(d - q_b)$, where $d$ is the unperturbed distance between the parallel plates and $C_{c0}$ ($C_{cp}$) is the base (parasitic) capacitance of the LC circuit. The final term in Equation (4.11) is the energy of the voltage drive with amplitude $V_c$.

To analyze the collective dynamics of the system, we rewrite this Hamiltonian in terms of the dimensionless mode operators $j$ with $q_j = q_{jZP}(j^\dagger + j)$ and $p_j = ip_{jZP}(j^\dagger - j)$, such that $[j, j^\dagger] = 1$. $q_{jZP}$ and $p_{jZP}$ are the corresponding zero-point values. In the rotating frame of the laser frequency $\omega_l$, the total Hamiltonian takes the form (refer to Appendix D for its derivaiton)

$$\begin{aligned} H &= -\hbar\Delta_0 a^\dagger a + \hbar\omega_b b^\dagger b - \hbar g_0 a^\dagger a\left(b^\dagger + b\right) + i\hbar\left(A_l a^\dagger - A_l^* a\right) \\ &\quad + \hbar\omega_c c^\dagger c - \hbar g_1\left(b^\dagger + b\right)\left(c^\dagger + c\right)^2 - \hbar A_v\left(c^\dagger + c\right), \end{aligned} \tag{4.12}$$

APPROXIMATION

*While deriving Equation (4.12), we have neglected the terms quadratic or higher in $q_b/d$, assuming that the displacements are much smaller the separation between the parallel plates.*

where $\omega_c = 1/\sqrt{L_c(C_{cp} + C_{c0})}$ is the resonance frequency of the LC circuit and $A_v = q_{cZP}V_c/\hbar$ is the normalized amplitude of the voltage drive. This gives us the electromechanical coupling strength

$$g_1 = \frac{r^2 q_{b_{ZP}} q_{c_{ZP}}^2}{2\hbar C_{c0} d}, \tag{4.13}$$

where $r = C_{c0}/(C_{cp}+C_{c0})$ is the participation ratio of the capacitance. It can be seen from Equation (4.12) that $g_1$ is constraint by the physical parameters of the system. For an LC circuit operating in the radio frequency with $\mu$m-scale parallel-plates and for a weak optomechanical coupling, the ratio $g_1/g_0$ is constraint to $\sim 10^2 r$, where $r$ is typically of the order of $10^{-3}$ [181].

We now introduce the modulations corresponding to the laser amplitude as $A_l = A_{l0} + \sum_{k=\pm1} A_{lk}e^{-ik\Omega_l t}$, the voltage amplitude as $A_v = A_{v0} + A_{v1}\cos(\Omega_v t)$ and the mechanical frequency as $\omega_b = \omega_{b0}\sqrt{\{1 + \theta\cos(\Omega_s t)\}}$ (which results from the modulation of the mechanical spring constant). Such a voltage drive amplitude can be realized by using an AC signal with a DC

TH-3401_186121105

bias. The modulation of the mechanical spring constant can be realized using a parametric oscillator [189, 192–194] or through an ancilla cavity with a quadratic optomechanical coupling [195, 196]. Assuming that the modulation of the laser drive amplitude is gentle [40] whereas those of the voltage drive amplitude and the mechanical spring constant are strong, we obtain

$$\dot{a} = -\left(\frac{\gamma_a}{2} - i\Delta_0\right) a + ig_0 a\left(b^\dagger + b\right) + A_l + \sqrt{\gamma_a} a_{in}, \tag{4.14a}$$

$$\dot{b} = -\left(\frac{\gamma_b}{2} + i\omega_b\right) b + ig_0 a^\dagger a + ig_1\left(c^\dagger + c\right)^2 + \sqrt{\gamma_b} b_{in}, \tag{4.14b}$$

$$\dot{c} = -\left(\frac{\gamma_c}{2} + i\omega_c\right) c + 2ig_1\left(b^\dagger + b\right)\left(c^\dagger + c\right) + iA_v + \sqrt{\gamma_c} c_{in}. \tag{4.14c}$$

The dynamics of the linearized quantum fluctuations can then be derived as

$$\delta\dot{a} = -\left(\frac{\gamma_a}{2} - i\Delta\right)\delta a + iG_\alpha\left(\delta b^\dagger + \delta b\right) + \sqrt{\gamma_a} a_{in}, \tag{4.15a}$$

$$\begin{aligned}\delta\dot{b} = &-\left(\frac{\gamma_b}{2} + i\omega_b\right)\delta b + iG_\alpha \delta a^\dagger + iG_\alpha^* \delta a \\ &+2iG_\chi\left(\delta c^\dagger + \delta c\right) + \sqrt{\gamma_b} b_{in},\end{aligned} \tag{4.15b}$$

$$\begin{aligned}\delta\dot{c} = &-\left(\frac{\gamma_c}{2} + i\omega_c\right)\delta c + 2iG_\chi\left(\delta b^\dagger + \delta b\right) \\ &+2iG_\beta\left(\delta c^\dagger + \delta c\right) + \sqrt{\gamma_c} c_{in}.\end{aligned} \tag{4.15c}$$

In deriving these equations, we have introduced three new terms. The first one is $G_\alpha = g_0\alpha$, which enhances the intrinsic optomechanical coupling by a factor proportional to the intra-cavity field. The second one is $G_\beta = g_1\left(\beta^* + \beta\right)$, which detunes the frequency of the oscillating electrical flux. The final term is $G_\chi = g_1\left(\chi^* + \chi\right)$, with $\chi = \langle c\rangle$, which accounts for the back-action of the mechanical position on the LC circuit mode and that of the LC circuit charge on the mechanical mode. Equations (4.15) then gives us

$$\mathbf{A} = \begin{pmatrix} -\frac{\gamma_a}{2} & -\Delta & -2G_{\alpha I} & 0 & 0 & 0 \\ \Delta & -\frac{\gamma_a}{2} & 2G_{\alpha R} & 0 & 0 & 0 \\ 0 & 0 & -\frac{\gamma_b}{2} & \omega_b & 0 & 0 \\ 2G_{\alpha R} & 2G_{\alpha I} & -\omega_b & -\frac{\gamma_b}{2} & 4G_\chi & 0 \\ 0 & 0 & 0 & 0 & -\frac{\gamma_c}{2} & \omega_c \\ 0 & 0 & 4G_\chi & 0 & -\omega_c + 4G_\beta & -\frac{\gamma_c}{2} \end{pmatrix}, \tag{4.16}$$

as the drift matrix of the quadratures, where $G_{\alpha R}$ and $G_{\alpha I}$ are the real and imaginary parts of $G_\alpha$, with $D = \mathrm{Diag}[\gamma_a/2, \gamma_a/2, \gamma_b(n_{th_b} + 1/2), \gamma_b(n_{th_b} + 1/2), \gamma_c(n_{th_c} + 1/2), \gamma_c(n_{th_c} + 1/2)]$ as the noise correlation matrix.

TH-3401_186121105

DIGRESSION 4.2

**Choice of Numerical Parameters and Dynamical Stability**

To estimate the numerical ranges of the parameters for which the system is stable, we first study the steady state of the system in the *absence* of all modulations, i.e., with $A_l = A_{l0}$, $A_v = A_{v0}$ and $\omega_b = \omega_{b0}$. To do this, we set the classical mode rates obtained from Equations (4.14) to zero and obtain the coupled steady-state equations for the intra-cavity photon number, the mechanical position and the electrical charge as,

$$\begin{aligned}
\alpha_s^*\alpha_s &= \frac{4A_{l0}^*A_{l0}}{\gamma_a^2 + 4\left\{\Delta_0 + g_0\left(\beta_s^* + \beta_s\right)\right\}^2}, \\
\beta_s^* + \beta_s &= \frac{8\omega_{b0}\left\{g_0\alpha_s^*\alpha_s + g_1\left(\chi_s^* + \chi_s\right)^2\right\}}{\gamma_b^2 + 4\omega_{b0}^2}, \\
\chi_s^* + \chi_s &= \frac{8\omega_c A_{v0}}{\gamma_c^2 + 4\omega_c^2 - 16\omega_c g_1\left(\beta_s^* + \beta_s\right)}.
\end{aligned}$$

Solving these steady-state equations in terms of $\beta_s$, we get a polynomial equation of the form $\Sigma_{k=0}^{5} e_k(\beta_s^* + \beta_s)^{5-k} = 0$ where the coefficients are

$$\begin{aligned}
e_0 &= 16g_0^2g_1^2\omega_c^2\left(\frac{\gamma_b^2}{4} + \omega_{b0}^2\right), \\
e_1 &= -8g_0g_1\omega_c\left\{-4\Delta_0 g_1\omega_c + g_0\left(\frac{\gamma_c^2}{4} + \omega_c^2\right)\right\}\left(\frac{\gamma_b^2}{4} + \omega_{b0}^2\right), \\
e_2 &= \left[16\left({\Delta_0}^2 + \frac{\gamma_a^2}{4}\right)g_1^2\omega_c^2 + g_0\left(\frac{\gamma_c^2}{4} + \omega_c^2\right)\left\{-16\Delta_0 g_1\omega_c\right.\right. \\
&\quad \left.\left. + g_0\left(\frac{\gamma_c^2}{4} + \omega_c^2\right)\right\}\right]\left(\frac{\gamma_b^2}{4} + \omega_{b0}^2\right), \\
e_3 &= -2\left\{-\Delta_0 g_0\left(\frac{\gamma_c^2}{4} + \omega_c^2\right) + 4g_1\omega_c\left({\Delta_0}^2 + \frac{\gamma_a^2}{4}\right)\right\}\left(\frac{\gamma_b^2}{4} + \omega_{b0}^2\right) \\
&\quad \times\left(\frac{\gamma_c^2}{4} + \omega_c^2\right) - 8g_0g_1\omega_{b0}\omega_c^2\left(4g_1A_{l0}^2 + g_0A_{v0}^2\right),
\end{aligned}$$

TH-3401_186121105

$$
\begin{aligned}
e_4 &= \left(\Delta_0{}^2 + \frac{\gamma_a^2}{4}\right)\left(\frac{\gamma_b^2}{4} + \omega_{b0}^2\right)\left(\frac{\gamma_c^2}{4} + \omega_c^2\right)^2 \\
&\quad +16 g_0 g_1 \omega_{b0}\omega_c \left\{A_{l0}^2\left(\frac{\gamma_c^2}{4} + \omega_c^2\right) - A_{v0}^2 \Delta_0 \omega_c\right\}, \\
e_5 &= -2A_{l0}^2 g_0 \omega_{b0}\left(\frac{\gamma_c^2}{4} + \omega_c^2\right)^2 - 8A_{v0}^2 g_1 \omega_{b0}\omega_c^2\left(\Delta_0{}^2 + \frac{\gamma_a^2}{4}\right).
\end{aligned}
$$

The real roots of this equation depict the steady-state mechanical positions. We use these values to numerically obtain the regions of mono-stability at the intrinsic mechanical frequency. The choice of parameter values is motivated by some of the recent works in opto-electro-mechanical systems [44, 45, 197] as well as relevant works in modulated optomechanics [40, 188, 189]. From our analysis, we determine the feasible ranges of laser and voltage drive amplitudes such that the system is away from multi-stability. We further verify that stability holds for fixed values of amplitudes within those ranges by choosing different mechanical spring constants around the intrinsic one.

In the presence of modulations, the classical amplitudes do not settle into a steady state. Instead, they display oscillatory dynamics in the long time limit [40] due to the presence of the time-dependent parameters $\Delta$, $G_\alpha$, $G_\beta$ and $G_\chi$. We, therefore, incorporate the Routh-Hurwitz criteria discussed in Digression 1.3 to determine the dynamical stability using the characteristic equation for the drift matrix, $\sum_{k=0}^{6} e_k \lambda^{6-k} = 0$, where the coefficients are

$$
\begin{aligned}
e_0 &= 1, \\
e_1 &= \gamma_a + \gamma_b + \gamma_c, \\
e_2 &= D^2 + O_b^2 + O_c^2 + (\gamma_b\gamma_c + \gamma_b\gamma_a + \gamma_c\gamma_a), \\
e_3 &= D^2(\gamma_b + \gamma_c) + \gamma_a\gamma_b\gamma_c + \gamma_b O_c^2 + \gamma_c O_b^2 + \gamma_a\left\{O_b^2 + O_c^2\right\}, \\
e_4 &= D^2\left\{O_b^2 + O_c^2 + \gamma_b\gamma_c\right\} + 4\Delta\left|G_\alpha\right|^2\omega_b + \gamma_a\left\{\gamma_b O_c^2 + \gamma_c O_b^2\right\} \\
&\quad + O_b^2 O_c^2 - 16 G_\chi^2 \omega_b\omega_c, \\
e_5 &= D^2\left\{\gamma_b O_c^2 + \gamma_c O_b^2\right\} + 4\Delta\left|G_\alpha\right|^2\gamma_c\omega_b \\
&\quad + \gamma_a\left\{O_b^2 O_c^2 - 16 G_\chi^2\omega_b\omega_c\right\}, \\
e_6 &= D^2\left\{O_b^2 O_c^2 - 16 G_\chi^2\omega_b\omega_c\right\} + 4\Delta\left|G_\alpha\right|^2 O_c^2\omega_b,
\end{aligned}
$$

with $D^2 = \Delta^2 + \gamma_a^2/4$, $O_b^2 = \gamma_b^2/4 + \omega_b^2$ and $O_c^2 = \gamma_c^2/4 + \omega_c\{\omega_c - 4G_\beta\}$.

TH-3401_186121105

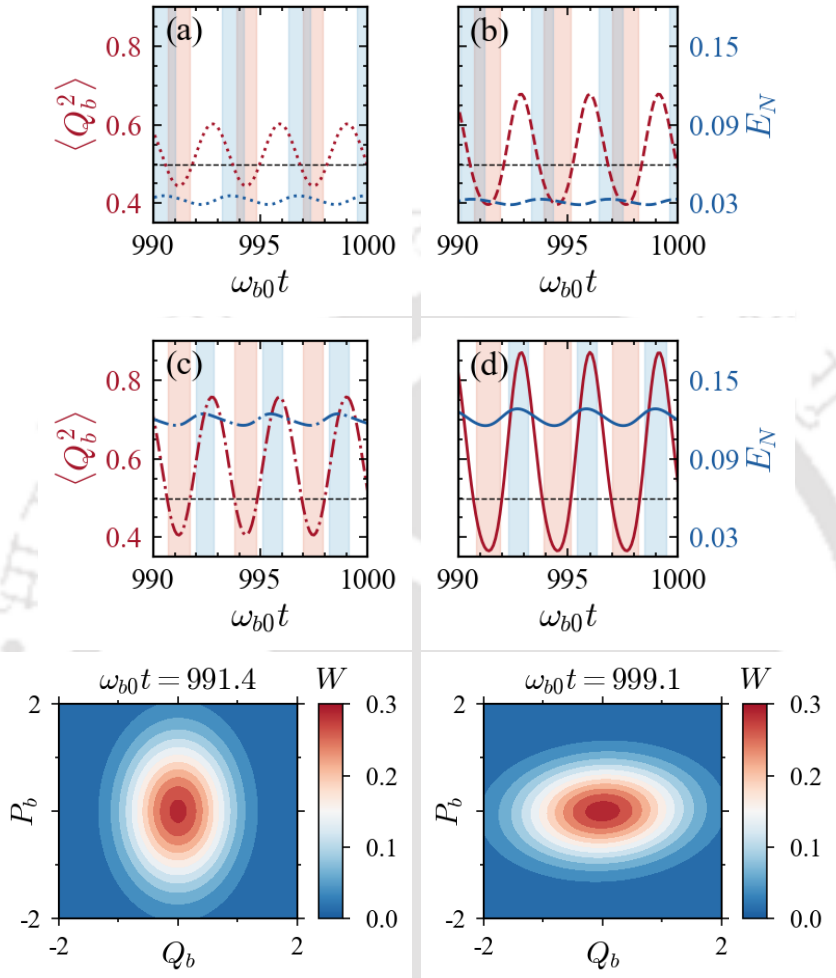


**Figure 4.8:** *Line Plots:* Dynamics of the variance in the mechanical position, $\langle Q_b^2 \rangle$ (red), and the optoelectrical entanglement, $E_N$ (blue), in the presence of (a) only the laser modulation (dotted), (b) laser and spring constant modulation (dashed), (c) laser and voltage modulation (dash-dotted) and (d) all three types of modulations (solid). The dashed black line represents the SQL for the mechanical variance. The shaded regions represent high values of squeezing and entanglement. *Contour Plots:* Wigner distributions depicting the degree of squeezing with time in the presence of all modulations. Other parameters (in units of $\omega_{b0}$) are $A_{l0} = 100$, $A_{l\pm} = 10$, $A_{v0} = 50$, $A_{v1} = 100$, $\Delta_0 = -1$, $\gamma_a = 0.2$, $\gamma_b = 2 \times 10^{-6}$, $\gamma_c = 0.02$, $g_0 = 10^{-3}$, $g_1 = 2 \times 10^{-4}$, $\Omega_l = 2$, $\Omega_v = 2$, $\Omega_s = 2$ and $\omega_c = 1.1$, with $\theta = 0.5$.

TH-3401_186121105

NOTE

*In the mono-stable regime of the system, neither optoelectrical entanglement nor high mechanical squeezing is observed when the modulations are absent.*

It has been well-established in several works that incorporating a laser modulation not only enhances the degree of maximum bipartite entanglement between the optics and mechanics, but also helps surpass the standard quantum limit of the mechanical position [40, 198, 199]. In our system, since the mechanical mirror is simultaneously coupled to the LC circuit mode, the optical and electrical modes get entangled through the mechanical mode. We plot the corresponding optoelectrical entanglement and variance of the mechanical position in the presence of only the laser modulation in Figure 4.8(a). We find that the windows of maximas in entanglement and squeezing can be tuned by varying the voltage drive amplitude. This effect can be predicted from Equations (4.15), where the magnitude of LC circuit charge alters the amplitude of the mechanical mode and therby introduces a shift in optical frequency. It is worth mentioning here that a finite amount of *optomechanical* entanglement is observed corresponding to the windows of high mechanical squeezing. Further, since the optomechanical cavity is driven by a red-detuned laser, the mechanical motion simultaneous cools down.

NOTE

*The phenomena are robust upto a few hundred milli-Kelvins of phonon bath temperatures but only upto a few hundred micro-Kelvins of the LC circuit bath.*

Together with the laser modulation, we now introduce the mechanical spring constant modulation. This results in a higher degree of squeezing in the mechanical position as shown in Figure 4.8(b). For our set of parameters, the minimum quadrature variance decreases to $\approx 0.4$ from $\approx 0.44$ in Figure 4.8(a). However, the maximum optoelectrical entanglement decreases slightly. Next, we implement the laser modulation along with the voltage modulation without modulating the spring constant. This enhances the maximum degree of generated optoelectrical entanglement significantly with a value of $\approx 0.12$ as shown in Figure 4.8(c) compared to just $\approx 0.04$ in Figure 4.8(a). Finally, as depicted in Figure 4.8(d), both the maximum values of optoelectrical entanglement and mechanical squeezing are sufficiently enhanced in the presence of all three modulations. The corresponding values are $E_{N_{\max}} \approx 0.13$ and $\langle Q_b^2 \rangle_{\min} \approx 0.36$, denoting a squeezing of 28%.

TH-3401_186121105

To understand the role of modulation frequency on the enhancement of entanglement, let us write the linearized Hamiltonian that describes Equations (4.15) in terms of the effective parameters as,

$$\begin{aligned} H_l &= -\hbar\Delta\delta a^\dagger\delta a + \hbar\omega_b\delta b^\dagger\delta b + \hbar\omega_c\delta c^\dagger\delta c - \hbar\left(G_\alpha\delta a^\dagger + G_\alpha^*\delta a\right)\left(\delta b^\dagger + \delta b\right) \\ &\quad -2\hbar G_\chi\left(\delta b^\dagger + \delta b\right)\left(\delta c^\dagger + \delta c\right) - \hbar G_\beta\left(\delta c^\dagger\delta c^\dagger + \delta c\delta c\right). \end{aligned} \tag{4.21}$$

One can approximate this Hamiltonian with $\Delta \approx -\omega_{b0}$ (red detuned), $\omega_c \approx \omega_{b0}$ and $\omega_b \approx \omega_{b0}$ and obtain the linearized interaction Hamiltonian as

$$\begin{aligned} H_i &\approx -\hbar\Big\{G_\alpha\left(\delta a^\dagger\delta b^\dagger e^{2i\omega_{b0}t} + \delta a^\dagger\delta b\right) + G_\alpha^*\left(\delta a\delta b^\dagger + \delta a\delta b e^{-2i\omega_{b0}t}\right) \\ &\quad +2G_\chi\left(\delta b^\dagger\delta c^\dagger e^{2i\omega_{b0}t} + \delta b^\dagger\delta c + \delta b\delta c^\dagger + \delta b\delta c e^{-2i\omega_{b0}t}\right) \\ &\quad +G_\beta\left(\delta c^\dagger\delta c^\dagger e^{2i\omega_{b0}t} + \delta c\delta c e^{-2i\omega_{b0}t}\right)\Big\}. \end{aligned} \tag{4.22}$$

In the long time limit, the classical amplitudes $\alpha$, $\beta$ and $\chi$ acquire the same form as their external driving fields [20,40], such that when $\Omega_{l,v,s} = 2\omega_{b0}$, we have $\mathcal{C} \approx \mathcal{C}_- e^{2i\omega_{b0}t} + \mathcal{C}_0 + \mathcal{C}_+ e^{-2i\omega_{b0}t}$, where $\mathcal{C} \in \{\alpha, \beta, \chi\}$. Substituting these values and neglecting the terms rotating at frequencies $\pm 2\omega_{b0}$ and $\pm 4\omega_{b0}$ under the rotating wave approximation, we obtain the Hamiltonian

$$\begin{aligned} \tilde{H}_i &\approx -\hbar g_0\left(\alpha_+\delta a^\dagger\delta b^\dagger + \alpha_0\delta a^\dagger\delta b + \alpha_0^*\delta a\delta b^\dagger + \alpha_+^*\delta a\delta b\right) \\ &\quad -2\hbar g_1\left(\chi_-^* + \chi_+\right)\left(\delta b^\dagger\delta c^\dagger + \delta b\delta c\right) - 2\hbar g_1\left(\chi_0^* + \chi_0\right)\left(\delta b^\dagger\delta c + \delta b\delta c^\dagger\right) \\ &\quad -\hbar g_1\left(\beta_-^* + \beta_+\right)\left(\delta c^\dagger\delta c^\dagger + \delta c\delta c\right). \end{aligned} \tag{4.23}$$

It can be easily seen from here that the resonant interaction of the down-converted LC circuit mode with the mechanical mode gives rise to entanglement between them. Similarly, the optical mode gets entangled with the mechanical mode through a two-mode squeezed interaction. The mechanical mirror then mediates the entanglement between the optical and LC circuit modes via two distinct processes: (i) the frequency shifts due to the mechanical position, and (ii) the backactions of the mechanical position. To verify our analysis, we numerically simulate the behaviour of maximum optoelectrical entanglement and minimum quadrature variance that can be achieved around the optimal modulation frequencies.

TH-3401_186121105

NOTE

*When the resonance condition is not satisfied, the system dynamics for each set of parameters follows oscillations within a slowly varying envelope. When the modulation frequency is close to resonance, the extremas of this envelope are well-separated in time, spanning several fast oscillations. At resonance, the dynamics settles down into a simple oscillatory state with fixed extremas.*

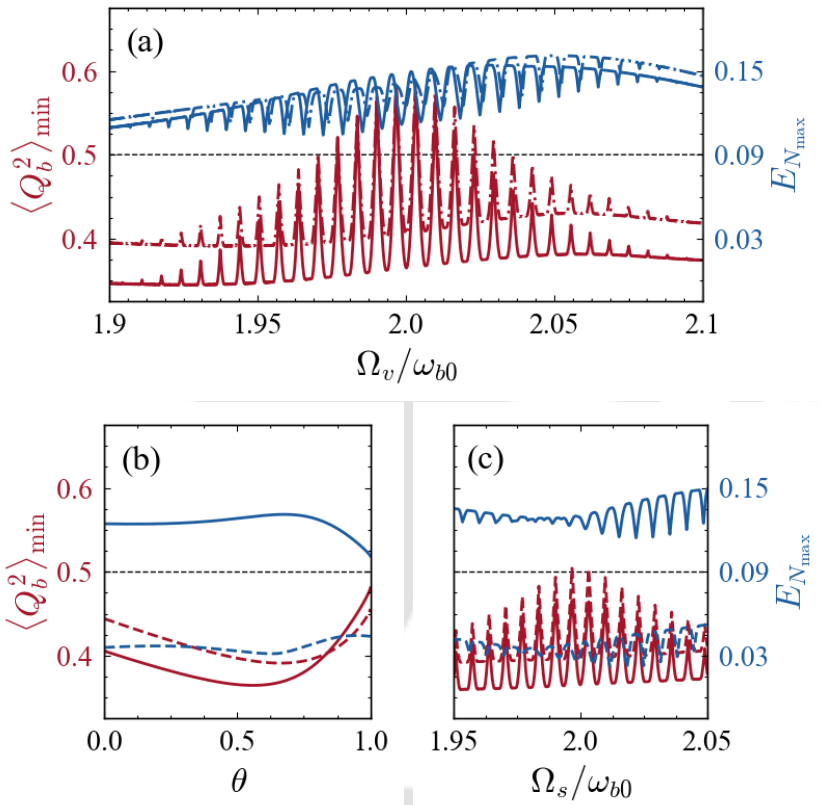


**Figure 4.9:** Minimum values of variance in the mechanical position (red) and maximum values of the optoelectrical entanglement (blue) plotted with (a) variation in the voltage modulation frequency in the absence (dashed dotted) and presence (solid) of spring constant modulation, (b) variation in the modulation amplitude of the spring constant and (c) variation in the modulation frequency of the spring constant in the absence (dashed) and presence (solid) of voltage modulation. The thin dashed line in each of the plots represents the SQL for the mechanical variance. Other parameters are the same as Figure 4.8.

TH-3401_186121105

Figure 4.9(a) shows the variation of these measures with change in the voltage modulation frequency. It can be seen here that the maximum value of entanglement is observed when this frequency is close to twice that of the mechanical frequency. Likewise, the amount of achievable mechanical squeezing reaches its maximum value when the frequency of modulation is close to twice the mechanical frequency and its modulation amplitude is close to half. This can be visualized from Figure 4.9(b-c). We also observe that the electromechanical coupling strength and the LC circuit frequency play an important role in the amount of achievable entanglement between the optical and LC circuit modes. It may be mentioned here that even though the degree of maximum squeezing reported in this work is less in comparison to recent schemes with individual or coupled *optomechanical* systems [20, 188], we report this generation of mechanical squeezing in a hybrid *opto-electro-mechanical* system supporting the simultaneous generation of optoelectrical entanglement. Moreover, although similar works on modulation have been carried out in the context of individual optomechanical and electromechanical systems [189, 198, 199], our work introduces a more general formalism for a compact opto-electro-mechanical system in the presence of all three forms of modulation. The enhancement of *both* optoelectrical entanglement and mechanical squeezing in the presence of multiple modulations, and the observation of alternate maximas of squeezing and entanglement even in the *microwave* or the *radio-frequency* regime are the key findings of this work. The numerical values for the observed maximum entanglement are comparable to previous works for GHz-scale signals [44] or in the strong coupling regime [45]. However, we obtain these values for MHz-scale signals which have several applications in sensing and communication. We also assume a weak coupling regime, making our scheme more feasible experimentally.

## 4.4 Summary of the Chapter

We began this chapter by mentioning the motivation behind generating squeezing in optomechanical systems, and briefly hinted on its applications in the development of quantum devices. We also discussed the importance of quantum entanglement in quantum information processing applications and highlighted a few ways to enhance this quantum signature. We then analyzed the effects of modulations on the enhancement of quantum phenomena in optomechanical systems and presented two of our works to illustrate the same.

TH-3401_186121105

In the first work, we demonstrated the combined effect of pump modulation and cavity dissipation for the generation of mechanical squeezed states in a membrane-in-the-middle optomechanical setup. By introducing a periodic modulation in the amplitude of the external laser field, we observed that, under the rotating wave approximation, the linearized Hamiltonian between the mechanical and the optical mode takes the form of a beam-splitter interaction, which contributes to the ground-state cooling of the mechanical Bogoliubov mode. We then analyzed how the magnitude of squeezing depends on the ratio of the coupling sidebands and numerically optimized this ratio to obtain maximum squeezing for a given cavity dissipation strength. A key outcome of our study is the robustness of the degree of mechanical squeezing and optomechanical entanglement, which stays well above the SQL even for a large thermal noise component in the mechanical mode. The second work that we discussed involved the study of a hybrid opto-electro-mechanical system where the optical and electrical components were coupled through a common mechanical mode. We then systematically studied the effect of multiple modulations — in the amplitudes of the laser and the voltage drives, and the spring constant of the moveable end-mirror — on the generation of optoelectrical entanglement in this system. We reported the enhancement in the achievable entanglement and squeezing in the presence of all three modulations. The generalized dynamics discussed in our work enables us to approach the radio-frequency regime of LC circuit frequencies. Moreover, we perform our analysis in the weak optomechanical coupling regime and with a red-detuned laser which simultaneously cools down the mechanical mirror. A direct advantage of our study is transduction between optical and electrical degrees of freedom, which paves the path towards the development of novel schemes such as quantum radars that rely on opto-electro-mechanical converters for their operation. Another key output of our result — tunable windows of squeezing and entanglement — allows us to periodically estimate the fluctuations entering the system without interfering with the optical-to-electrical transduction.

TH-3401_186121105

CHAPTER

5

# Conclusion

The design and analysis of open quantum systems in the mesoscopic scale is crucial to understand quantum phenomena arising in macroscopic objects. In this thesis, we presented a few such studies involving optomechanical systems. We began Chapter 1 by formalizing the effects of light-matter interaction in optical cavities that contain a mechanically compliant element. By defining the Hamiltonian for such an optomechanical system, we outlined the typical methods that are used to ascertain its stability and obtain the dynamical behaviour of its classical modes and correlations in quantum fluctuations. Finally, we introduced certain measures to estimate classical and quantum properties in such a system and demonstrated them by appropriate choices of the system's parameters and corresponding approximations.

---

Select parts of this chapter are taken from two of our published articles: (1) Phys. Rev. A **107**, 013528 (2023), titled *Synchronization of a Superconducting Qubit to an Optical Field mediated by a Mechanical Resonator* and authored by Roson Nongthombam, Sampreet Kalita and Amarendra K. Sarma [200, 201] (©2023 American Physical Society) and (2) J. Opt. Soc. Am. B **41**, 447 (2024), titled *Quantum Interference induced Magnon Blockade and Antibunching in a Hybrid Quantum System* and authored by Pooja Kumari Gupta, Sampreet Kalita and Amarendra K. Sarma [202, 203] (©2024 Optica Publishing Group). All reproduced content are added with permission.



TH-3401_186121105

In Chapter 2, we elaborated on the theory behind the measure of quantum phase synchronization for coupled harmonic oscillators. We then introduced two different configurations through which nearly-identical optomechanical systems were optically coupled. Here, we observed that these coupled systems maintained a self-sustained oscillatory state in both configurations after an initial transient. In the configuration where there was a reversible exchange of photons between the two cavities, the quantum synchronization between their corresponding mechanical phases displayed a behaviour similar to the Arnold tongue in classical synchronization, reaching highest synchronization in identical oscillators. On the other hand, for the configuration where there was an irreversible exchange of photons from one cavity to the other, the maximum value of synchronization was not observed for identical oscillators. Rather, it peaked at finite detunings between the mechanical frequencies. Also, one could switch between in-phase and anti-phase synchronization by varying this detuning and the photon transmission loss of the optical channel. We explained these observations with analytical reasoning and connected them to the difference in the average phonon numbers of the two mechanical oscillators by analyzing the dynamics of the system in the adiabatic limit.

In Chapter 3, we introduced another hybrid configuration containing an annular Bose-Einstein condensate trapped inside a cavity. Using an equivalent Hamiltonian containing an optical mode and two mechanical modes depicting the Bragg-scattered sidemodes, we employed the toolbox of optomechanics to analyze the steady-state output spectrum of a weak probe beam in the presence of a strong control laser driving the system. An interesting outcome of this study was the detection of rotation of the condensate from the probe transmission profile observed at the output. When the detuning of the control laser was in resonance with the sidemode frequencies, we observed a single transparency window in the absence of atomic circulation. Whereas, in its presence, the profile displayed two transmission windows equidistantly spaced from the pump-probe resonance condition. Moreover, the distance between the transmission peaks increased linearly with the degree of circulation, thereby providing information of the condensate's rotation strength in a minimally destructive manner. Finally, we analyzed the group delay of the probe beam from its dispersion profile by varying the strength of atomic rotation. Similar to the behaviour observed in the transmission profiles, we observed a switching from slow to fast light in the dispersion profile when the condensate started rotating. The magnitude of this change also increased with the strength of rotation.

TH-3401_186121105

In Chapter 4, we first demonstrated the effect of modulations in the laser amplitude on the dynamical behaviour of an optomechanical system and the enhancement observed in its corresponding classical and quantum properties. We then introduced a membrane-in-the-middle system with a quadratic type of optomechanical interaction, and driven by a modulated laser. Choosing a rotating wave approximation that agreed with the minimum variance in the mechanical position, we sought for the optimal sideband modulation amplitudes at which the mechanical squeezing was maximum. We observed that this optimal ratio was related to the occupancy of the mechanical Bogoliubov mode. We also observed that the degree of this squeezing and corresponding optomechanical entanglement was robust to few milliKelvins of temperature. Next, we introduced another hybrid setup where an optical mode was dispersively coupled to a mechanical mode, which in turn was capacitively coupled to an LC circuit mode. Here, we analyzed the effects of three different types of modulations — the laser drive, the voltage drive and the mechanical spring constant. We found that the application of all three modulations at twice the mechanical frequency significantly enhanced the degree of mechanical squeezing and optoelectric entanglement. The observation of tunable windows for maximum squeezing and maximum entanglement was another notable result.

Alongside these, we carried out similar works involving open quantum systems containing mechanical or spin elements that mediate optical and electrical degrees of freedom. In one of them, we proposed the preparation and monitoring of the polarization state of a superconducting qubit using an optical drive via a mechanical membrane [200]. We achieved this controllability through the semi-classical synchronization of one of the bistable states of the qubit with an external reference optical drive. The idea behind such works is the transduction of information between microwave and optical signals, which is at the heart of realizing long-distance communication of quantum information. In another work, we proposed a mechanism to generate antibunched magnons in a hybrid ferromagnet-superconductor system by driving one of two magnon modes inside a cavity containing a qubit [202]. Since the magnon modes were coupled indirectly to the qubit via a microwave drive, the parameters of the qubit could also be used to fine tune this antibunching and achieve magnon blockade in the system. The study of such magnonic systems is currently on the rise owing to their potential implementation as a quantum computing platform. Given the rapid advancement in nanofabrication, we believe that such hybrid systems will be extensively explored in the coming years.

TH-3401_186121105

It is also worth mentioning here that the systems described in this thesis utilized the linearization approximation for the quantum dynamics. This approach is primarily useful (and usually sufficient) in the weak coupling regime where the effect of most higher order coupling terms is almost negligible. Also, such a regime typically favours experimental feasibility. However, the theoretical exploration and experimental setup of open quantum systems in the strong coupling regime is also an active field of research. Moreover, open quantum systems strongly coupled to the environment are also gaining rapid popularity for the ability to steer system dynamics using the reservoir. Additionally, control over dynamical quantum phenomena and shortcut towards steady-state behaviour by use of electronic feedback techniques or tuning sequences predicted using machine learning are evolving areas of interdisciplinary research. Figure 5.1 connects some such trends in the extended domain of cavity optomechanical systems.

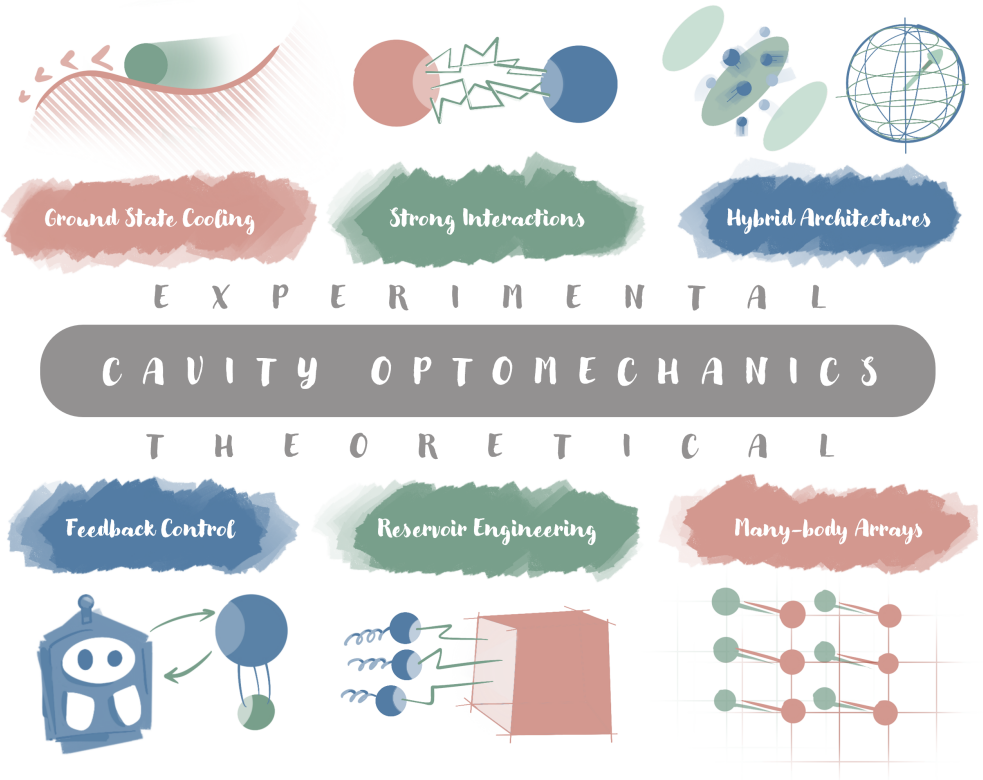


**Figure 5.1:** Recent trends in cavity optomechanics.

TH-3401_186121105

# Appendices



TH-3401_186121105

TH-3401_186121105

APPENDIX

# A

# Phonon Number in Coupled Systems

To have a better insight on the quantum dynamics of the mechanical oscillators in the coupled configurations described in Section 2.2, let us analyze the behaviour of their phonon numbers in the adiabatic limit of the cavity fields. We begin with the bidirectional configuration. In the rotating frame of the left mechanical frequency ($U = \exp[i\omega_{mL}\sum_{L,R}(-a_j^\dagger a_j + b_j^\dagger b_j)t]$), the linearized quantum dynamics can be obtained from Equations (2.3) as

$$\delta\dot{a}_L = -\frac{\kappa}{2}\delta a_L + i\left(\Delta_L - \omega_{mL}\right)\delta a_L + iG_L\delta b_L^\dagger + i\lambda\delta a_R + \sqrt{\kappa}a_{in_L} \quad \text{(A.1a)}$$

$$\delta\dot{a}_R = -\frac{\kappa}{2}\delta a_R + i\left(\Delta_R - \omega_{mL}\right)\delta a_R + iG_R\delta b_R^\dagger + i\lambda\delta a_L + \sqrt{\kappa}a_{in_R} \quad \text{(A.1b)}$$

$$\delta\dot{b}_L = -\frac{\gamma}{2}\delta b_L + iG_L\delta a_L^\dagger + \sqrt{\gamma}b_{in_L}, \quad \text{(A.1c)}$$

$$\delta\dot{b}_R = -\frac{\gamma}{2}\delta b_R - i\left(\omega_{mR} - \omega_{mL}\right)\delta b_R + iG_R\delta a_R^\dagger + \sqrt{\gamma}b_{in_R}, \quad \text{(A.1d)}$$

where the symbols represent the quantities defined in Section 2.2. It may be noted here that in deriving these equations, we have removed the highly oscillating terms in $\omega_{mL}$ under the rotating wave approximation. Now, as-



TH-3401_186121105

suming $\Delta_L = \omega_{mL} = \Delta_R$ for analytical simplicity, we eliminate the cavity modes to obtain the slower dynamics for the coupled mechanical modes as,

$$\delta\dot{b}_L = \left(\Gamma_L - \frac{\gamma}{2}\right)\delta b_L - i\chi^*\delta b_R + \epsilon_L\left(ia^\dagger_{in_L} + \frac{2\lambda}{\kappa}a^\dagger_{in_R}\right) + \sqrt{\gamma}b_{in_L}, \tag{A.2a}$$

$$\delta\dot{b}_R = \left(\Gamma_R - \frac{\gamma}{2}\right)\delta b_R - i\left(\omega_{mR} - \omega_{mL}\right)\delta b_R - i\chi\delta b_L + \epsilon_R + \sqrt{\gamma}b_{in_R}, \tag{A.2b}$$

where we have used $\Gamma_j = 2\kappa|G_j|^2/(4\lambda^2+\kappa^2)$, $\chi = 4\lambda G_L^* G_R/(4\lambda^2+\kappa^2)$ and $\epsilon_j = 2\sqrt{\kappa}\kappa G_j(ia^\dagger_{in_L} + 2\lambda a^\dagger_{in_R}/\kappa)/(4\lambda^2+\kappa^2)$. To obtain the steady-state value of the difference in the phonon numbers, we rewrite these equations in terms of the fluctuation quadratures which obey Equation (1.16). The steady-state solutions of these correlation elements then give us

$$n_{\text{diff}} \approx \frac{\gamma\kappa^2\left(n_{th}+1\right)\left(\Gamma_R - \Gamma_L\right)\left(1+\zeta^2\right)}{\Gamma_R\Gamma_L\left\{8\lambda^2 + 2\kappa^2\left(1+\zeta^2\right)\right\}}, \tag{A.3}$$

where we assume $\Gamma_j \gg \gamma$, with $\zeta = (\omega_{mR} - \omega_{mL})/(\Gamma_R + \Gamma_L)$. For a complete derivation of this expression, the reader may refer to the notebooks in [63]. The above expression hints that the phonon number difference vanishes in the steady-state only when $\Gamma_R = \Gamma_L$ (i.e., when $\langle\alpha_R\rangle = \langle\alpha_L\rangle$).

Following the exact same procedure for the unidirectional configuration, one can obtain the rate equations pertaining to the mechanical modes as

$$\delta\dot{b}_L = \left(\Gamma_L - \frac{\gamma}{2}\right)\delta b_L + i\epsilon_L a^\dagger_{in_L} + \sqrt{\gamma}b_{in_L}, \tag{A.4a}$$

$$\delta\dot{b}_R = \left(\Gamma_R - \frac{\gamma}{2}\right)\delta b_R - i\left(\omega_{mL} - \omega_{mR}\right)\delta b_R - \chi\delta b_L + \epsilon_R\left(-i\sqrt{\eta}\delta a^\dagger_{in_L} + i\sqrt{1-\eta}\delta a^\dagger_{in_R}\right) + \sqrt{\gamma}b_{in_R}, \tag{A.4b}$$

where $\Gamma_j = 2|G_j|^2/\kappa$, $\chi = 4\sqrt{\eta}G_L^* G_R/\kappa$ and $\epsilon_j = \sqrt{4/\kappa}G_j$. Here, we obtain the corresponding phonon number difference (assuming $\Gamma_j \gg \gamma$) as

$$n_{\text{diff}} \approx \frac{\gamma\left(n_{th}+1\right)\left(\Gamma_R - \Gamma_L\right)}{2\Gamma_R\Gamma_L} - \frac{2\eta\gamma\left(n_{th}+1\right)}{\left(\Gamma_R+\Gamma_L\right)\left(1+\zeta^2\right)}. \tag{A.5}$$

It can be easily inferred from this expression that even at zero detuning ($\zeta = 0$), a finite value of $\eta$ can give rise to a non-zero difference [63].

TH-3401_186121105

APPENDIX

# B

# Hamiltonian Formalism of the Ring-BEC System

The one-dimensional Hamiltonian describing the azimuthal motion of the BEC in the rotating frame of the laser frequency is given by [120]

$$\begin{aligned} H &= -\hbar\Delta_o a^\dagger a + \int_0^{2\pi} \Psi^\dagger(\phi)\left[-\frac{\hbar^2}{2I}\frac{d^2}{d\phi^2} + \hbar U_o \cos^2(l\phi) a^\dagger a\right]\Psi(\phi)d\phi \\ &\quad + \frac{g}{2}\int_0^{2\pi} \Psi^\dagger(\phi)\Psi^\dagger(\phi)\Psi(\phi)\Psi(\phi)d\phi - i\hbar A_l\left(a^\dagger - a\right), \end{aligned} \tag{B.1}$$

where $\Psi(\phi)$ denotes the bosonic atomic field operator obeying $[\Psi(\phi), \Psi^\dagger(\phi')] = \delta(\phi - \phi')$. Rest of the symbols have their usual meaning, as elaborated in Section 3.1. Here, the second expression inside the first integral denotes the atomic interactions with the cavity mode, whereas the second integral describes the atom-atom interactions.

Assuming an ansatz for the first ordered scattered sidebands as,

$$\Psi(\phi) = \frac{e^{iL_p\phi}}{\sqrt{2\pi}}c_p + \frac{e^{i(L_p+2l)\phi}}{\sqrt{2\pi}}c_+ + \frac{e^{i(L_p-2l)\phi}}{\sqrt{2\pi}}c_-, \tag{B.2}$$



TH-3401_186121105

with $[c_j, c_{j'}^\dagger] = \delta_{jj'}$ and $c_p^\dagger c_p + c_+^\dagger c_+ + c_-^\dagger c_- = N$, and introducing the operators $c = c_p^\dagger c_+/\sqrt{N}$ and $d = c_p^\dagger c_-/\sqrt{N}$, we obtain the Hamiltonain of Equation (3.1). It may be noted here that in deriving this Hamiltonian, we have also assumed that the mode with winding number $L_p$ is macroscopically occupied with relatively negligible occupancies in the sidemodes.

TH-3401_186121105

APPENDIX

C

# Effective Squeezing Parameter

The linearized Hamiltonian for the membrane-in-the-middle setup described in Section (4.2) can be written using Equations (4.3) as

$$H_l = -\hbar\Delta_1 a^\dagger a + \hbar\tilde{\omega}_m b^\dagger b + \hbar g\left(\alpha a^\dagger + \alpha^* a\right)\left(b^\dagger + b\right) + \hbar\Gamma_m\left(b^{\dagger 2} + b^2\right), \quad \text{(C.1)}$$

where we have used $\tilde{\omega}_m = \omega_m - 2\Gamma_m$, $g = 2g_1(\beta^* + \beta)$ and $\Gamma_m = g|\alpha|^2$. Using the squeezing transformation, $S(r) = \exp[r(b^2 - b^{\dagger 2})/2]$, we get

$$\begin{aligned}
H_s &= S(r)^\dagger H S(r) \\
&= -\hbar\Delta_1 a^\dagger a + \frac{\hbar\tilde{\omega}_m}{2}\left(b^\dagger b - bb^\dagger\right) \\
&\quad + \hbar\left\{gr\left(1 - 2r + 4r^2\cdots\right)\right\}\left(\alpha a^\dagger + \alpha^* a\right)\left(b^\dagger + b\right) \\
&\quad - \hbar\left(\frac{\tilde{\omega}_m}{2}\cosh[2r] + \Gamma_m \sinh[2r]\right)\left(b^\dagger b + bb^\dagger\right) \\
&\quad - \hbar\left(\frac{\tilde{\omega}_m}{2}\sinh[2r] + \Gamma_m \cosh[2r]\right)\left(b^\dagger b^\dagger + bb\right).
\end{aligned}$$



TH-3401_186121105

Setting the coefficient of $b^\dagger b^\dagger + bb$ equal to zero, we obtain the squeezing parameter as $r = \ln[1 + 4\Gamma_m/\omega_m]/4$. This gives us

$$\begin{aligned} H_s &= -\hbar\Delta_1 a^\dagger a + \hbar\omega'_m \left(b^\dagger b + \frac{1}{2}\right) - \frac{\hbar\tilde{\omega}_m}{2} \\ &\quad + \hbar\left(\frac{gr}{1+2r}\right)\left(\alpha a^\dagger + \alpha^* a\right)\left(b^\dagger + b\right), \end{aligned}$$

where $\omega'_m = \omega_m\sqrt{1 + 4\Gamma_m/\omega_m}$. Proceeding in a similar way as discussed in Section 4.2, the interaction term of the Hamiltonian in the rotating frame of the fluctuation operators under the rotating wave approximation becomes

$$\tilde{H}_s = a^\dagger\left(G'_1 b^\dagger + G'_0 b\right) + a\left(G'_0 b^\dagger + G'_1 b\right),$$

where $G'_1 = G_1\sqrt{\omega_m/\omega'_m}$ and $G'_0 = G_0\sqrt{\omega_m/\omega'_m}$. Thus, we obtain an effective squeezing parameter under the rotating wave approximation from this equation as $\tilde{r} = \tanh^{-1}[G'_1/G'_0] = \tanh^{-1}[G_1/G_0]$ [159, 163].

TH-3401_186121105

APPENDIX

# D

# Hamiltonian Formalism of the Hybrid System

We begin with the complete Hamiltonian of the hybrid opto-electro-mechanical system described in Section 4.3 as Equation (4.11):

$$\begin{aligned} H &= \hbar\omega_a a^\dagger a + \frac{1}{2}m_b\omega_b^2 q_b^2 + \frac{p_b^2}{2m_b} + \frac{q_c^2}{2C_c} + \frac{p_c^2}{2L_c} \\ &\quad + i\hbar\left(A_l a^\dagger e^{-i\omega_l t} - A_l^* a e^{i\omega_l t}\right) - q_c V_c. \end{aligned} \tag{D.1}$$

Next, we simplify and approximate the capacitance $C_c$ by using the participation ratio $r = C_{c0}/(C_{cp} + C_{c0})$ as

$$\begin{aligned} C_c &= C_{cp} + \frac{C_{c0}}{1 - \frac{q_b}{d}}, \\ &= \frac{r\left(1 - \frac{q_b}{d}\right)\left(1 + \frac{rq_b}{d} - \frac{q_b}{d}\right)^{-1}}{C_{c0}}, \\ &\approx \frac{r}{C_{c0}} - \frac{r^2 q_b}{C_{c0}d} + \frac{r^2 q_b^2}{C_{c0}d^2} - \frac{rq_b^2}{C_{c0}d^2} + \dots. \end{aligned} \tag{D.2}$$



TH-3401_186121105

Now, ignoring the higher order terms in $q_b/d$, and utilizing the relations $\omega_c = 1/\sqrt{L_c(C_{cp} + C_{c0})}$, $A_v = q_{c_{ZP}} V_c/\hbar$ $q_c = q_{c_{ZP}}(c^\dagger + c)$ and $p_c = ip_{c_{ZP}}(c^\dagger - c)$, such that $q_{c_{ZP}} = \sqrt{\hbar/(2L\omega_c)}$ and $p_{c_{ZP}} = \sqrt{\hbar L\omega_c/2}$ [179], we obtain the terms involving the driven LC circuit mode as $H_{em} = \hbar\omega_c c^\dagger c - \hbar g_1(b^\dagger + b)(c^\dagger + c)^2 - \hbar A_v(c^\dagger + c)$, where $g_1$ is given by Equation (4.13). Also, following the formalism of Section 1.1, we can write the first three terms and the laser Hamiltonian in the rotating frame of the laser frequency as $H_{om} = -\hbar\Delta_0 a^\dagger a + \hbar\omega_b b^\dagger b - \hbar g_0 a^\dagger a(b^\dagger + b) + i\hbar(A_l a^\dagger - A_l^* a)$. Combining the expressions of $H_{om}$ and $H_{em}$, we obtain the Hamiltonian in Equation (4.11).

TH-3401_186121105

TH-3401_186121105

TH-3401_186121105

# Bibliography


[1] Kepler, J. *De Cometis Libelli Tres*. Typis Andreæ Apergeri, (1619).

[2] Lindberg, D. C. *Osiris* **2**, 4–42 (1986).

[3] Thomson, W. *Proc. R. Soc. Edinb. B* **3**, 108–114 (1857).

[4] Maxwell, J. C. *A Treatise on Electricity and Magnetism*. Cambridge University Press, (1873).

[5] Sarma, A. K. and Kalita, S. *Indian J. Pure Appl. Phys.* **61**(7), 622–634 (2023).

[6] Ashkin, A. *Phys. Rev. Lett.* **24**, 156–159 (1970).

[7] Braginskii, V. B. and Manukin, A. B. *Sov. Phys. JETP* **25**, 653–655 (1967).

[8] Caves, C. M. *Phys. Rev. Lett.* **45**, 75–79 (1980).

[9] Aspelmeyer, M., Kippenberg, T. J., and Marquardt, F. *Rev. Mod. Phys.* **86**, 1391–1452 (2014).

[10] Aspelmeyer, M., Kippenberg, T. J., and Marquardt, F. *Cavity Optomechanics: Nano- and Micromechanical Resonators Interacting with Light*. Springer Berlin Heidelberg, (2014).

[11] Aspelmeyer, M., Meystre, P., and Schwab, K. *Physics Today* **65**, 29 (2012).

[12] Bowen, W. P. and Milburn, G. J. *Quantum Optomechanics*. Taylor & Francis, (2015).


TH-3401_186121105

[13] Dorsel, A., McCullen, J. D., Meystre, P., Vignes, E., and Walther, H. *Phys. Rev. Lett.* **51**, 1550–1553 (1983).

[14] Bakemeier, L., Alvermann, A., and Fehske, H. *Phys. Rev. Lett.* **114**, 013601 (2015).

[15] Mari, A., Farace, A., Didier, N., Giovannetti, V., and Fazio, R. *Phys. Rev. Lett.* **111**, 103605 (2013).

[16] Wilson-Rae, I., Nooshi, N., Zwerger, W., and Kippenberg, T. J. *Phys. Rev. Lett.* **99**, 093901 (2007).

[17] Weis, S., Rivière, R., Deléglise, S., Gavartin, E., Arcizet, O., Schliesser, A., and Kippenberg, T. J. *Science* **330**(6010), 1520–1523 (2010).

[18] Huang, S. and Agarwal, G. S. *Phys. Rev. A* **81**, 033830 (2010).

[19] Vitali, D., Gigan, S., Ferreira, A., Boehm, H., Tombesi, P., Guerreiro, A., Vedral, V., Zeilinger, A., and Aspelmeyer, M. *Phys. Rev. Lett.* **98**(3), 030405 (2007).

[20] Bai, C.-H., Wang, D.-Y., Zhang, S., Liu, S., and Wang, H.-F. *Phys. Rev. A* **101**, 053836 (2020).

[21] Gan, J.-H., Xiong, H., Si, L.-G., Lü, X.-Y., and Wu, Y. *Opt. Lett.* **41**, 2676–2679 (2016).

[22] Oliveira, H. M. and Melo, L. V. *Sci. Rep.* **5**(1), 11548 (2015).

[23] Strogatz, S. H. *Sync: The Emerging Science of Spontaneous Order.* Penguin Books Limited, (2004).

[24] Sivrikaya, F. and Yener, B. *IEEE Network* **18**(4), 45–50 (2004).

[25] Li, Q. and Rus, D. *IEEE Trans. Comput.* **55**(2), 214–226 (2006).

[26] Koppenhöfer, M. and Roulet, A. *Phys. Rev. A* **99**, 043804 (2019).

[27] Jaseem, N., Hajdušek, M., Solanki, P., Kwek, L.-C., Fazio, R., and Vinjanampathy, S. *Phys. Rev. Research* **2**, 043287 (2020).

TH-3401_186121105

[28] Galve, F., Luca Giorgi, G., and Zambrini, R. In *Lectures on General Quantum Correlations and their Applications,* Fanchini, F. F., Soares Pinto, D. d. O., and Adesso, G., editors, 393–420. Springer International Publishing, Cham. (2017).

[29] Li, T., Bao, T.-Y., Zhang, Y.-L., Zou, C.-L., Zou, X.-B., and Guo, G.-C. *Opt. Express* **24**(11), 12336–12348 (2016).

[30] Marangos, J. P. *J. Mod. Opt.* **45**(3), 471–503 (1998).

[31] Xiong, H. and Wu, Y. *Appl. Phys. Rev.* **5**, 031305 (2018).

[32] Duan, Z., Fan, B., Stace, T. M., Milburn, G. J., and Holmes, C. A. *Phys. Rev. A* **93**, 023802 (2016).

[33] Safavi-Naeini, A. H., Alegre, T. P. M., Eichenfield, M., Wigner, M., Lin, Q., Hill, J. T., Chang, D. E., and Painter, O. *Nature* **472**, 69–73 (2011).

[34] Einstein, A., Podolsky, B., and Rosen, N. *Phys. Rev.* **47**, 777–780 (1935).

[35] Bell, J. S. *Phys. Phys. Fiz.* **1**, 195–200 (1964).

[36] Bell, J. S. *Rev. Mod. Phys.* **38**, 447–452 (1966).

[37] Hensen, B. et al. *Nature* **526**, 682–686 (2015).

[38] Bouwmeester, D., Ekert, A., and Zeilinger, A. *The Physics of Quantum Information*. Springer Berlin Heidelberg, (2000).

[39] Wilde, M. M. *Quantum Information Theory*. Cambridge University Press, (2013).

[40] Mari, A. and Eisert, J. *Phys. Rev. Lett.* **103**, 213603 (2009).

[41] Asjad, M., Tombesi, P., and Vitali, D. *Phys. Rev. A* **94**, 052312 (2016).

[42] Lau, H.-K. and Clerk, A. A. *Science* **372**, 570–571 (2021).

[43] Tse, M. et al. *Phys. Rev. Lett.* **123**, 231107 (2019).

[44] Barzanjeh, S., Vitali, D., Tombesi, P., and Milburn, G. J. *Phys. Rev. A* **84**, 042342 (2011).

TH-3401_186121105

[45] Li, J. and Gröblacher, S. *New J. Phys.* **22**, 063041 (2020).

[46] Barzanjeh, S., Guha, S., Weedbrook, C., Vitali, D., Shapiro, J. H., and Pirandola, S. *Phys. Rev. Lett.* **114**, 080503 (2015).

[47] Gardiner, C. W. and Collett, M. J. *Phys. Rev. A* **31**, 3761–3774 (1985).

[48] Walls, D. F. and Milburn, G. J. *Quantum Optics*. Springer Berlin Heidelberg, (2012).

[49] Benguria, R. and Kac, M. *Phys. Rev. Lett.* **46**, 1–4 (1981).

[50] DeJesus, E. X. and Kaufman, C. *Phys. Rev. A* **35**, 5288–5290 (1987).

[51] Zhang, M., Wiederhecker, G. S., Manipatruni, S., Barnard, A., McEuen, P., and Lipson, M. *Phys. Rev. Lett.* **109**, 233906 (2012).

[52] Liao, C.-G., Chen, R.-X., Xie, H., He, M.-Y., and Lin, X.-M. *Phys. Rev. A* **99**, 033818 (2019).

[53] Sarma, A. K., Chakraborty, S., and Kalita, S. *AVS Quantum Sci.* **3**, 015901 (2021).

[54] Williamson, J. *American Journal of Mathematics* **58**(1), 141–163 (1936).

[55] Horodecki, P. *Physics Letters A* **232**(5), 333–339 (1997).

[56] Peres, A. *Phys. Rev. Lett.* **77**, 1413–1415 (1996).

[57] Simon, R. *Phys. Rev. Lett.* **84**, 2726–2729 (2000).

[58] Vidal, G. and Werner, R. F. *Phys. Rev. A* **65**, 032314 (2002).

[59] Adesso, G., Serafini, A., and Illuminati, F. *Phys. Rev. A* **70**, 022318 (2004).

[60] Kalita, S. and Sarma, A. K. In *Proceedings of Eighth International Congress on Information and Communication Technology*, volume 694 of *Lecture Notes in Networks and Systems*, 581–590. Springer Nature Singapore, (2023).

TH-3401_186121105

[61] A wonderful demonstration of synchronization in classical systems can be found in *Steven Strogatz's TED talk*. A technical version of the same can be found in *his recent talk on his book "Sync"*. For more resources, the reader may also visit *his collection of articles on synchronization*.

[62] Kalita, S., Chakraborty, S., and Sarma, A. K. *J. Phys. Commun.* **5**(11), 115006 (2021).

[63] All the resources for the work are available in the *sync-bi-uni* GitHub repository. The notebooks corresponding to the derivation of phonon number differences and the plots in the manuscript are available in the *notebooks* folder. Note that the convention for the decay rates and their corresponding values have been updated in this thesis in order to maintain consistency with the convention used in all the chapters.

[64] Walter, S., Nunnenkamp, A., and Bruder, C. *Ann. Phys.* **527**, 131–138 (2015).

[65] Lörch, N., Amitai, E., Nunnenkamp, A., and Bruder, C. *Phys. Rev. Lett.* **117**, 073601 (2016).

[66] Xu, M., Tieri, D. A., Fine, E. C., Thompson, J. K., and Holland, M. J. *Phys. Rev. Lett.* **113**, 154101 (2014).

[67] Hush, M. R., Li, W., Genway, S., Lesanovsky, I., and Armour, A. D. *Phys. Rev. A* **91**, 061401 (2015).

[68] Laskar, A. W., Adhikary, P., Mondal, S., Katiyar, P., Vinjanampathy, S., and Ghosh, S. *Phys. Rev. Lett.* **125**, 013601 (2020).

[69] Heinrich, G., Ludwig, M., Qian, J., Kubala, B., and Marquardt, F. *Phys. Rev. Lett.* **107**, 043603 (2011).

[70] Holmes, C. A., Meaney, C. P., and Milburn, G. J. *Phys. Rev. E* **85**, 066203 (2012).

[71] Bagheri, M., Poot, M., Fan, L., Marquardt, F., and Tang, H. X. *Phys. Rev. Lett.* **111**, 213902 (2013).

[72] Zhang, M., Shah, S., Cardenas, J., and Lipson, M. *Phys. Rev. Lett.* **115**, 163902 (2015).

TH-3401_186121105

[73] Li, W., Li, C., and Song, H. *Phys. Rev. E* **95**, 022204 (2017).

[74] Li, W., Zhang, F., Li, C., and Song, H. *Commun. Nonlinear Sci. Numer. Simulat.* **42**, 121–131 (2017).

[75] Amitai, E., Lörch, N., Nunnenkamp, A., Walter, S., and Bruder, C. *Phys. Rev. A* **95**, 053858 (2017).

[76] Sonar, S., Hajdušek, M., Mukherjee, M., Fazio, R., Vedral, V., Vinjanampathy, S., and Kwek, L.-C. *Phys. Rev. Lett.* **120**, 163601 (2018).

[77] Ludwig, M. and Marquardt, F. *Phys. Rev. Lett.* **111**, 073603 (2013).

[78] Weiss, T., Kronwald, A., and Marquardt, F. *New J. Phys.* **18**, 013043 (2016).

[79] Yang, N., Miranowicz, A., Liu, Y.-C., Xia, K., and Nori, F. *Sci. Rep.* **9**, 15874 (2019).

[80] Ying, L., Lai, Y.-C., and Grebogi, C. *Phys. Rev. A* **90**, 053810 (2014).

[81] Gil-Santos, E., Labousse, M., Baker, C., Goetschy, A., Hease, W., Gomez, C., Lemaître, A., Leo, G., Ciuti, C., and Favero, I. *Phys. Rev. Lett.* **118**, 063605 (2017).

[82] Giorgi, G. L., Galve, F., Manzano, G., Colet, P., and Zambrini, R. *Phys. Rev. A* **85**, 052101 (2012).

[83] Manzano, G., Galve, F., Giorgi, G., Hernández-García, E., and Zambrini, R. *Sci. Rep.* **3**, 1439 (2013).

[84] Lee, T. E., Chan, C.-K., and Wang, S. *Phys. Rev. E* **89**, 022913 (2014).

[85] Bemani, F., Motazedifard, A., Roknizadeh, R., Naderi, M. H., and Vitali, D. *Phys. Rev. A* **96**, 023805 (2017).

[86] Roulet, A. and Bruder, C. *Phys. Rev. Lett.* **121**, 063601 (2018).

[87] Witthaut, D., Wimberger, S., Burioni, R., and Timme, M. *Nat. Commun.* **8**, 14829 (2017).

[88] Ameri, V., Eghbali-Arani, M., Mari, A., Farace, A., Kheirandish, F., Giovannetti, V., and Fazio, R. *Phys. Rev. A* **91**, 012301 (2015).

TH-3401_186121105

[89] Gardiner, C. W. *Phys. Rev. Lett.* **70**, 2269–2272 (1993).

[90] Cirac, J. I., Zoller, P., Kimble, H. J., and Mabuchi, H. *Phys. Rev. Lett.* **78**, 3221–3224 (1997).

[91] Tan, H., Buchmann, L. F., Seok, H., and Li, G. *Phys. Rev. A* **87**, 022318 (2013).

[92] Kalita, S., Kumar, P., Kanamoto, R., Bhattacharya, M., and Sarma, A. K. *Phys. Rev. A* **107**, 013525 (2023).

[93] All the resources for the work are available in the *omit-bec* GitHub repository. Note that the symbols for most of the system parameters have been updated in this thesis in order to maintain consistency with the convention used in all the chapters.

[94] Shi, H. and Bhattacharya, M. *J. Phys. B: At. Mol. Opt. Phys.* **49**, 153001 (2016).

[95] He, H., Friese, M. E. J., Heckenberg, N. R., and Rubinsztein-Dunlop, H. *Phys. Rev. Lett.* **75**, 826–829 (1995).

[96] Simpson, N. B., Dholakia, K., Allen, L., and Padgett, M. J. *Opt. Lett.* **22**(1), 52–54 (1997).

[97] Piccirillo, B., Toscano, C., Vetrano, F., and Santamato, E. *Phys. Rev. Lett.* **86**, 2285–2288 (2001).

[98] Andersen, M. F., Ryu, C., Cladé, P., Natarajan, V., Vaziri, A., Helmerson, K., and Phillips, W. D. *Phys. Rev. Lett.* **97**, 170406 (2006).

[99] Ryu, C., Andersen, M. F., Cladé, P., Natarajan, V., Helmerson, K., and Phillips, W. D. *Phys. Rev. Lett.* **99**, 260401 (2007).

[100] Wright, K. C., Leslie, L. S., and Bigelow, N. P. *Phys. Rev. A* **77**, 041601 (2008).

[101] Beattie, S., Moulder, S., Fletcher, R. J., and Hadzibabic, Z. *Phys. Rev. Lett.* **110**, 025301 (2013).

[102] Wright, K. C., Blakestad, R. B., Lobb, C. J., Phillips, W. D., and Campbell, G. K. *Phys. Rev. Lett.* **110**, 025302 (2013).

TH-3401_186121105

[103] Ryu, C., Blackburn, P. W., Blinova, A. A., and Boshier, M. G. *Phys. Rev. Lett.* **111**, 205301 (2013).

[104] Eckel, S., Lee, J. G., Jendrzejewski, F., Murray, N., Clark, C. W., Lobb, C. J., Phillips, W. D., Edwards, M., and Campbell, G. K. *Nature* **506**, 200–203 (2014).

[105] Marti, G. E., Olf, R., and Stamper-Kurn, D. M. *Phys. Rev. A* **91**, 013602 (2015).

[106] Eckel, S., Kumar, A., Jacobson, T., Spielman, I. B., and Campbell, G. K. *Phys. Rev. X* **8**, 021021 (2018).

[107] Öhberg, P. and Wright, E. M. *Phys. Rev. Lett.* **123**, 250402 (2019).

[108] Fetter, A. L. *Rev. Mod. Phys.* **81**, 647–691 (2009).

[109] Freilich, D. V., Bianchi, D. M., Kaufman, A. M., Langin, T. K., and Hall, D. S. *Science* **329**(5996), 1182–1185 (2010).

[110] Cooper, N. *Advances in Physics* **57**(6), 539–616 (2008).

[111] Shin, Y., Saba, M., Vengalattore, M., Pasquini, T. A., Sanner, C., Leanhardt, A. E., Prentiss, M., Pritchard, D. E., and Ketterle, W. *Phys. Rev. Lett.* **93**, 160406 (2004).

[112] Tilley, D. R. and Tilley, J. *Superfluidity and Superconductivity*. Graduate Student Series in Physics. Taylor & Francis, (1990).

[113] Mehdi, Z., Bradley, A. S., Hope, J. J., and Szigeti, S. S. *SciPost Phys.* **11**, 080 (2021).

[114] Pandey, S., Mas, H., Vasilakis, G., and von Klitzing, W. *Phys. Rev. Lett.* **126**, 170402 (2021).

[115] Amico, L. et al. *AVS Quantum Sci.* **3**(3), 039201 (2021).

[116] Polo, J., Ahufinger, V., Hekking, F. W. J., and Minguzzi, A. *Phys. Rev. Lett.* **121**, 090404 (2018).

[117] Park, J. W., Ko, B., and Shin, Y. *Phys. Rev. Lett.* **121**, 225301 (2018).

TH-3401_186121105

[118] Cai, Y., Allman, D. G., Sabharwal, P., and Wright, K. C. *Phys. Rev. Lett.* **128**, 150401 (2022).

[119] Del Pace, G., Xhani, K., Muzi Falconi, A., Fedrizzi, M., Grani, N., Hernandez Rajkov, D., Inguscio, M., Scazza, F., Kwon, W. J., and Roati, G. *Phys. Rev. X* **12**, 041037 (2022).

[120] Kumar, P., Biswas, T., Feliz, K., Kanamoto, R., Chang, M.-S., Jha, A. K., and Bhattacharya, M. *Phys. Rev. Lett.* **127**, 113601 (2021).

[121] Morizot, O., Colombe, Y., Lorent, V., Perrin, H., and Garraway, B. M. *Phys. Rev. A* **74**, 023617 (2006).

[122] Naidoo, D., A it-Ameur, K., Brunel, M., and Forbes, A. *Appl. Phys. B* **106**, 683–690 (2012).

[123] Cheng, Z.-D. et al. *Opt. Lett.* **42**(10), 2042–2045 (2017).

[124] Huang, S., Miao, Z., He, C., Pang, F., Li, Y., and Wang, T. *Opt. Lasers Eng.* **78**, 132–139 (2016).

[125] Moulder, S., Beattie, S., Smith, R. P., Tammuz, N., and Hadzibabic, Z. *Phys. Rev. A* **86**, 013629 (2012).

[126] Brennecke, F., Ritter, S., Donner, T., and Esslinger, T. *Science* **322**(5899), 235–238 (2008).

[127] Agarwal, G. S. and Huang, S. *Phys. Rev. A* **81**, 041803 (2010).

[128] Herve, M. d. G. d., Guo, Y., Rossi, C. D., Kumar, A., Badr, T., Dubessy, R., Longchambon, L., and Perrin, H. *J. Phys. B: At. Mol. Opt. Phys.* **54**, 125302 (2021).

[129] Tiesinga, E., Williams, C. J., Julienne, P. S., Jones, K. M., Lett, P. D., and Phillips, W. D. *J. Res. Natl. Inst. Stand. Technol.* **101**, 505–520 (1996).

[130] Ludlow, A. D., Huang, X., Notcutt, M., Zanon-Willette, T., Foreman, S. M., Boyd, M. M., Blatt, S., and Ye, J. *Opt. Lett.* **32**(6), 641–643 (2007).

[131] Safavi-Naeini, A. H., Alegre, T. P. M., Chan, J., Eichenfield, M., Winger, M., Lin, Q., Hill, J. T., Chang, D. E., and Painter, O. *Nature* **472**, 69–73 (2011).

[132] Peng, J.-X., Chen, Z., Yuan, Q.-Z., and Feng, X.-L. *Phys. Lett. A* **384**, 126153 (2020).

[133] Alzar, C. L. G., Martinez, M. A. G., and Nussenzveig, P. *Am. J. Phys.* **70**, 37 (2002).

[134] Lemonde, M.-A., Didier, N., and Clerk, A. A. *Phys. Rev. Lett.* **111**, 053602 (2013).

[135] Børkje, K., Nunnenkamp, A., Teufel, J. D., and Girvin, S. M. *Phys. Rev. Lett.* **111**, 053603 (2013).

[136] Kronwald, A. and Marquardt, F. *Phys. Rev. Lett.* **111**, 133601 (2013).

[137] Ma, P.-C., Zhang, J.-Q., Xiao, Y., Feng, M., and Zhang, Z.-M. *Phys. Rev. A* **90**, 043825 (2014).

[138] Huang, S. *J. Phys. B: At. Mol. Opt. Phys.* **47**, 055504 (2014).

[139] Qu, K. and Agarwal, G. S. *Phys. Rev. A* **87**, 063813 (2013).

[140] Chen, H.-J. *Phys. Rev. A* **104**, 013708 (2021).

[141] Mikaeili, H., Dalafi, A., Ghanaatshoar, M., and Askari, B. *Sci. Rep.* **12**, 4428 (2022).

[142] Tian, L. *Phys. Rev. Lett.* **108**, 153604 (2012).

[143] Wang, Y.-D. and Clerk, A. A. *Phys. Rev. Lett.* **108**, 153603 (2012).

[144] Zhang, Z., Pei, J., Wang, Y.-P., and Wang, X. *Front. Phys.* **16**(5), 32503 (2021).

[145] Stern, L., Grajower, M., and Levy, U. *Nat. Commun.* **5**, 4865 (2014).

[146] Lü, H., Jiang, Y., Wang, Y.-Z., and Jing, H. *Photon. Res.* **5**(4), 367–371 (2017).

[147] Hill, J. T., Safavi-Naeini, A. H., Chan, J., and Painter, O. *Nat. Commun.* **3**, 1196 (2012).

TH-3401_186121105

[148] Banerjee, P., Kalita, S., and Sarma, A. K. *J. Opt. Soc. Am. B* **40**(6), 1398–1406 (2023).

[149] All the resources for the work are available in the *squeeze-mm* GitHub repository. Note that the convention for the laser detuning and its corresponding value have been updated in this thesis in order to maintain consistency with the convention used in all the chapters.

[150] Kalita, S., Shah, S., and Sarma, A. K. *Phys. Rev. A* **106**, 043501 (2022).

[151] All the resources for the work are available in the *entan-oem-mod* GitHub repository. Note that the convention for the laser detuning and the decay rates and their corresponding values have been updated in this thesis in order to maintain consistency with the convention used in all the chapters.

[152] Wollman, E. E., Lei, C. U., Weinstein, A. J., Suh, J., Kronwald, A., Marquardt, F., Clerk, A. A., and Schwab, K. C. *Science* **349**(6251), 952–955 (2015).

[153] Hope, D. M., Bachor, H.-A., Manson, P. J., McClelland, D. E., and Fisk, P. T. H. *Phys. Rev. A* **46**, R1181–R1184 (1992).

[154] Nunnenkamp, A., Børkje, K., Harris, J. G. E., and Girvin, S. M. *Phys. Rev. A* **82**, 021806 (2010).

[155] Lü, X.-Y., Liao, J.-Q., Tian, L., and Nori, F. *Phys. Rev. A* **91**, 013834 (2015).

[156] Zhang, R., Fang, Y., Wang, Y.-Y., Chesi, S., and Wang, Y.-D. *Phys. Rev. A* **99**, 043805 (2019).

[157] Huang, S. and Agarwal, G. S. *Phys. Rev. A* **82**, 033811 (2010).

[158] Jähne, K., Genes, C., Hammerer, K., Wallquist, M., Polzik, E. S., and Zoller, P. *Phys. Rev. A* **79**, 063819 (2009).

[159] Kronwald, A., Marquardt, F., and Clerk, A. A. *Phys. Rev. A* **88**, 063833 (2013).

TH-3401_186121105

[160] Qin, W., Miranowicz, A., and Nori, F. *Phys. Rev. Lett.* **129**, 123602 (2022).

[161] Gu, W.-j., Li, G.-x., and Yang, Y.-p. *Phys. Rev. A* **88**, 013835 (2013).

[162] Rabl, P., Shnirman, A., and Zoller, P. *Phys. Rev. B* **70**, 205304 (2004).

[163] Zhang, J.-S. and Chen, A.-X. *Opt. Express* **28**(9), 12827–12836 (2020).

[164] Lei, C. U., Weinstein, A. J., Suh, J., Wollman, E. E., Kronwald, A., Marquardt, F., Clerk, A. A., and Schwab, K. C. *Phys. Rev. Lett.* **117**, 100801 (2016).

[165] Abbott, B. P. et al. *Rep. Prog. Phys.* **72**(7), 076901 (2009).

[166] Accadia, T. et al. *Astropart. Phys.* **34**(7), 521–527 (2011).

[167] Braunstein, S. L. and van Loock, P. *Rev. Mod. Phys.* **77**, 513–577 (2005).

[168] Akram, U., Munro, W., Nemoto, K., and Milburn, G. J. *Phys. Rev. A* **86**, 042306 (2012).

[169] Sete, E. A., Eleuch, H., and Raymond Ooi, C. H. *J. Opt. Soc. Am. B* **31**, 2821–2828 (2014).

[170] Li, J., Haghighi, I. M., Malossi, N., Zippilli, S., and Vitali, D. *New J. Phys.* **17**, 103037 (2015).

[171] Lai, D.-G., Qin, W., Hou, B.-P., Miranowicz, A., and Nori, F. *Phys. Rev. A* **104**, 043521 (2021).

[172] Riedinger, R., Wallucks, A., Marinković, I., L oschnauer, C., Aspelmeyer, M., Hong, S., and Gr oblacher, S. *Nature* **556**, 473–477 (2018).

[173] Ockeloen-Korppi, C. F., Damsk agg, E., Pirkkalainen, J.-M., Asjad, M., Clerk, A. A., Massel, F., Woolley, M. J., and Sillanp a a, M. A. *Nature* **556**, 478–482 (2018).

[174] Chen, J., Rossi, M., Mason, D., and Schliesser, A. *Nat. Commun.* **11**, 943 (2020).

[175] Barzanjeh, S., Xuereb, A., Gr oblacher, S., Paternostro, M., Regal, C. A., and Weig, E. M. *Nat. Phys.* **18**, 15–24 (2021).

[176] Regal, C. A. and Lehnert, K. W. *J. Phys.: Conf. Ser.* **264**, 012025 (2011).

[177] Midolo, L., Schliesser, A., and Fiore, A. *Nat. Nanotechnol.* **13**, 11–18 (2018).

[178] Zeuthen, E., Schliesser, A., Taylor, J. M., and Sørensen, A. S. *Phys. Rev. Applied* **10**, 044036 (2018).

[179] Vool, U. and Devoret, M. *Int. J. Circuit Theory Appl.* **45**(7), 897–934 (2017).

[180] Paternostro, M., Vitali, D., Gigan, S., Kim, M. S., Brukner, C., Eisert, J., and Aspelmeyer, M. *Phys. Rev. Lett.* **99**, 250401 (2007).

[181] Vitali, D., Tombesi, P., Woolley, M. J., Doherty, A. C., and Milburn, G. J. *Phys. Rev. A* **76**, 042336 (2007).

[182] Jiang, C., Tserkis, S., Collins, K., Onoe, S., Li, Y., and Tian, L. *Phys. Rev. A* **101**, 042320 (2020).

[183] Fu, W., Xu, M., Liu, X., Zou, C.-L., Zhong, C., Han, X., Shen, M., Xu, Y., Cheng, R., Wang, S., Jiang, L., and Tang, H. X. *Phys. Rev. A* **103**, 053504 (2021).

[184] Zhang, J.-S., Li, M.-C., and Chen, A.-X. *Phys. Rev. A* **99**, 013843 (2019).

[185] Karuza, M., Biancofiore, C., Bawaj, M., Molinelli, C., Galassi, M., Natali, R., Tombesi, P., Di Giuseppe, G., and Vitali, D. *Phys. Rev. A* **88**, 013804 (2013).

[186] Chen, R.-X., Shen, L.-T., Yang, Z.-B., Wu, H.-Z., and Zheng, S.-B. *Phys. Rev. A* **89**, 023843 (2014).

[187] Bai, C.-H., Wang, D.-Y., Zhang, S., Liu, S., and Wang, H.-F. *Annalen der Physik* **531**(7), 1800271 (2019).

[188] Zhang, W.-J., Zhang, Y., Guo, Q., Liu, A.-P., Li, G., and Zhang, T. *Phys. Rev. A* **104**, 053506 (2021).

TH-3401_186121105

[189] Bothner, D., Yanai, S., Iniguez-Rabago, A., Yuan, M., Blanter, Y. M., and Steele, G. A. *Nat. Commun.* **11**, 1589 (2020).

[190] Marquardt, F., Chen, J. P., Clerk, A. A., and Girvin, S. M. *Phys. Rev. Lett.* **99**, 093902 (2007).

[191] Pirkkalainen, J.-M., Damskägg, E., Brandt, M., Massel, F., and Sillanpää, M. A. *Phys. Rev. Lett.* **115**, 243601 (2015).

[192] Woolley, M. J., Doherty, A. C., Milburn, G. J., and Schwab, K. C. *Phys. Rev. A* **78**, 062303 (2008).

[193] Meaney, C. P., McKenzie, R. H., and Milburn, G. J. *Phys. Rev. E* **83**, 056202 (2011).

[194] Sonar, S., Fedoseev, V., Weaver, M. J., Luna, F., Vlieg, E., van der Meer, H., Bouwmeester, D., and Löffler, W. *Phys. Rev. A* **98**, 013804 (2018).

[195] Asjad, M., Agarwal, G. S., Kim, M. S., Tombesi, P., Giuseppe, G. D., and Vitali, D. *Phys. Rev. A* **89**, 023849 (2014).

[196] Yan, K., Zhang, Y., Cui, Y., and Jiang, C. *Opt. Commun.* **475**, 126249 (2020).

[197] Malossi, N., Piergentili, P., Li, J., Serra, E., Natali, R., Di Giuseppe, G., and Vitali, D. *Phys. Rev. A* **103**, 033516 (2021).

[198] Farace, A. and Giovannetti, V. *Phys. Rev. A* **86**, 013820 (2012).

[199] Wang, M., Lü, X.-Y., Wang, Y.-D., You, J. Q., and Wu, Y. *Phys. Rev. A* **94**, 053807 (2016).

[200] Nongthombam, R., Kalita, S., and Sarma, A. K. *Phys. Rev. A* **107**, 013528 (2023).

[201] All the resources for the work are available in the *sync-qubit* GitHub repository.

[202] Gupta, P. K., Kalita, S., and Sarma, A. K. *J. Opt. Soc. Am. B* **41**(2), 447–455 (2024).

[203] All the resources for the work are available in the *blockade-mag* GitHub repository.

TH-3401_186121105

# Vita

Sampreet Kalita is a Prime Minister's Research Fellow at the Department of Physics, Indian Institute of Technology Guwahati, India. He graduated as a B.Tech. (Engineering Physics) in 2017 from Indian Institute of Technology Guwahati, India and worked in software development and embedded systems both in the industry and academia before joining Ph.D. in Quantum Optics. He has completed multiple projects in quantum phenomena, classical cryptography, parallel computing, machine learning, and native/web application development. He is also passionate about programming, design and music. He is currently exploring hybrid open quantum systems strongly coupled to the environment and deep reinforcement learning-based feedback control.

EXPERIENCES

| Tenure | Institute/Company | Position |
|---|---|---|
| *2021 - 23* | *North Gauhati College* | *Visiting Instructor* |
| *2019 - 23* | *Indian Institute of Technology Guwahati* | *Teaching Assistant* |
| *2017 - 18* | *Tezpur University* | *Project Staff (JRF)* |
| *2016* | *Rupeek Fintech* | *Full-stack Intern* |

AWARDS

| | |
|---|---|
| Prime Minister's Research Fellow | MHRD, Govt. of India |
| Kishore Vaigyanik Protsahan Yojana | DST, Govt. of India |
| National Talent Search Scholarship | NCERT, Govt. of India |
| Cultural Talent Search Scholarship | CCRT, Govt. of India |

TH-3401_186121105

TH-3401_186121105